First Principles Study of Structure and Lithium Storage in Inorganic Nanotubes

by
Kevin Tibbetts
Submitted to the Department of Materials Science and Engineering in partial fulfillment of the requirements for the degree of

Doctor of Philosophy

in Materials Science and Engineering

at the

MASSACHUSETTS INSTITUTE OF TECHNOLOGY

September 2009

Author ....
Department of Materials Science and Engineering
June 17, 2009

Certified by...
Gerbrand Ceder
R.P. Simmons Professor of Materials Science and Engineering
Thesis Supervisor

Accepted by ....
Christine Ortiz
Chair, Departmental Committee on Graduate Students

First Principles Study of Structure and Lithium Storage in Inorganic Nanotubes

by

Kevin Tibbetts

Submitted to the Department of Materials Science and Engineering in partial fulfillment of the
requirements for the degree of
Doctor of Philosophy
in Materials Science and Engineering
June 17, 2009

Abstract

The exact structure of layered inorganic nanotubes is difficult to determine, but this information is vital to using atomistic calculations to predict nanotube properties. A multi-walled nanotube with a circular cross section will have either a mostly incoherent interface or a large amount of tensile strain to accommodate a coherent interface, but a polygonal cross section could result in a coherent interface with considerably less strain. An energy component model is parameterized with atomistic calculations to compare nanotubes with a circular and polygonal cross section. The model shows that for TiS_2 nanotubes with some chiralities the radius at which a polygonal shape becomes energetically favorable is approximately 15 Å. Due to the higher strain energy and lower interfacial energy the critical radius for polygonal formation of MoS_2 nanotubes is 36 Å. Both of these values are below the typical radius of TiS_2 and MoS_2 nanotubes seen experimentally, indicating that for certain chiralities polygonal nanotubes should form.

We also investigate the potential of inorganic nanotubes as energy storage materials. First principles calculations on curved surfaces and distorted slabs are used to analyze the effect of curvature and stacking on voltage and diffusion properties. The effect is qualitatively and quantitatively dependent on the material and structure. The Li voltage on the surface of TiS_2 nanotubes decreases with a decreasing radius whether lithium is inside or outside of the nanotube. On the surface of MoS_2, the voltage decreases with decreasing radius when Li is inside the tube, but increases with decreasing radius when Li is outside the tube. The activation barrier for lithium diffusion increases with decreasing radius whether Li is outside or inside the nanotube while the barrier decreases in either case for MoS_2. When the stacking is disordered the lithium voltage and activation barrier between TiS_2 layers decreases, although the decrease in voltage is not as large as the decrease in activation barrier because the stable lithium site changes from the octahedral site to the tetrahedral site at some stacking arrangements.

Thesis Supervisor: Gerbrand Ceder
Title: R. P. Simmons Professor of Materials Science and Engineering

Acknowledgements:

First of all I would like to thank my daughter Cassie and my sons Kyle and Jacoby, each of whom wrote a chapter of this thesis, and my wife Lori who wrote the other three chapters. Seriously, no matter how stressful things got, Cassie always brought a smile to my face and so did the twins, when I had time to smile. I could not have accomplished this without the love and support of Lori as well.

Of course I want to thank Professor Ceder, my advisor. Thermodynamics with Lord Ceder as a teacher was an incredible way to start the MIT experience. His knowledge and insight has been an inspiration throughout my time here. On top of that, he's a great puppeteer.

Dane Morgan and Chris Fischer were the first two people I worked with here and both of them were always willing and able to help whenever I needed it. I want to thank Kathryn Simons, who knows everything that no one else knows. Caetano Miranda was extremely helpful in his brief time here at teaching me all the important details of VASP. Shirley Meng was a big help at getting me started on my thesis project.

I want to thank everyone else in the cedergroup for making my time here that much more enjoyable. In no particular order, Tim Mueller, Kisuk Kang, Ashley Predith, Kristin Persson, Maria Chan, Lei Wang, Byoungwoo Kang, Byungchan Han, Fei Zhou, Anton Van der Ven, Hinuma Yoyo, Thomas Maxisch, Robert Doe, Denis Kramer, Geoffroy Hautier, Anubhav Jain, Shin Young Kang, Rahul Malik, Jae Chul Kim, Xiaohua Ma, Charles Moore, Shyue Ping Ong, Ruoshi Sun, Yabi Wu, Lusann Yang and Osman Okan.

Thanks to Professor Marzari and Professor Gradecak for agreeing to be on my committee and bearing with me as my thesis topic evolved. Also thanks to Professor Allen and Professor Gibson for making me feel welcome at the university.

Thanks also to the rest of my family for their support as well as my wife's family.

Thanks to our cats Georgie and Sonia, but not Maggie, she was kind of a pain.

Contents

List of Figures

List of Tables

Chapter 1

Introduction

1.0 Overview

Inorganic layered nanotubes constitute a large portion of the nanotubes that have been synthesized to date. These nanotubes can be useful for energy storage or other applications. It would be useful to predict the properties of these tubes through atomistic calculations, but there are two barriers to accurate calculations for nanoparticles: The number of atoms is often too large for many types of calculations and the precise structure is not always well known. In this thesis I will present a structural model for nanotubes consisting of a polygonal cross section instead of a circular cross section. This model is assessed using atomistic calculations of curved surfaces, which simulate the nanotube environment with fewer atoms. The curved surface method is also used to investigate how lithium storage properties of nanotubes vary from the bulk form of the material. In this chapter I will introduce inorganic nanotubes, atomistic calculations for nanoparticles, the polygonal model and energy storage materials. I will also give an outline of the chapters in this thesis.

1.1 Inorganic Nanotubes

Over the past 20 years, nanoparticles have drawn considerable interest in the scientific community [1-5]. These particles come in many different shapes and have been assigned many different names, including nanodots, nanowires, nanotubes, nanosheets and nanoribbons. Nearly every day, a different material is synthesized in nanoparticle form. These nanoparticles of many different shapes and materials bring the potential for beneficial materials properties.

Nanotubes are one of the more commonly studied types of nanoparticles [6-9]. Most nanotubes are layered, meaning they consist of one or more 'sheets' of a material rolled into a tubular form. Inorganic nanotubes include all non-carbon nanotubes. In this thesis the focus is on layered nanotubes of the form MX_2 (M=transition metal, X=S, Se) with calculations performed on TiS_2 and MoS_2. However, the concepts discussed can easily be applied to any layered nanotubes, inorganic or carbon. A thorough history of nanotubes is given in the next chapter.

1.2 Atomistic Calculations

With the large variety of nanotubes to choose from it can be difficult to find the optimum material and tube size for a given application. Synthesizing many different nanotubes in order to investigate their properties can be costly and time consuming. Fortunately, with theoretical calculations it is possible to predict the properties for a given nanotube without the need to synthesize the particle [10-20]. This can be difficult because the number of atoms in the unit cell of a nanotube is often too large for theoretical calculations. In these cases it is necessary to estimate the properties for the nanotube using other calculations. This can be done by examining tubes of a much smaller size and extrapolating the results to the desired size. Alternatively, it is sometimes possible to simulate the nanotube environment in order to predict a particular property [17, 20]. In the work discussed here, the nanotube environment is simulated using curved surfaces, which can replicate the curvature of the tube with considerably fewer atoms.

1.3 Polygonal Model

The first step in predicting properties of a nanotube is determining its structure. While there are experimental techniques to analyze the structure, it is not always possible to determine everything about the atomic configuration, such as how the atoms in one layer are oriented relative to the atoms in the next layer. This is important to many properties, especially properties relevant to energy storage because intercalates in energy storage applications reside between the layers. In this thesis I examine two possible structures for a layered nanotube, a circular cross section and a polygonal cross section. The cross section of the nanotube largely determines how the atoms in consecutive layers are oriented. A polygonal cross section can lower the interfacial energy, by providing a coherent interface, at the expense of increased strain energy. An energy component model was used to estimate and compare the energy of these two structures. The model was parameterized with atomistic calculations using the curved surface method. The results will show that there is a critical radius, above which a polygonal cross section becomes energetically favorable.

1.4 Energy Storage Applications

One of the important areas of technology where layered nanotubes can make a large impact is energy storage and conversion. There have been many examples of layered nanotubes and layered bulk materials storing lithium, hydrogen or other intercalates [21-24]. A lot of research is focused on the search for materials that can store more energy and provide more power, in addition to being safe and cost effective. The short length scales in nanotubes can improve the speed with which the material can be charged and discharged, thus increasing the available power. In addition, the structure of some nanotubes provides more room for storage and diffusion of lithium, hydrogen and other energy storage intercalates.

Atomistic calculations can be used to estimate the capacity of a material within a given voltage range as well as the mobility of intercalates in the material. The mobility determines the rate of charge and discharge. In this thesis the effect of nanotube structure on Li mobility and voltage is examined using curved surfaces and distorted slabs, as discussed in chapter 3. The calculations show how these properties are affected by curvature of the surface and stacking of nanotube layers.

1.5 Importance of Work

Atomistic calculations have become an important part of many investigations in materials science. However, the use of these calculations has been limited in regards to nanotubes because of the absence of small periodic unit cells. Increases in computing power have resulted in a recent increase in the computational studies of nanotubes, but these studies are still usually limited to single-walled nanotubes. Most nanotubes created are multi-walled nanotubes, so an understanding of the interface between layers is crucial when trying to predict nanotube properties. One important contribution of this work is the methods developed to simulate a nanotube environment without the need for the full nanotube unit cell. This was accomplished with the use of curved surfaces and distorted slabs.

Knowledge of the exact structure of the nanotube is required to predict properties. This was the motivation for investigating the possibility of polygonal nanotubes. The results of the polygonal nanotube study show that polygonal nanotubes can, in fact, reduce the overall energy of the nanotube. This structural information is an important contribution to the computation of nanotube properties.

Many experimental studies have shown that nanotubes can have improved rate capabilities compared to the bulk material. The results shown in chapter 5 agree with these studies in that diffusion of lithium on the surface and between nanotube layers was shown to be dramatically better than bulk diffusion. This understanding of why rate capabilities of nanotubes can be better than in the bulk materials will be useful in determining which nanotubes will be optimal for battery applications.

1.6 Chapter Outline

In chapter 2, a history of nanotubes is presented. This starts with the discovery of carbon nanotubes in 1991 and continues with the numerous inorganic nanotubes that have been discovered since this time. The different synthesis methods used to create nanotubes are discussed as well as applications for nanotubes, with a focus on energy storage applications. I also review the literature on polygonal nanotubes. Most of this is in reference to carbon nanotubes, but polygonal boron nitride and molybdenum disulfide nanotubes are also discussed.

Chapter 3 contains an overview of theoretical calculations. This includes a brief introduction to density functional theory, but is focused on the specific methods used in this work. These methods are the elastic band method to calculate activation barriers, the curved surface method to simulate nanotube curvature and distorted slabs to simulate nanotube stacking. The parameters used in the calculations are also given in this chapter.

The polygonal model is presented in chapter 4. The energy component model used to compare polygonal nanotubes to circular ones is explained and the results used to parameterize this model are shown. With these results the nanotube radius at which polygonal nanotubes are energetically favored is estimated. The effect of chirality and lattice parameters on the polygonal structure is also discussed.

Calculations on lithium voltage and mobility in TiS_2 and MoS_2 nanotubes are presented in chapter 5. The effect of curvature on the surface properties of lithium is explained as well as the effect of stacking disorder on the same properties when lithium is between nanotube layers.

Conclusions and recommendations for future work are included in chapter 6. The main results are summarized and the effect of a polygonal structure on lithium properties is theorized. Some possibilities for future experimental and computational work inspired by this thesis are also presented.

Chapter 2

Inorganic Nanotubes

2.0 Introduction

The term nanotube encompasses a broad range of materials, sizes and structures. Nanotube diameters can be one nanometer [25-29] or over one hundred nanometers [30-33]. Lengths are typically on the order of microns [26, 34, 35], but nanotubes with lengths of 100-200 nm are not uncommon [36-38]. While carbon nanotubes are the most well known there are many types of inorganic, or non-carbon, nanotubes [4, 6-9]. Carbon nanotubes and most of the inorganic nanotubes discovered in the 1990s were layered nanotubes [4, 6-9, 34-35, 39]. There have also been many non-layered nanotubes [31, 40-42], especially in recent years. Several applications have been discovered for these nanotubes and as investigations into different nanotube types and properties intensify, many more will be discovered.

2.1. History of Nanotubes

In 1991 Iijima reported graphitic carbon needles of 2 to 50 layers with diameters from 4 to 30 nm and lengths up to 1 micron [39]. This discovery sparked a tremendous amount of research into nanotubes. There was previous interest in carbon fibers, which typically had diameters of 7-15 μm, although fibers with diameters of 100-500 nm were reported in 1987 [43]. Later examination [44] showed that these fibers had a carbon nanotube core with a polygonal shell. In addition, prior to Iijima's discovery, studies showed that MoS_2 layers have a tendency to fold and occasionally form tubes [45-46].

Shortly after Iijima's discovery it was theorized that other layered materials would be unstable versus bending and thus form tubes [36]. This was verified in 1992 with the synthesis of WS_2 nanotubes with diameters of ~10 nm and lengths of ~200 nm [36]. In 1995 MoS_2 nanotubes with diameters of 10-20 nm and lengths up to 5 μm were produced [35]. Boron nitride nanotubes, which are similar in structure to Carbon nanotubes, were discovered in 1995 [38]. These nanotubes had diameters of a few nanometers and lengths of ~200 nm. Over the last decade, nanotubes of many different materials have been synthesized [4, 6-9]. The majority of these materials were layered materials, but many non layered nanotubes have also been created. Table 2.1 lists the year of synthesis for many inorganic nanotubes.

Formula	**Year of Synthesis**
WS_2	1992
MoS_2, BN	1995
TiO_2	1998
Co, Fe	2000
$MoSe_2$, WSe_2, NbS_2, TaS_2	2001
TiS_2, HfS2, ZrS_2,	2002
$TiSe_2$, $NbSe_2$	2003
ZrO_2	2004
Ag, Cu, B, Se, Te	2004
VS_2	2005

Table 2.1: Formula and year of first synthesis for several inorganic nanotubes

2.1.1 Layered Nanotubes:

There are many materials that have a layered structure in the bulk form. The structure of these materials consists of several 'sheets'. The atoms in each sheet are bound together with short range atomic forces. The sheets are bound together by long range Van der Waals forces. These are weak forces caused by correlations in the fluctuating polarizations of nearby particles. A common example of a layered material is graphite. Graphite consists of single atomic layers of carbon arranged in a planar hexagonal arrangement. Several of these sheets are held together by a Van der Waals attraction. Boron Nitride has the same structure as graphite with carbon atoms replaced by Boron and Nitrogen. There are several layered materials of the form MX_2 (M=transition metal, X=S, Se). In these materials the sheet consists of a layer of transition metal cations sandwiched between layers of anions. Many MX_2 materials have been synthesized in nanotube form. These MX_2 nanotubes are the focus of this thesis, specifically MoS_2 and TiS_2 nanotubes. Figures 2.2 and 2.3 show TEM images of MoS_2 and TiS_2 nanotubes, respectively.

The basic structural unit of layered nanotubes is the sheet described earlier. MoS_2 and WS_2, the first inorganic nanotubes discovered, are layered nanotubes from the MX_2 class of materials. Other nanotubes from this class include TiS_2, $TiSe_2$, $MoSe_2$, WSe_2, NbS_2, ZrS_2, HfS_2, $NbSe_2$ and VS_2 [35-36, 38, 47-49]. Single-walled nanotubes consist of one of the sheets rolled into a tube [25-29]. Multi-walled nanotubes can consist of several concentric single-walled nanotubes [35-36, 39, 48] or a single sheet rolled into a scroll [50-52]. There is also evidence of multi-walled nanotubes that contain both concentric tubes and scrolls [53].

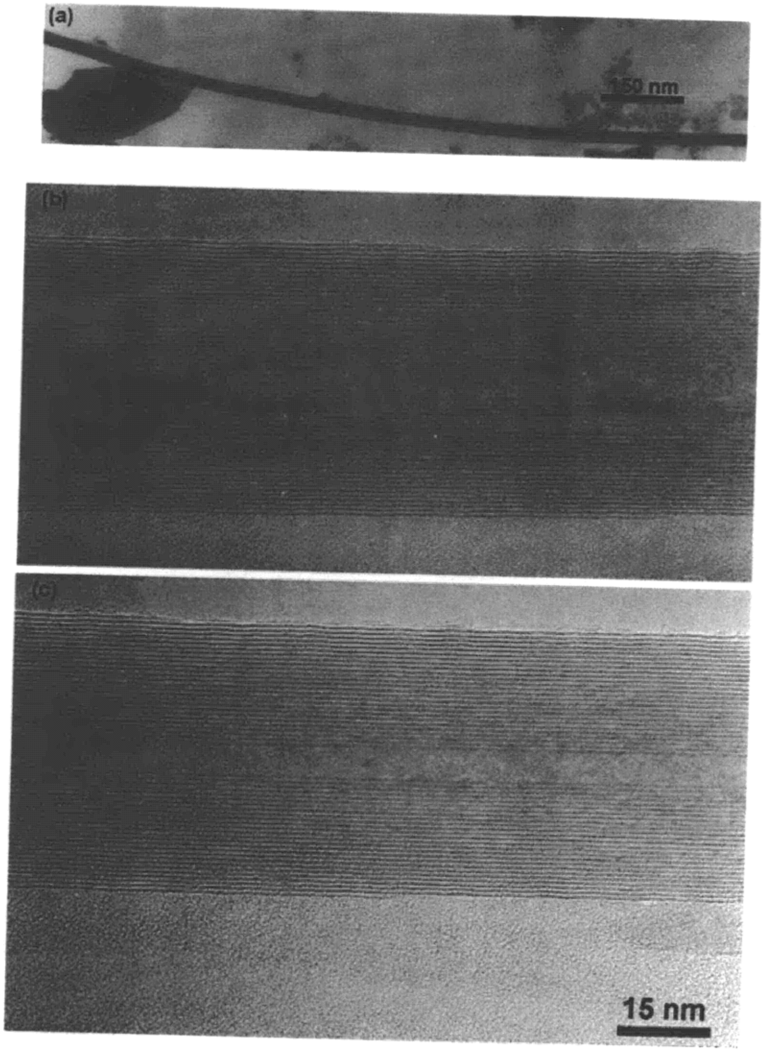

Figure 2.1: TEM images of multi-walled MoS_2 nanotubes [180]

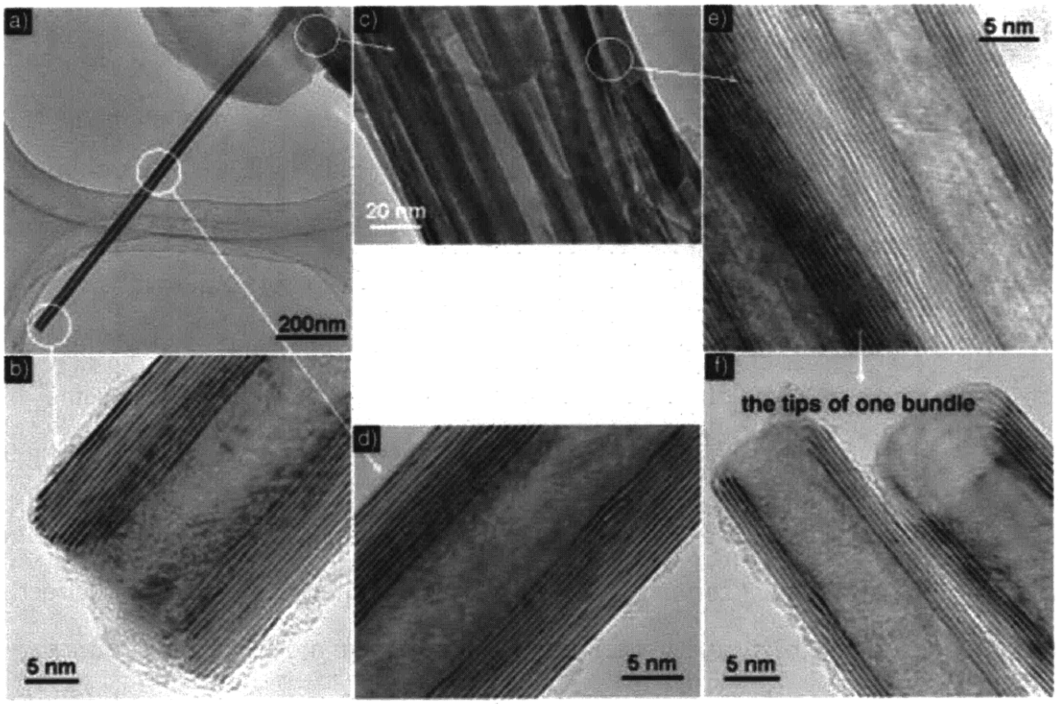

Figure 2.2 : TEM images of multi-walled TiS_2 nanotubes [104]

2.1.2 Synthesis of Layered Nanotubes:

Many different techniques have been employed to synthesize layered nanotubes. Early multi-walled carbon nanotubes were created through arc-discharge evaporation of carbon in an argon-filled vessel by Iijima and later by Ebbessen and Ajayan using helium instead of argon [54]. Other techniques used to produce carbon nanotubes include laser ablation [55], chemical vapor deposition (CVD) [56-57], electrochemical techniques [58] and templating techniques [59]. Arc discharge and CVD techniques have also been employed to created boron nitride nanotubes [38, 60].

Arc discharge and laser ablation have also been employed to create WS_2, MoS_2 and $MoSe_2$ nanotubes [61-63]. However, chemical decomposition techniques are more commonly used to create MX_2 nanotubes. The first WS_2 (MoS_2) nanotubes were created by heating Tungsten (Molybdenum) foils on a quartz substrate with H_2S gas flow [35-36]. MoS_2 and WS_2 tubes have also been produced with starting materials of MoO_3 and WO_3 instead of the metal. By replacing HS_2 with HSe_2 in this process selenide nanotubes, such as $MoSe_2$ and WSe_2, can be created [64-65]. After it was determined that MoS_3 and WS_3 are intermediates in the process of converting oxides to disulfide nanotubes, many MX_2 nanotubes, including TiS_2, HfS_2 and NbS_2, were created by direct decomposition of the trisulphides [47-48]. Diselenide nanotubes have also been produced with the triselenides as the starting material [66]. Hydrothermal treatment has been used to produce vanadium oxide nanotubes [67]. Ma et al. transformed 2D nanosheets to nanotubes through intercalation and deintercalation of Sodium ions. This method produced nanoscrolls of titanium dioxide, manganese dioxide and niobate [50]. Du et al synthesized potassium hexaniobate nanoscrolls through exfoliation of polycrystalline $K_4Nb_6O_{17}$ [68]. TiO_2 nanotubes have been produced by mixing TiO_2 powder with NaOH [69-71].

There are several other methods that have been used to synthesize layered nanotubes, but these are some of the most common techniques. The method of synthesis can affect nanotube size, yield and structure. Low temperature routes are more likely to produce nanoscrolls [3]. While closed nanotubes are typically more stable than nanoscrolls [2], the kinetic barrier for forming closed tubes is difficult to overcome at low temperature. Minor variation of a synthesis technique will often affect the ratio of nanotubes to nanoparticles produced as well as the diameter of the nanotubes.

2.1.3 Non-Layered Nanotubes:

Although the focus of this thesis is on layered inorganic nanotubes, I will give a brief overview of non-layered nanotubes. Recently many nanotubes of materials that are not layered have been produced [31, 40-42]. These nanotubes will often contain many defects or have a large amount of strain due to the large variation from the bulk structure. Synthesis is generally accomplished by depositing the material in a porous membrane [72]. This technique has been used with alumina membranes to produce Ag and Cu nanotubes [41, 73]. Other templates have been utilized to create bismuth, boron, selenium and tellurium nanotubes [74]. TiO_2 is a layered material, but amorphous TiO_2 nanotubes, which are non layered, have been created by anodizing Ti films in a HF aqueous solution [75]. Figure 2.3 shows SEM images of Cu nanotubes.

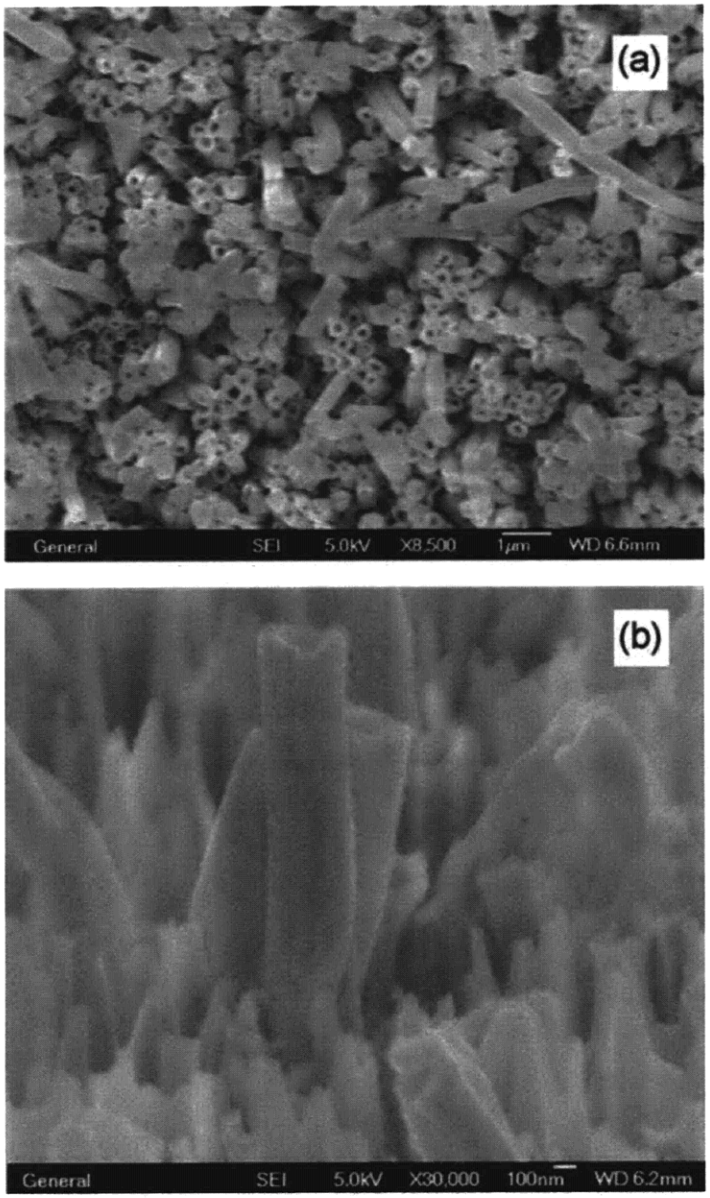

Figure 2.3: SEM image of Cu nanotubes [41]

2.2 Nanotube properties and applications

Nanotubes possess many materials properties that are different from the bulk form of the same material. This is due to the high surface to volume ratio, low number of defects and finite size effects. These properties have resulted in many beneficial applications for nanotubes. Due to the variety of nanotubes that have been synthesized there are likely many more applications yet to be discovered.

The extraordinary strength of carbon nanotubes has led to the creation of nanotube sheets, foams and ropes. Functionalized CNT have been used as biomedical delivery agents, biosensors, electrodes, in artificial bone construction, as supercapacitors and in many other applications [1, 76]. WS_2 and MoS_2 nanotubes have proven to be effective solid lubricants [77]. WS_2 nanotubes also display shock wave resistance [78] and have been used as tips in scanning probe microscopy [79]. TiO_2 nanotubes have been used as hydrogen sensors, dye sensitized solar cells, and have displayed photoluminescence properties [80-82]. $NbSe_2$ nanotubes have shown superconducting properties [66].

2.2.1 Energy Storage

Layered materials have been studied extensively for energy storage applications [83]. The gap between the layers of these materials is often ideal for intercalates, such as hydrogen and lithium. TiS_2 was one of the first materials considered for lithium rechargeable batteries [84-85]. Nanoparticles in general have attracted great interest as energy storage materials [23, 86], because the short length scales in these materials often improve rate capabilities. Not surprisingly, carbon nanotubes and many inorganic layered nanotubes have shown the ability to store hydrogen, lithium, and other intercalates [21-22, 24, 86].

2.2.1.1 Hydrogen Storage

Ma et al. studied hydrogen storage in BN nanotubes [87]. Bamboo-like and multi-wall nanotubes were examined, storing 2.6 and 1.8 wt % of hydrogen, respectively, at room temperature and a pressure of 10MPa, compared to 0.2% for bulk BN powder. The lower value for multi-walled tubes is due to the closed ends, which prevent hydrogen from diffusing to the interior of the tube. Multi-layered TiO_2 nanotubes were shown by Bavykin et al. to adsorb hydrogen [88]. Hydrogen uptake ranged from 1.3 wt % at 100° C and 0.4 bar to 3.8 wt. % at -196° C and 6 bar. TiS_2 nanotubes were able to store 2.5 wt % hydrogen at 25° C and 4 MPa [89].

The hydrogen storage was reversible, but multiple cycling resulted in several defects. Chen et al. [90] were able to electrochemically charge and discharge MoS_2 nanotubes with 0.97 wt % hydrogen at 20° C and 50 mA/g charging rate. These nanotubes also exhibited gaseous hydrogen storage up to 1.2 wt % at 25° C and 1.5 MPa [91].

2.2.1.2 Lithium Storage

There have been numerous studies of lithium storage in TiO_2 nanotubes, including voltage profiles and rate capabilities. The results for anatase [92-95], TiO_2 – B [96] and H-titanate [97] nanotubes were similar. The maximum capacity was approximately 300 mAh/g for all studies. The capacity loss after the first cycle was as low as 14% [95]. The rate capabilities of these nanotubes were very good, with 96 mAh/g capacity at a 21C rate [96]. One study [93] showed higher capacity after 100 cycles with a rate of 2C compared to the capacity at a rate of 0.1C. Several investigations into lithium storage of Vanadium Oxide nanotubes have been reported [67, 98-99]. The first study [67] showed a maximum capacity of 180 mAh/g with nearly 50% capacity loss after 10 cycles. The cyclability and maximum capacity were greatly improved by changing the potential window from 1.5-4.0V to 1.4-3.6 V [99]. Manganese Vanadium Oxide nanotubes were also shown to intercalate lithium to 140 mAh/g in a voltage window of 2-3.5 V [100]. Bundles of single-walled MoS_2 nanotubes with diameters of 1 nm were capable of storing lithium up to a capacity of 500 mAh/g in the first cycle, but more than half of the capacity was irreversible [101]. Most of the lithium is stored in the channels between nanotubes with some lithium forming small metallic particles [102]. Bundles of WS_2 nanotubes intercalated lithium with a capacity of 915 mAh/g in the first cycle [103]. Subsequent cycles showed a capacity of 600 mAh/g. The voltage window for this study was large, 0.1 – 3.1 V, and it is thought that lithium is stored between tubes and in the core of the nanotube in addition to between the layers of the nanotube. Lithium was chemically intercalated into TiS_2 nanotubes up to $LiTiS_2$ (~225 mAh/g) [104]. Full lithiation resulted in a 10.5 % increase in the c-lattice parameter, which also occurs in bulk TiS_2.

In addition to nanotubes, several different types of nanowires have shown promising lithium storage capability. Silicon nanowires were investigated for their potential as anode materials in rechargeable lithium batteries [105]. These nanowires have a capacity more than 10 times that of graphite and show dramatic improvement in cyclability compared to bulk silicon. Cobalt oxide nanowires synthesized and assembled with viruses displayed high capacity at rates up to 5C [106]. Tin oxide nanowires show improved capacity and cyclability compared to SnO_2 powder [107]. TiO_2 nanowires have similar lithium storage properties to TiO_2 nanotubes [108]. Vanadium pentoxide nanoribbons have display completely reversible lithium insertion at rates up to 360C [109].

2.2.1.3 Other Intercalates

Other materials besides lithium and hydrogen have been intercalated into layered nanotubes. TiS_2 nanotubes were shown to reversibly store magnesium [110]. The capacity in the first cycle was 236 mAh/g at a rate of 10 mA/g. After 80 cycles the capacity was reduced to 180 mAh/g. The capacity as a function of temperature was also studied, showing a 22% decrease in capacity when the temperature was raised from 20° C to 60° C. Vanadium oxide nanotubes have also intercalated magnesium [111]. The capacity for these tubes was 75 mAh/g at a rate of 5 mA/g with a voltage window from 0.2-0.8 V. In addition to magnesium, Na, K, Ca, Sr, Fe, Co, Ni and Cu have also been intercalated into vanadium oxide nanotubes [112]. VS_2 nanotubes have electrochemically intercalated Cu up to $Cu_{0.77}VS_2$, approximately 360 mAh/g, with a reversible capacity of 314 mAh/g [113].

2.3 Polygonal Nanotubes

In this thesis a model is presented to compare the energy of layered nanotubes with a polygonal cross section to those with a circular cross section. There is previous evidence of polygonal nanotubes, predominantly carbon nanotubes.

Two years before Iijima's discovery of carbon nanotubes, graphitic carbon needles with diameters as small as 100 nm were shown to have an outer shell with a polygonal cross section [44]. Two years after the discovery of carbon nanotubes, investigations of the helicity of carbon nanotubes revealed that some of the nanotubes had polygonal cross sections [114]. The focus of this study was on the helix angles of the nanotubes, specifically the observation that the helix angle changes every 3 to 5 nanotube layers. The authors theorize that this change in helicity occurs because it results in lower interfacial energy. This is also presented as the main reason for polygonal nanotube formation, although they suggest that defects at the polygon corners play a role in the formation of polygonal nanotubes. Carbon nanotubes have a layer spacing of 0.34 nm [39], which is approximately 2% larger than the spacing seen in bulk graphite. This layer spacing corresponds to graphite with disordered stacking [115]. High temperature treatment (HTT) of multi-walled carbon nanotubes [116] caused graphitization of the nanotubes. The interlayer spacing of the nanotubes subjected to HTT decreased and the (002) peak became much sharper. This indicated the stacking became more ordered. For nanotubes with diameters greater than 50 nm, polygonization of the nanotubes was observed. The authors proposed that the transformation from disordered to ordered layer stacking drove the formation of polygonal nanotubes. There are multiple reports of polygonization of single-walled carbon nanotube bundles under pressure [117-118]. This is partly due to the interaction between layers of neighboring nanotubes, similar to the interaction between layers of multi-walled nanotubes. In addition, polygonalization lowers the total energy when the nanotube bundles are forming a hexagonal close packed structure. Graphitic polyhedral crystals have been studied extensively [119-121]. These have diameters from 100 to 1000 nm with a carbon nanotube core and a polygonal outer shell. Images of graphitic polyhedral crystals are shown in figure 2.4.

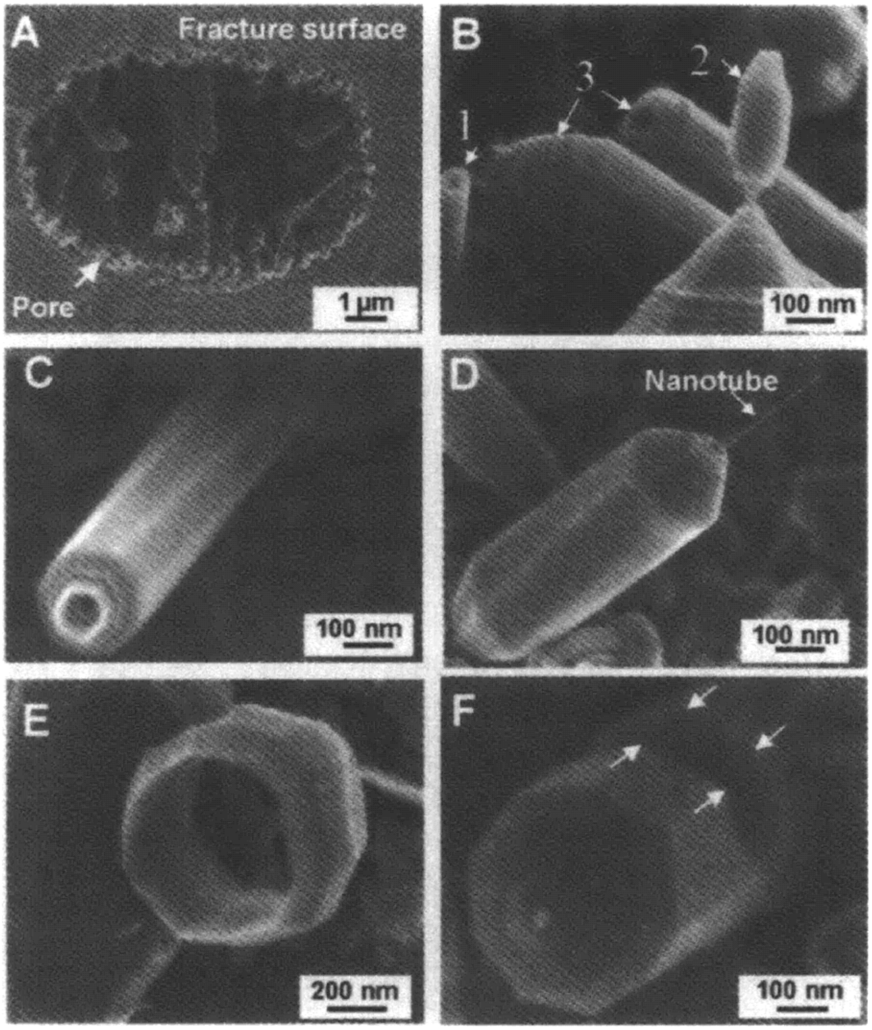

Figure 2.4: Graphitic polyhedral crystals showing a polygonal shell with a circular core [125]

Most inorganic nanotubes, especially the dichalcogenide structures, do not have a known disordered stacking phase like that seen in graphite. Many of these materials have ionic bonding [122]. When there is an incoherent interface in these materials, the cations in consecutive layers are closer together, likely resulting in a larger interfacial energy than that for carbon nanotubes. This should increase the likelihood of polygonal nanotubes, however there are only a few reports of inorganic nanotubes with a polygonal cross section. Multi-walled Boron Nitride nanotubes with perfectly stacked, polygonal in cross section regions have been reported [123-124]. These nanotubes are not completely polygonal, but partially polygonal and partially circular. There is also evidence that some WS_2 nanotubes have a polygonal cross section [125], although it was theorized that this was due to the polygonal nature of the WO_3 nanorods from which these nanotubes were formed.

2.4 Computational Nanotube Studies

There have been numerous computational studies of nanotubes. The majority of these studies are of carbon nanotubes [15-17, 126-129]. I will not go into detail on theoretical calculations of carbon nanotubes, except for the studies relevant to this thesis. The electronic properties of multi-walled polygonal carbon nanotubes were studied [18], showing that modified low-lying conduction bands are introduced either into the bandgap of insulating nanotubes or below the degenerate states that form the top of the valence band of metallic tubes. The effect of pressure on bundles of single-walled carbon nanotubes was studied using continuum elasticity theory [118]. It is reported that single-walled CNT in hexagonal close packed bundles begin to facet before pressure is applied. The amount of faceting increases with pressure and this change is reversible up to 4 GPa. In addition, they report that the intertubular gap in these bundles is below that of bulk graphite even at normal pressure. There are many other studies on the effect of pressure on bundles of single walled nanotubes [117, 130-133]. Lee and Marzari studied covalent functionalizations that preserve or control the conductance of single-walled metallic carbon nanotubes [134]. This study used a method very similar to the curved surface method used in this thesis and described in chapter 3.

Although most computational studies of nanotubes are of carbon nanotubes, the number of studies of inorganic nanotubes has grown steadily in recent years. Srolovitz et al. investigated defect formation in nanotubes using a theory of the bending of crystalline films [135]. The study predicted a transition from a bent coherent film with no dislocations to an incoherent, dislocated film as either film thickness (nanotube wall thickness) or curvature is increased. Bishop and Wilson [19] examined the energetics of inorganic nanotubes with atomistic and continuum models. Hexagonal INTs, which includes most dichalcogenide nanotubes, display folding energetics consistent with a continuum model. However, square-net INTs display folding energetics strongly dependent on the direction along which the sheet is folded. Enyashin et al. [136] reported on the importance of considering coulomb interactions in addition to strain energy when studying stability of MX_2 nanotubes. This is in contrast to studies of carbon nanotubes, in which consideration of strain energy is generally sufficient. It was determined that among sulfide nanotubes, those with octahedral coordination are the least stable, while the tubes with trigonal prismatic coordination are the most stable.

There are several reports on theoretical studies of BN, BC_2N and BC_3 nanotubes [137-140]. The calculations show that N-N and B-B nearest neighbor pairs do not provide a stable nanotubular structure. These studies also showed that BN nanotubes are insulating with a wide band gap of 5.5 eV. There have been multiple studies on hydrogen adsorption on boron nitride nanotubes. Jhi and Kwon showed that the binding energy of hydrogen on BN nanotubes is 40% larger than on carbon nanotubes [141]. Wu et al. studied chemical adsorption of H atoms on (8,0) zigzag BN nanotubes using DFT, determining that H prefers to adsorb on the top sites of adjacent B and N atoms [142]. This group also studied the effect of defects on H_2 dissociation [143]. This study showed that without defects, hydrogen dissociation is endothermic with an energy barrier of 2.0 eV. In the presence of defects, dissociation becomes exothermic and the barrier reduces to about 0.67 eV. Han et al studied collision and adsorption of hydrogen on single-walled BN nanotubes [144]. Energies between 14 and 26 eV are needed for hydrogen molecules to dissociate without damaging the nanotube walls.

Multiple theoretical investigations of MX_2 and oxide nanotubes have been undertaken. Enyashin and Seifert studied TiO_2 nanotubes using Density Functional Tight Binding (DFTB) calculations [10]. Anatase nanotubes are the most stable nanostructure of TiO_2 and are semiconductors with a direct band gap of approximately 4.2 eV. Lepidocrocite nanotubes are also semiconductors, but have an indirect band gap of 4.5 eV. Ivanovskaya et al. compared TiO_2 and VO_2 nanotubes using the tight binding method [11]. Zigzag and armchair TiO_2 nanotubes are semiconducting and the band gap tends to vanish at small diameters. At small diameters zigzag nanotubes are more likely to form, but at larger diameters armchair nanotubes are more stable. In contrast, all VO_2 nanotubes are metal-like and armchair tubes are more stable at all diameters. Ivanovskaya and Seifert studied titanium disulfide nanotubes using DFTB [12-13]. They determined that the octahedral coordination is preferable to the trigonal prismatic coordination. All single-walled TiS_2 nanotubes are semiconducting regardless of chirality and diameter, but the band gap decreases with decreasing radius. Enyashin and Ivanovskii used the tight binding model to study defects in TiS_2 nanotubes [14]. The most stable defects are S vacancies in the inner cylinder. All defects lead to a semiconductor-metal transition.

In this thesis computational studies of TiS_2 and MoS_2 nanotubes are discussed. These studies are used to investigate the structure of the tubes and their potential as energy storage materials.

Chapter 3

First Principles Calculations

3.0 Introduction

With atomistic calculations it is possible to predict many properties of materials where the only required knowledge is the composition of the material [145-146]. The structure type must also be known, but given a short list of possible structure types, calculations can be used to determine the low energy, and thus stable, structure type. This field of computational materials science has benefited considerably from the Moore's Law scaling of computation speed. As computers get faster and cheaper, more calculations and calculations on larger systems can be performed.

These techniques have been used to predict crystal structures [147-148], phase diagrams [149-150], mechanical properties [151-152], electrochemical properties [153-154] and many other properties. There is even work going on involving "high throughput" automated calculations as a way of scanning many different materials for a desired property [155-157]. In this chapter I will give a brief introduction to Density Functional Theory (DFT) and discuss the specific techniques used for calculations discussed in the next two chapters.

3.1: Density Functional Theory

Knowledge of the energy of a collection of atoms in different configurations is sufficient to predict many materials properties. The structure with the lowest energy will be the stable structure. Elastic constants can be derived from the change in energy as the material is stretched or compressed. The difference in energy between lithium in the anode and in the cathode determines the voltage of the material. First principles calculations, or atomistic calculations, determine this energy by solving the Schrodinger Equation.

$$H\psi = E\psi \tag{3.1}$$

In the above equation ψ is the wavefunction and E is the total energy. H is the Hamiltonian operator,

$$H = T + V + U + C \tag{3.2}$$

When applied to the wavefunction, T gives the electron kinetic energy, V is the coulomb potential form electron-nucleus interactions, U is the electron-electron coulomb energy and C is the nucleus-nucleus coulomb energy, which is independent of the wavefunction. The energy must be minimized with respect to the wavefunction to give the ground state energy for a given external potential. Due to the size of the many body wavefunction, this equation cannot be solved for any real systems.

Density functional theory (DFT) [158-159] makes it possible to determine the ground state energy of a system without knowing the many body wavefunction. DFT is based on the Hohenberg-Kohn theorem [158], which says that the ground state properties of a system are uniquely determined by the electron density. With this theorem the energy of a system is much easier to determine.

$$E[\rho] = F[\rho] + V[\rho] \tag{3.3}$$

The constant term accounting for nucleus-nucleus coulomb interaction is not included. The ground state energy for a given atomic configuration is determined by finding the electron density that minimizes this energy. The electron density is designated by ρ, V is the potential energy resulting from the electron-nucleus coulomb interaction and F is a universal functional accounting for the kinetic energy of the electrons and electron-electron coulomb interaction for a given electron density.

$$F[\rho] = T[\rho] + V_{ee}[\rho] \tag{3.4}$$

If the universal functional was known, the energy could be exactly determined. However, it is not known so approximations are needed. Kohn and Sham [160] introduced an approximation to F[ρ].

$$F[\rho] = T_s[\rho] + J[\rho] + E_{xc}[\rho] \tag{3.5}$$

T_s is the kinetic energy of non-interacting electrons of density ρ and J is the classical coulomb energy. E_{xc} is called the exchange correlation energy and includes the difference in kinetic energy and coulomb energy between non-interacting electrons and real electrons. The first two terms can be exactly determined, but the exchange correlation energy is not known. Two common techniques to estimate E_{xc} are the Local Density Approximation (LDA) [160] and the Generalized Gradient Approximation (GGA) [161-162]. Under LDA it is assumed that the exchange correlation energy per electron is local, while in GGA the gradient of the electron density is included in the calculation of E_{xc}. For a more in depth description of DFT see the references [163-164].

3.2 Elastic Band Method

The activation barrier is the largest energy that must be overcome when a system goes from one state to another. For example, the activation barrier for lithium diffusion is the difference between the energy of a system when lithium in its stable site and the largest energy as lithium diffuses between two stable sites. The diffusion coefficient varies exponentially with this activation barrier.

$$D \propto e^{\frac{E_{ab}}{kT}} \tag{3.6}$$

In order to determine the activation barrier it is necessary to find the minimum energy path between two stable lithium sites. The elastic band method is used to find this path [165]. The starting point for elastic band calculations is a series of intermediate structures between the two stable end points. These are usually determined by interpolating between the endpoints. The atoms in the intermediate structures are allowed to relax according to the local energy landscape. To prevent atoms from relaxing to the endpoints, atoms in successive structures are held together with elastic band like forces (hence the name). This results is several structures constrained to be approximately equally spaced along the path between the two stable endpoints, but relaxed to a local minimum so as lie on the minimum energy path between the endpoints. The largest energy along the path, relative to the stable energy, is the activation barrier. By increasing the number of intermediate structures the precision of the activation barrier can be increased, at the expense of greater computation time.

3.3 Curved Surface Method

With first principles calculations, the computation time required for nanotubes with a radius larger than 1-2 nanometers is prohibitively long. Most inorganic nanotubes have radii greater than 5 nm, so it is necessary to simulate the nanotube environment with fewer atoms. The curved surface method was derived for this purpose [20, 134]. A curved surface is a sheet with constant curvature everywhere, with the exception of a series of inflection points. This results in a periodic structure that can have any radius of curvature without increasing the number of atoms. Figure 3.1 shows curved surfaces of TiS_2 with radii of curvature of 0.95 nm and 10 nm. These surfaces are similar to a nanotube surface everywhere except at the inflection points. While non-local properties, such as total strain energy, will not be reproduced well with these surfaces, local properties can be accurately estimated when analyzed far from the inflection points. Lithium voltage and activation barrier for diffusion can be considered local properties in this context. By placing lithium atoms as far from the inflection points as possible, lithium properties as a function of curvature can be determined, as will be shown in chapter 5.

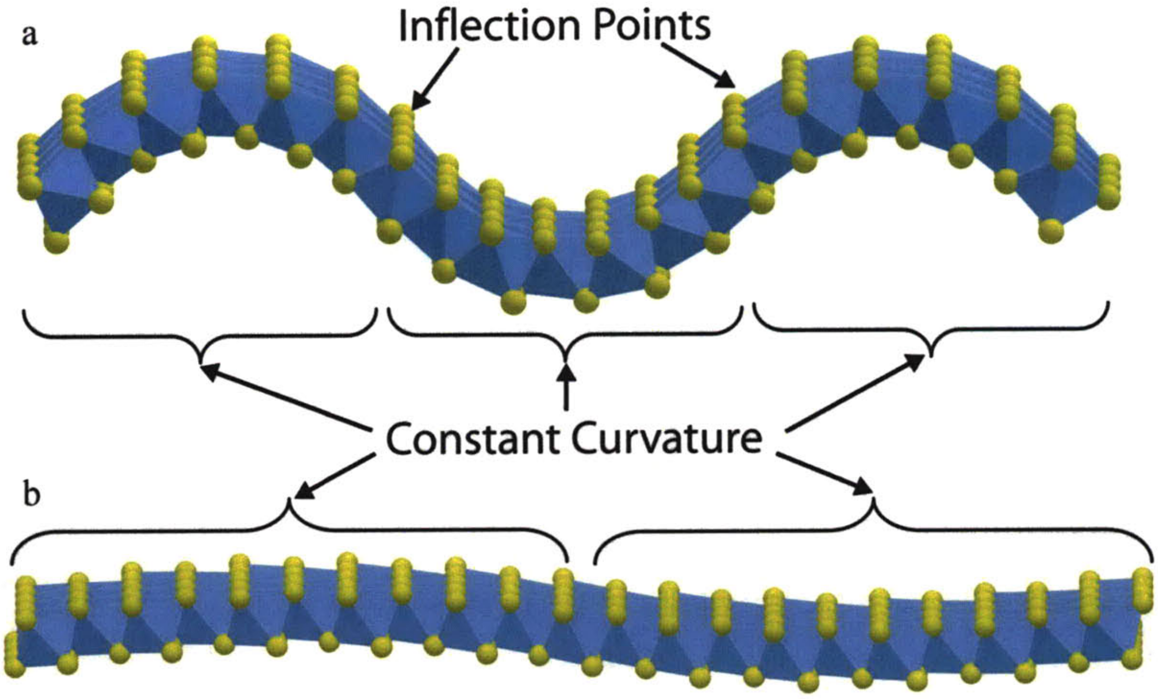

Figure 3.1: TiS_2 curved surfaces with radius of curvature of 9.5 Å (a) and 100 Å (b)

These surfaces were also used to parameterize the polygonal model described in chapter 4. This required obtaining the strain energy and interfacial energy constants. These are non-local properties that would not be assessed well with curved surfaces like those shown in figure 3.1, but modified curved surfaces were used that accurately represent polygonal nanotubes. The polygonal model consists of flat sections and curved sections. Curved surfaces were created with this same structure, as shown in figure 3.2. This figure shows a curved surface with a bend angle of 60° and a curved length of 10 Å. This corresponds to a radius of curvature of 9.5 Å. The rest of the surface has no curvature. In this case the curved segment, the flat segment and the point where the curvature changes all accurately represent the actual polygonal nanotube. By varying the curved length and the bend angle these surfaces are used to estimate the strain energy constant in chapter 4.

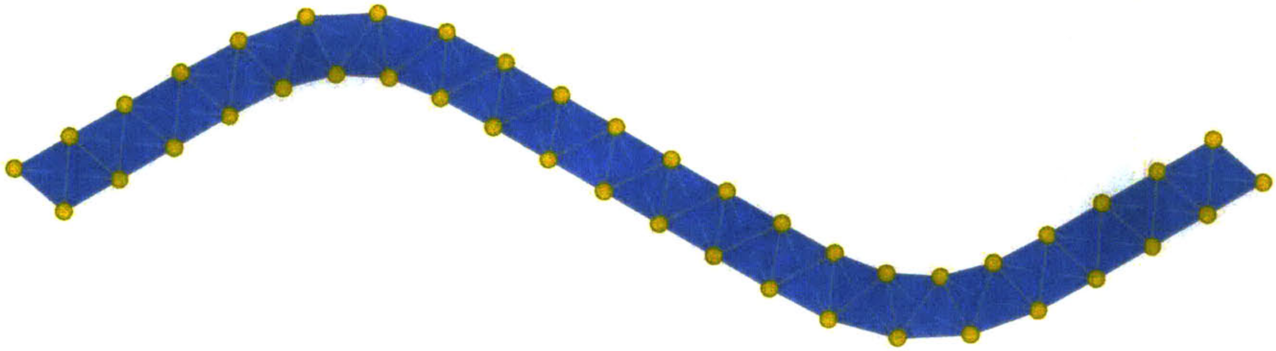

Figure 3.2: TiS_2 curved surface with a bend angle of 60°and a curved length of 10 Å.

In order to assess the interfacial energy constant a double curved surface is needed. This consists of two curved surfaces similar to the one shown in figure 3.2 stacked on top of each other. One of these double curved surfaces is shown in figure 3.3. The bend angle for this surface is 59.3° and the curved length is 10 Å for the inner curve and 15.9 Å at the outer curve. This bend angle was chosen to provide a coherent interface at either side of the curved segment without any strain required, apart from bending strain. The curved length was varied to assess the interfacial energy constant as described in chapter 4.

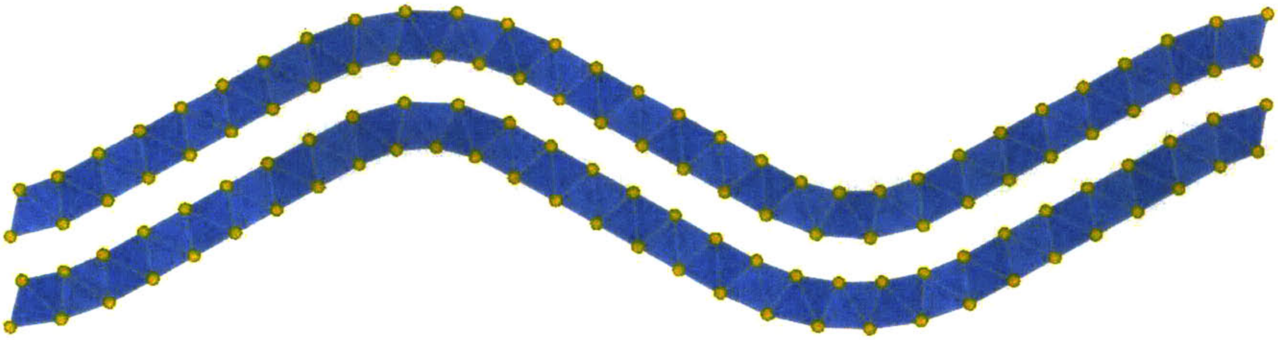

Figure 3.3: TiS_2 double curved surface with a bend angle of 59.3°and a curved length of 10 Å.

3.4 Distorted Slabs

As described in chapter 4, the difference in length between nanotube layers will result in a stacking mismatch. This will greatly affect the lithium sites between layers because lithium in these sites is coordinated with sulfur atoms from each layer. In order to determine how the stacking affects lithium voltage and activation barrier for diffusion, several structures were prepared with varying levels of stacking mismatch. This was accomplished by shifting one layer, relative to the previous layer, along one of the in plane lattice parameters. Figure 3.4 shows two layers of TiS_2 with and without a stacking mismatch. The layers in figure 3.4(a) are stacked as they would be in the bulk while in figure 3.4(b) the layers are offset by ¼ of the in plane lattice parameter. When relaxing these structures the titanium atoms were not allowed to relax in order to maintain the stacking mismatch. For each stacking orientation, lithium atoms were inserted in order to determine the stable site energy. The elastic band method was then used in order to determine the activation barrier for a given stacking mismatch.

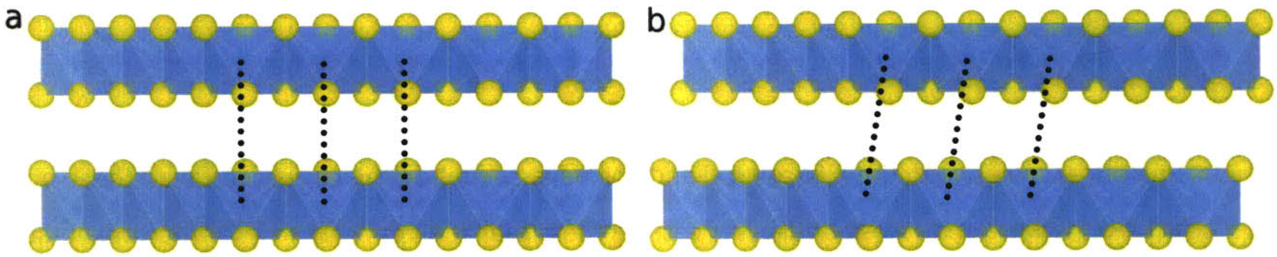

Figure 3.4: TiS_2 layers with (a) no stacking mismatch and (b) a stacking mismatch of 25% of the in-plane lattice parameter

3.5 Computational Parameters

All calculations discussed in this thesis were carried out using Density Functional Theory as implemented in the Vienna Ab-initio Simulation Package (VASP) [166-167]. We have used the generalized gradient approximation (GGA) of Perdew-Burke-Ernzerhof (PBE) to treat the exchange and correlation interaction. Projector-augmented-wave (PAW) potentials were used [168-169] with valence states $3d_3 4s_1$ for Ti, $4p_6 4d_5 5s_1$ for Mo, $3s_2 2p_4$ for S and $1s_1 2s_1 2p_1$ for Li.

Structural parameters for a TiS_2 sheet and a MoS_2 sheet, consisting of a Sulfur – Titanium (Molybdenum) – Sulfur triple layer, were determined using a 3 atom unit cell with a 15 Å vacuum layer. Atomic positions as well as unit cell shape and volume for this structure were relaxed using a 15x15x4 Monkhorst-pack *k*-point mesh (12x12x2 for MoS_2) until the forces on all atoms were less than 0.03 eV/Å.

Any periodicity along the length of the curved surface can be used in the calculations. For voltage, strain and interfacial energy calculations the minimal cell containing one Ti or Mo in the direction of the nanotube axis (~ 3.45 Å) was used. A cell twice as long was used for activation barrier calculations. For a radius of 9.5 Å these unit cells contained 36 and 72 atoms respectively. For all other radii the unit cells contained 60 and 120 atoms. When relaxing the curved surfaces the unit cell shape and volume were kept fixed and only the atomic positions of the S atoms were allowed to change. Inspection of the forces on the Ti atoms, and tests where Ti atoms were allowed to relax showed that freezing the Ti atoms did not have a significant effect on the results. Calculations were converged until all forces were less than 0.03 eV/Å with a Monkhorst-Pack *k* grid of 1x1x6.

To contrast the activation barrier for Li motion on the curved surface and in the bulk, a bulk activation barrier calculation was performed on a 2x2x2 supercell which gives about the same distance between the migrating Li and its image as that on the curved surface. These bulk calculations were converged until all forces were less than 0.03 eV/Å, with a 4x4x4 Monkhorst-pack *k* point mesh.

Activation barriers for Li motion were calculated using the Nudged Elastic Band (NEB) method with nine intermediate images. We performed a test using 19 intermediate images, yielding results within 2 meV of the results obtained with 9 intermediate images, verifying that 9 images is sufficient for these calculations. Li insertion/absorption voltages were calculated with the procedure described in the references [154,170].

Distorted slab calculations used to determine the effect of stacking on lithium voltage and activation barrier were performed using a 2x2x2 supercell. Slabs were relaxed with a 4x4x5

Monkhorst-pack *k*-point mesh until the forces on all lithium and sulfur atoms were less than 0.03 eV/Å, while Ti atoms were kept fixed.

Chapter 4

Polygonal Nanotubes

4.0 Introduction

A nanotube with a circular cross section must have either a mostly incoherent interface between nanotube layers or an excessively large amount of strain to maintain a coherent interface. This results in a large amount of excess energy relative to the bulk material. A polygonal nanotube is a nanotube with flat sides, resulting in a cross section that is a polygon rather than a circle. The flat sides can provide a mostly coherent interface between layers while increasing the bending strain energy at the corners. This structure can lower the overall energy of the nanotube, relative to a circular nanotube, due to the reduced interfacial energy. Figure 4.1 shows the cross section of a circular and polygonal nanotube.

A faceted structure is common among inorganic fullerenes, as can be seen in most reviews of these nanoparticles [3, 4, 171]. Figure 4.2 shows faceted MoS_2 and WS_2 nanoparticles. Faceted nanotubes are considerably less common, but there have been some reports of carbon and inorganic nanotubes with a polygonal cross section. The literature on polygonal nanotubes was discussed in chapter 2. There is general consensus that one reason for polygonalization of nanotubes is a lowering of the interfacial energy by providing a coherent interface between layers or nanotubes. However it is typically thought that the corners of the polygon are formed by defects. Also the importance of chirality to these polygonal nanotubes is seldom discussed.

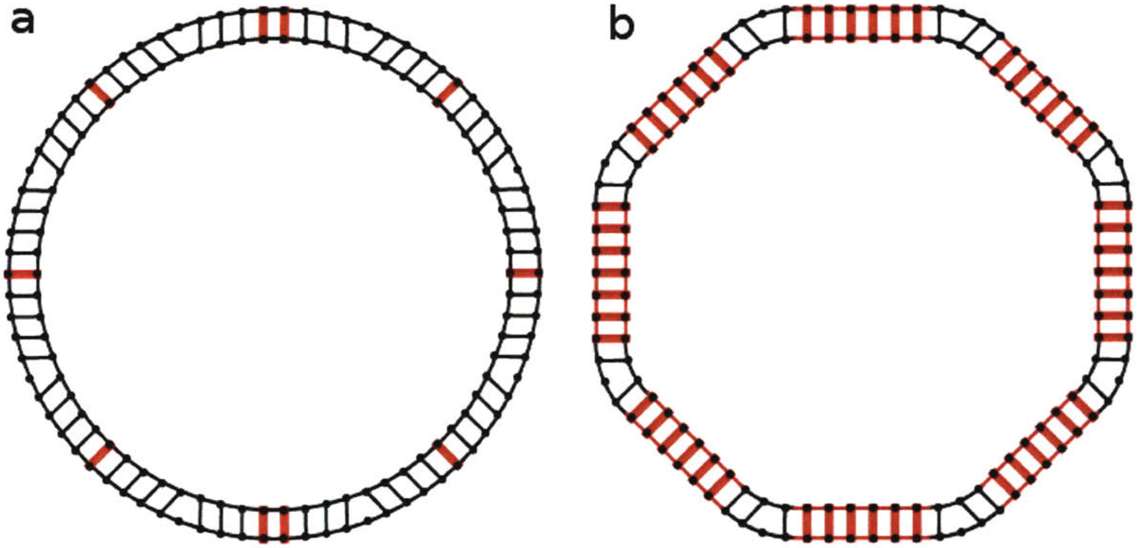

Figure 4.1: Nanotube with a (a) circular cross section and (b) polygonal cross section

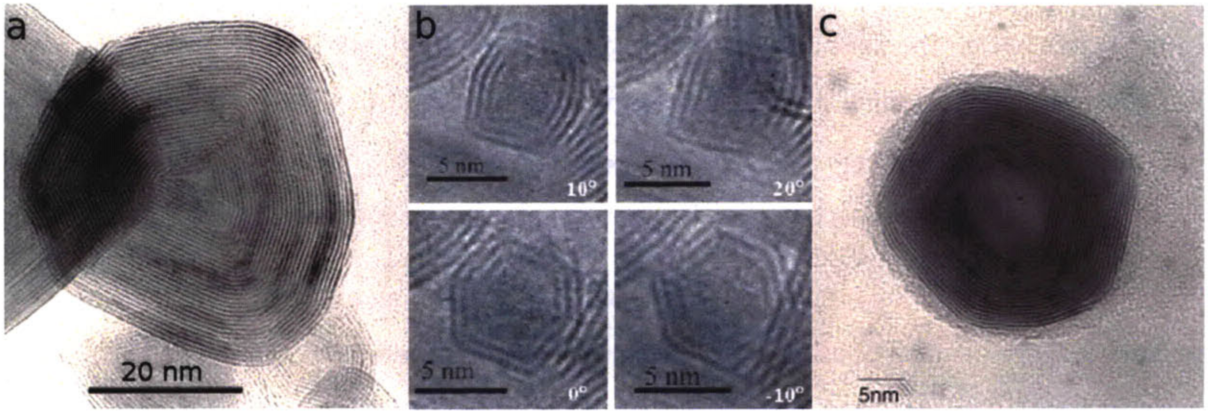

Figure 4.2: Faceted MoS_2 nanoparticle with (a) 50 nm diameter [3] and (b) 7 nm diameter [5] and (c) WS_2 nanoparticle with 30 nm diameter [2]

In this chapter I present a polygonal nanotube structure without defects. I show an energy component model that can be used to compare circular and polygonal nanotubes. I also discuss the effect of chirality on the structure of polygonal nanotubes. I have performed calculations in order to estimate the parameters in the energy component model for TiS_2 and

MoS_2 nanotubes. I will present the results of these calculations. I will end by discussing the key finding of this study and any implications this may have.

4.1 Energy components of nanotubes

Because the length of nanotubes is considerably larger than their diameter they can be considered infinite along the tube axis for the purpose of our calculations. This results in a unit cell consisting of the complete cross section of the nanotube with a length along the nanotube axis defined by some multiple of the periodic distance in this direction. For most inorganic nanotubes the minimum diameter seen experimentally is approximately 10 nm [35-36, 48, 172] and the minimum periodic distance along the nanotube axis is 3-3.5 Å. The periodic unit cell for a single-walled inorganic nanotube with a diameter of 10 nm and a length along the nanotube axis of 3.5 Å contains approximately 300 atoms. This is too large for extensive atomistic calculations.

An alternative to atomistic calculations is to divide the energy of a nanotube into a number of energy components and analyze the components separately. The energy of a nanotube, relative to the bulk material, can be divided into four components: strain energy, interfacial energy, defect energy and surface energy. The total energy of the nanotube can thus be written as,

$$E_{total} = N\varepsilon_{bulk} + E_{strain} + E_{interface} + E_{defect} + E_{surface} \qquad (4.1)$$

In this equation N is the number of atoms, ε_{bulk} is the bulk energy per atom, and all other energy terms represent the excess energy of the nanotube due to various components. In this chapter two possible structures for nanotubes are compared, a polygonal model in which the sides of the tube form polygonal faces, and a more cylindrical model in which the tube cross section is circular. The surface energy per unit area for each of these models will be approximately identical so this component is not important. Defect formation is an important energetic component that can affect the structure of a nanotube. Defects could lower the energy of polygonal nanotubes, increasing the likelihood of their formation; however their treatment lies outside of the scope of the work presented here. The two energy components discussed in detail in this chapter are strain energy and interfacial energy.

4.1.1 Strain Energy

4.1.1.1 Bending Strain Energy

The bending strain energy is the energy required to apply a given amount of curvature to a sheet of material. In linear elasticity the bending strain energy per atom, ε_{bend}, is inversely proportional to the square of the radius of curvature, r_c. The number of atoms, N, in a circular nanotube cross section with the periodic length is proportional to the radius of curvature (radius of the circle) so the total bending strain energy, E_{bend}, is inversely proportional to the radius. This can be shown mathematically as:

$$\varepsilon_{bend}(r) = \frac{C_{bend}}{r^2}$$

$$N(r) = 2\pi \times C_{length} \times r \tag{4.2}$$

$$E_{bend}(r) = N \times \varepsilon_{bend} = \frac{2\pi \times C_{length} C_{bend}}{r}$$

where C_{bend} is the bending strain energy constant and C_{length} is a factor to convert from length to number of atoms. These two constants, C_{bend} and C_{length}, are independent of the radius of curvature and depend only on the material.

4.1.1.2 Tensile Strain Energy

Tensile strain energy is the energy required to stretch or compress a sheet of material. Stretching or compressing of nanotube layers is often necessary in order to achieve a coherent interface between layers. Tensile strain is defined by the strain fraction, ε, which is the ratio of the change in length, Δl, to the initial length, l_0.

$$\varepsilon = \frac{\Delta l}{l_0} \qquad (4.3)$$

Tensile strain energy per unit volume is proportional to the square of the strain fraction, with the constant of proportionality equal to one half of the Young's Modulus.

$$E_{tensile} = N_\varepsilon \times U_0 \times \frac{E}{2}\varepsilon^2 \qquad (4.4)$$

In equation (4.4), N_ε is the number of atoms under tensile strain, U_0 is the volume per atom and E is Young's Modulus.

4.1.2 Interfacial Energy

The interfacial energy component corresponds to the energy of an incoherent interface relative to a coherent interface. The interface between two layers of a multi-walled nanotube cannot be coherent without the inclusion of tensile strain. This is due to the difference in the circumference of consecutive layers. In order for the interface to be coherent, the same number of unit cells has to be spread out over a length that increases with distance from the center of the nanotube. This is unlikely for multi-walled tubes due to the large amount of strain required. Figure 4.3 is a simple representation of two layers of TiS_2 where the blue dots represent Ti atoms (S atoms are not shown for ease of viewing). Figure 4.3(a) shows two flat layers, analogous to the bulk where Ti atoms in one layer project directly above Ti atoms in a preceding layer. No strain is required to maintain alignment throughout the layers. Figure 4.3(b) shows two of these layers bent independently of each other, with the radii of curvature of the two layers analogous to consecutive layers in a nanotube. In order for the interface to be coherent, the alignment lines should be perpendicular to the surface. While this is true in the center of Figure 4.3(b), for most of the nanotube the difference in length between the two layers results in an incoherent interface. Figure 4.3(c) shows two layers bent with the same curvature as in Figure 4.3(b), but the layers are strained so as to maintain the bulk alignment. In this figure the alignment lines are perpendicular to the surface. However, a large amount of tensile strain is required to achieve this alignment. The tensile strain energy required to maintain this alignment for multiple layers grows rapidly with the number of layers ($E_{tensile} \alpha n^3$).

The interfacial energy term in equation (4.1) is defined as the binding energy of a coherent interface minus the binding energy of an incoherent interface. This can be represented by an interfacial energy constant, γ_{int}, which gives the interfacial energy per unit of interfacial area.

$$E_{interface} = E_{incoherent} - E_{coherent} = N_{inc} \times A_0 \times \gamma_{int} \tag{4.5}$$

In this equation, N_{inc} is the number of atoms with an incoherent interface and A_0 is the interfacial area per atom.

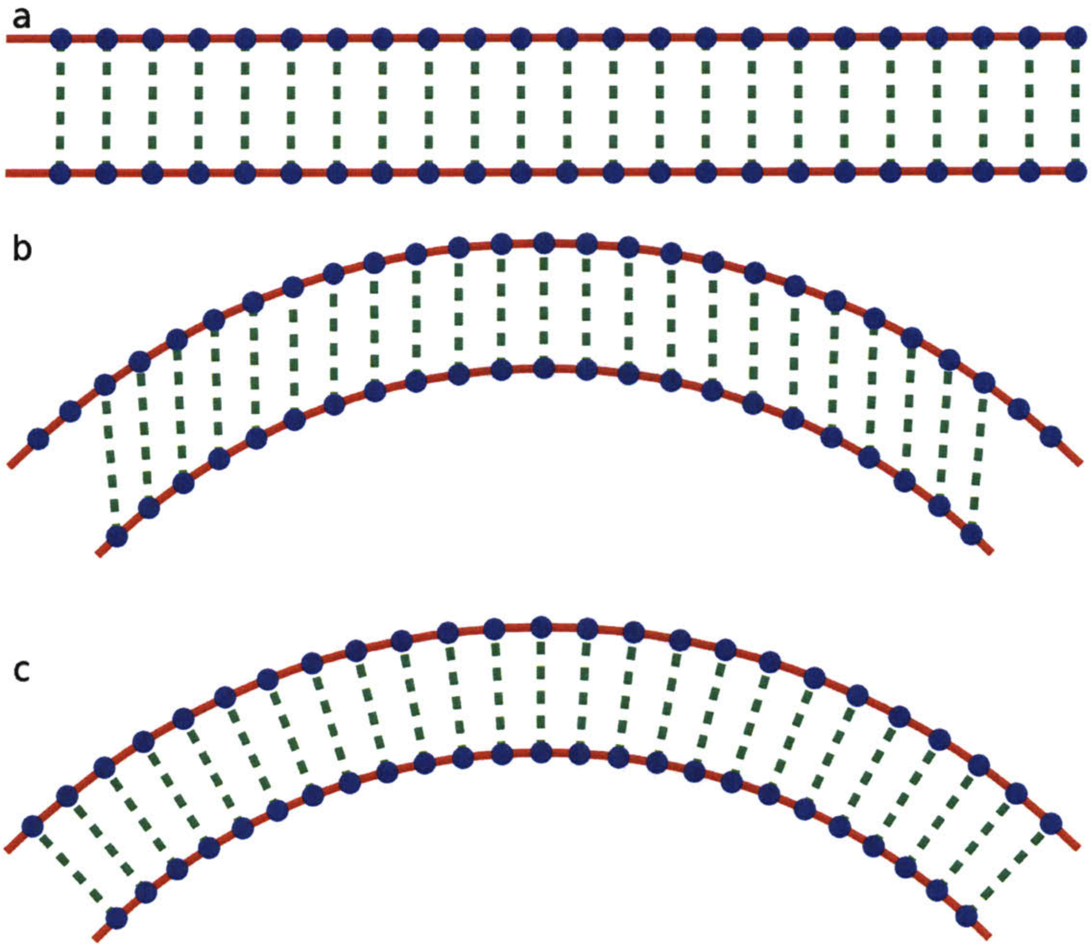

Figure 4.3: Alignment diagram. Bulk alignment (a) cannont be maintained when layers are curved without strain (b). If tensile and compressive strain is applied (c) bulk alignment can be maintained

4.2 Nanotube models: Polygonal versus circular cross-section

In the remainder of this chapter the energy of a normal cylindrical tube is compared with that of a polygonal tube. The polygonal model discussed in this paper consists of nanotubes where the cross section is a polygon with rounded corners. The bending strain energy is localized to the corners of the polygon, resulting in increased strain energy, but the flat sides of the polygon provide a coherent interface leading to a reduction in interfacial energy. When the interfacial energy is much larger than the bending strain energy the polygonal model can result in lower overall energy than that for a nanotube with a circular cross section. In this section we will first discuss the polygonal model in relation to single-walled nanotubes, and then we will expand this to multi-walled tubes and explain what determines the number of sides to the polygon.

4.2.1 Single Polygonal Tube

In an ideal polygon the corners are perfectly sharp, i.e. the radius of curvature of the corners is 0. This is not practical for a nanotube. The corners will have some finite radius of curvature, which will define the strain energy of the nanotube. To illustrate this point Figure 4.4(a) depicts a 6-sided polygon with the radius of curvature labeled. All of the strain energy is localized in these curved corners; the flat sections are free of strain. The total strain energy of a single polygonal tube depends only on this radius of curvature. To prove this point, consider an *N*-sided polygon. This polygon will have *N* corners, each with the same radius of curvature, r_c, and subtending an angle of $2\pi/N$. The length of the strained arc at each corner is thus $2\pi/N \times r_c$. Therefore, the total strain energy per unit cell for this tube will be

$$E_{bend} = N \times C_{length} \times 2\pi/N \times r_c \times C_{bend}/r_c^2 = \frac{2\pi C_{bend} C_{length}}{r_c} \tag{4.6}$$

The total strain energy is independent of the number of sides and only depends on the radius of curvature at the corners. Equation (4.6) is equivalent to equation (4.2) for bending strain energy with the radius of the tube replaced by the radius of curvature at the corners. For a single-walled nanotube there is no interfacial energy so the optimum structure is the one that minimizes the bending strain energy, which occurs for the maximum radius of curvature. For a given number of atoms on the circumference, the maximum radius of curvature results in a circle, Figure 4.4(b).

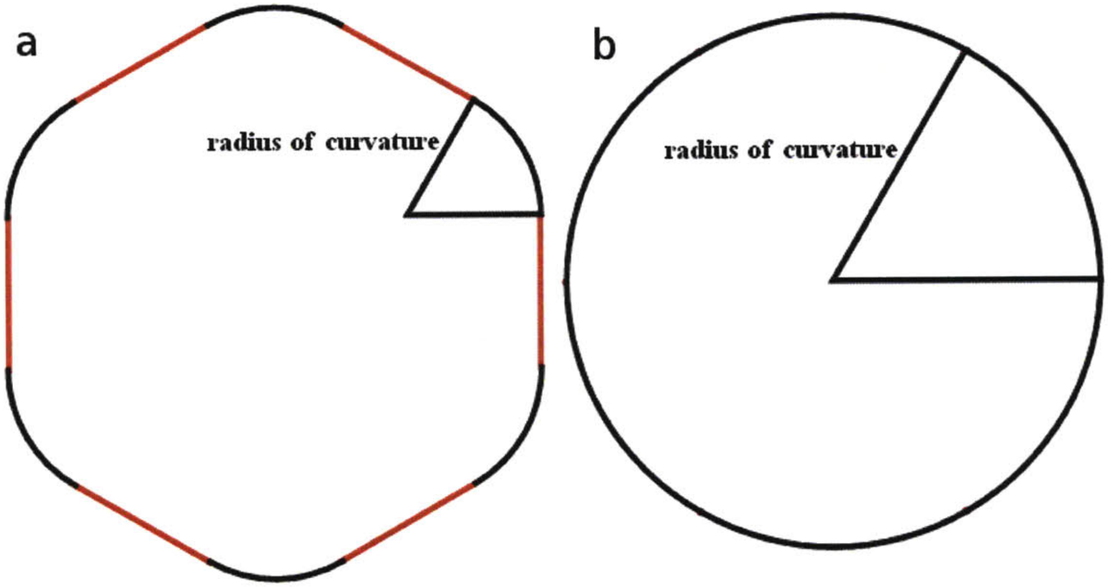

Figure 4.4: Bending strain in a single-walled polygonal nanotube (a) is localized to the corners where the radius of curvature is less than that of a cylindrical nanotube (b) with equal circumference

4.2.2 Multi-walled Tube

For a multi-walled nanotube the polygonal model provides lower interfacial energy than a circular nanotube as the flat sections of the tube can be coherent and without strain, although this occurs with an increase in strain energy due to the smaller radius of curvature in the corners. All of the incoherence and strain is localized in the corners of the polygon. Figure 4.5 shows two consecutive nanotube layers where the thick red lines represent a coherent interface. The outer layer has more length and thus more atoms than the inner layer. When the cross section is circular, as in figure 4.5(a), these excess atoms are spread evenly around the circumference of the tube, resulting in a mostly incoherent interface. When the cross section is a polygon (figure 4.5(b)) it is possible for the flat sections to have a coherent interface as all of the excess atoms are located in the corners of the polygon.

A nanotube with *n* layers will have *n-1* interfaces and its energy per unit cell can be obtained by adding the strain and interfacial energy:

$$E = n \times \frac{2\pi C_{bend} C_{length}}{r_c} + (n-1) \times 2\pi r_c \, l_{unit} \, \gamma_{int} \qquad (4.7)$$

where γ_{int} is the interfacial energy per unit area and l_{unit} is the length of the unit cell. To simplify the equation, we assumed that the radius of curvature remains constant from layer to layer, which may not be the case. This will be discussed in section 4.3.4. To determine the optimum radius of curvature we minimize equation (4.7) with respect to the radius of curvature. If this optimum radius of curvature, shown in equation (4.8), is smaller than the radius of the nanotube, then a polygonal cross section will be favored over a circular cross section.

$$\frac{\partial E}{\partial r_c} = (n-1) \times 2\pi l_{unit} \gamma_{int} - n \times \frac{2\pi C_{bend} C_{length}}{r_c^2} = 0$$

$$r_c = \sqrt{\frac{n}{n-1} \times \frac{C_{bend} C_{length}}{l_{unit} \gamma_{int}}} \qquad (4.8)$$

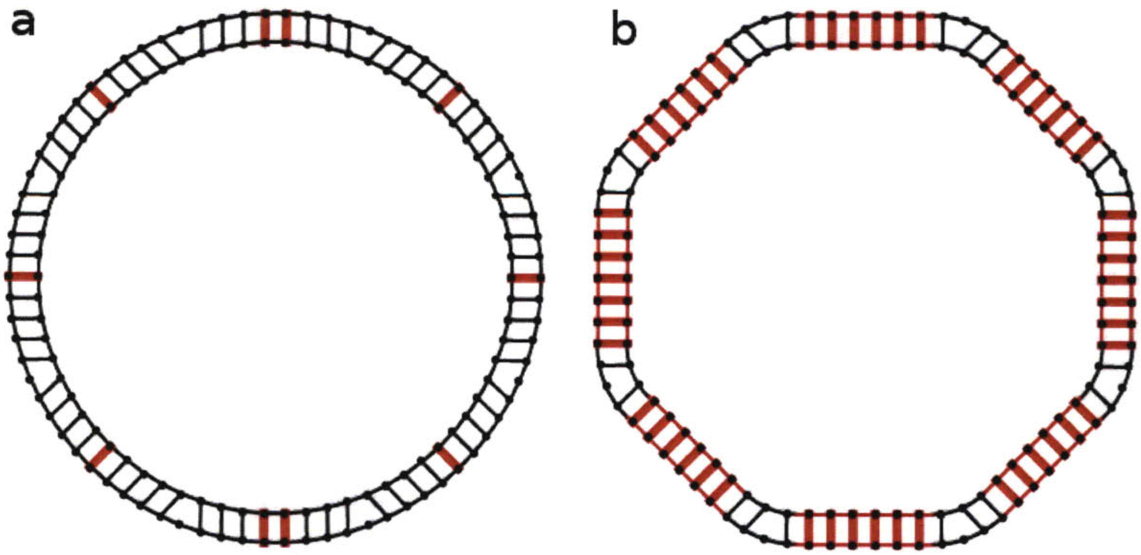

Figure 4.5: Multi-walled (a) cylindrical nanotubes have less coherent interface than (b) polygonal nanotubes. Thick Red lines represent coherent interface while black lines represent incoherent interface.

4.2.3 Effect of Chirality on Polygonal Structure

The polygonal model can only be energetically favored if there is a coherent interface between the flat sections of the polygon. This means that a coherent interface is attained on either side of each rounded corner. For this to occur, the difference in the length for two consecutive layers to go around one corner must be equal to an integer number of lattice vectors in the rolling direction. Figure 4.6 is a diagram of two consecutive layers to illustrate how the two layers must be coherent at the end of the curved segment. The outer layer has additional length equal to 2*Δl*, determined by the interlayer spacing, *d*, and the angle of the corner, *β*:

$$\Delta l = d \times Tan\left(\frac{\beta}{2}\right) = d \times Tan\left(\frac{\pi}{N}\right) \qquad (4.9)$$

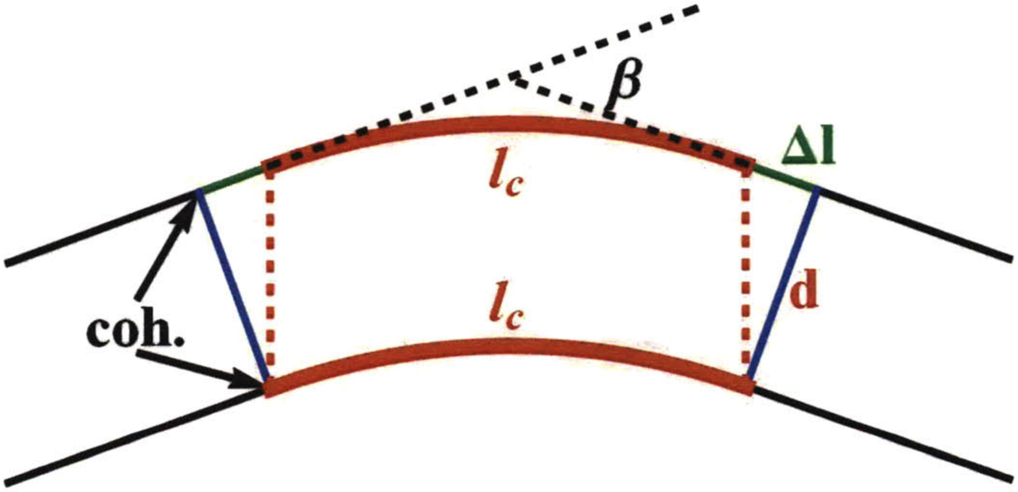

Figure 4.6: Two layers of a polygonal nanotube, representing the length difference between layers, *Δl,* the curved length, l_c, and the bending angle, *β*

In order for the layers to have a coherent interface at the points indicated, this excess length must equal an integer number of lattice vectors in the rolling direction. The lattice vector in the rolling direction is determined by the chirality of the nanotube. To illustrate this, figure 4.7

shows the top view of a TiS_2 sheet. The rolling direction indicated in the figure is that for a zigzag (n,0) nanotube. The vector, *a*, is the lattice vector in the rolling direction.

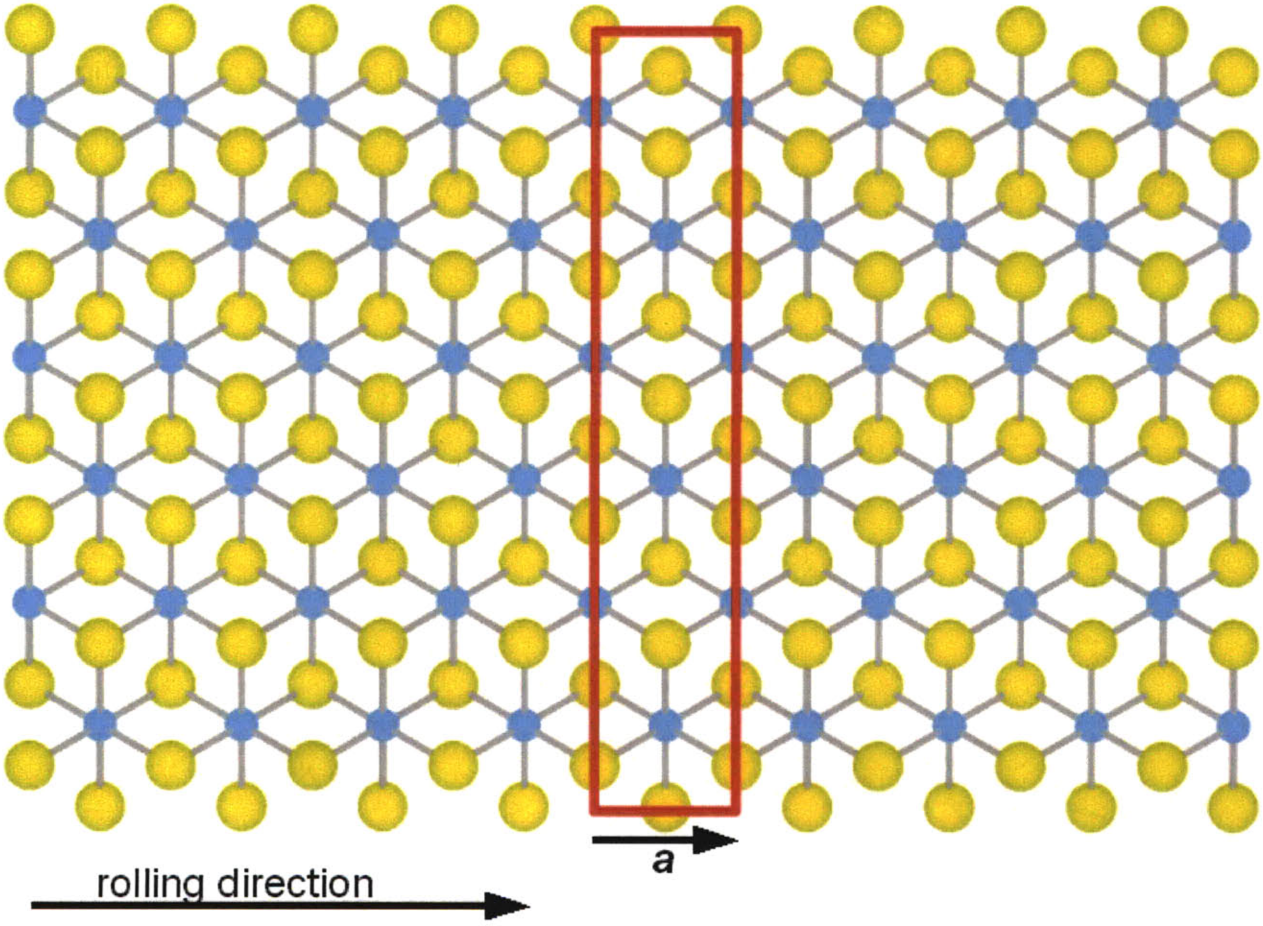

Figure 4.7: Top view of TiS_2 sheet showing the lattice vector in the rolling direction

This chirality dependence is the main restriction of the polygon model. There are only a few chiralities for which this requirement can be met. For example, in TiS_2, the interlayer spacing, *d*, is equal to 5.7 Å. The total difference in length between consecutive layers is $2\pi d = 35.8\ \AA$. This length difference is divided evenly among the corners in the polygon model. As a result, there are only four chiralities (along with symmetric equivalents) that have a lattice vector small enough for the polygon model to apply. However, the symmetric equivalents constitute 38% of all possible nanotube chiralities. Table 4.1 lists the four chiralities. The first column, *a*, is the length of the lattice vector in the rolling direction, as shown in figure 4.7. Chirality is the *x,y* vector defining the rolling direction. The third column, β_{opt}, is the optimum bending angle for that lattice vector. The bending angle is illustrated in figure 4.6. *N* is the number of sides on a polygon with a bending angle that comes closest to β_{opt}. Next is the actual bending angle, β, corresponding to a polygon with *N* sides. The last column is the strain, ε, resulting from the difference between the lattice vector, *a*, and the excess length for the actual bending angle. The strain is this difference divided by the length of the curved segment, calculated for a radius of curvature of 14.7 Å, which is the optimum radius of curvature for TiS_2 polygonal nanotubes as will be shown in section 4.5.1. The resulting strain energy can be large for some chiralities. The effect of this tensile strain on the total energy of a polygonal nanotube will be discussed in the section 4.5.2. For all chiralities that are not a symmetric equivalent of one of the chiralities shown in Table 4.1 the polygon model will not apply, unless defects are included to provide the appropriate difference in length between layers. It is possible that the difference in length between successive layers going around the corner is not a full lattice vector but instead results in a stacking fault in the flat section of the tube.

a	**chirality**	β_{opt}	**N**	β	**E**
3.460	1,0	34.780	10	36	-0.95%
5.993	2,1	60.240	6	60	0.11%
9.154	3,1	92.018	4	90	0.63%
12.475	4,1	125.399	3	120	1.26%

Table 4.1: Allowed chiralities in the polygonal model as applied to TiS_2 nanotubes. For each chirality the Table shows the length of the vector, maximum number of sides, angle of each corner and strain required at the corners of the polygon.

4.2.4 Layer Spacing at Corners of Polygon:

Equation (4.7) is a simplified energy model for polygonal nanotubes. A major approximation regarding spacing between layers was made in deriving this energy model in order to avoid confusion and provide an analytical equation to approximate the optimum radius of curvature. In this section this approximation is discussed as well as how it affects the energy model.

The previous discussion and equations have assumed that the radius of curvature is the same for every layer of the polygonal nanotube. This is not necessarily the case. Some complications arise when consecutive layers have the same radius of curvature. The main complication is that the interlayer spacing cannot be the same throughout the corner. The magnitude of the change in interlayer spacing depends on the bending angle. In order to clarify this, consider the two extreme cases as to how the radius of curvature can change for multiple layers: the radius of curvature is constant for every layer or the radius of curvature increases by the interlayer spacing every layer. Figure 4.8 illustrates these extremes. Figure 4.8(a) shows two layers where the radius of curvature is the same for each layer. In this case the interlayer spacing is larger at the corners than for the rest of the nanotube. The ratio of d_2 to d is

$^1/_{\cos(\frac{\beta}{2})}$. For β = 60° this corresponds to a difference in interlayer spacing of 15%. Figure 4.8(b) shows the other extreme, two layers where the radius of curvature changes by the interlayer spacing from one layer to the next. In this case the spacing is the same at the corners as it is in the rest of the nanotube. However, when the radius of curvature increases, the curved length also increases. As a result the amount of incoherent interface increases with the radius of curvature.

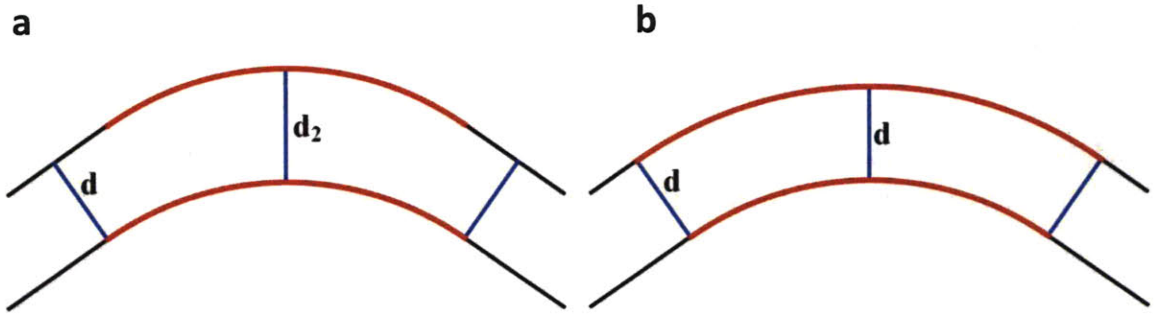

Figure 4.8: Two cases of how the radius of curvature changes for multiple nanotube layers. In (a) the radius of curvature remains constant, in (b) the radius of curvature increases by the interlayer spacing, *d*.

Equations 4.7 and 4.8 are derived under the assumption that the radius of curvature is constant, but these equations do not account for a change in interfacial energy due to a change in the interlayer spacing. One can revise equation (4.7) to represent a polygonal nanotube with a different radius of curvature in each layer and a constant interlayer spacing:

$$E_{polygon} = 2\pi C_{length} \sum_{i=0}^{n-1} \frac{C_{bend}}{r_c + i*d} + 2\pi\gamma_{int}\left[\left(r_c + {}^{d}/_{2}\right) * (n-1) + d*(n-2)\right] \quad (4.10)$$

The variable r_c is the radius of curvature of the innermost layer. There is no general minimum energy solution to equation (4.10), but for a given value of n the minimum energy radius of curvature can be determined. This will be shown in section 4.5.

4.3 Results

Atomistic calculations were performed on TiS_2 and MoS_2 in order to estimate the parameters of the nanotube energy model presented in this chapter. In this section the results of these calculations are reported. Calculations details are discussed in chapter 3.

4.3.1 TiS₂

4.3.1.1 Bending Strain Energy

The curved surface method that was explained in chapter 3 was used to determine the bending strain energy constant for a triple layer of TiS_2. Calculations were performed on structures with various bending angles and curved lengths. Figure 4.6 shows the bending angle, β, and the curved length, l_c. These two parameters define the radius of curvature, $r_c = {}^{\beta}/_{l_c}$.

The bending strain energy per formula unit is given by ${}^{C_{bend}}/_{r_c{}^2}$. The only unknown parameter in the equation for the bending strain energy (eqn. 4.6) is the constant, C_{bend}.

In order to determine the bending strain energy constant we calculated the strain energy for structures with bending angles of 10, 20, 30, 40 and 60°. For each of these angles we performed calculations on structures with curved lengths of 10 and 20 Å. Figure 4.9 shows a TiS_2 curved surface with a bending angle of 60° and a curved length of 10 Å. The results of these calculations are shown in figure 4.10. The points are the actual calculated strain energy, while equation (4.6) is plotted with a bending strain energy constant of 4.033 eV $Å^2$ per atom for the two different curved lengths. The data points agree with the fit line with an RMS deviation of 4.1 meV.

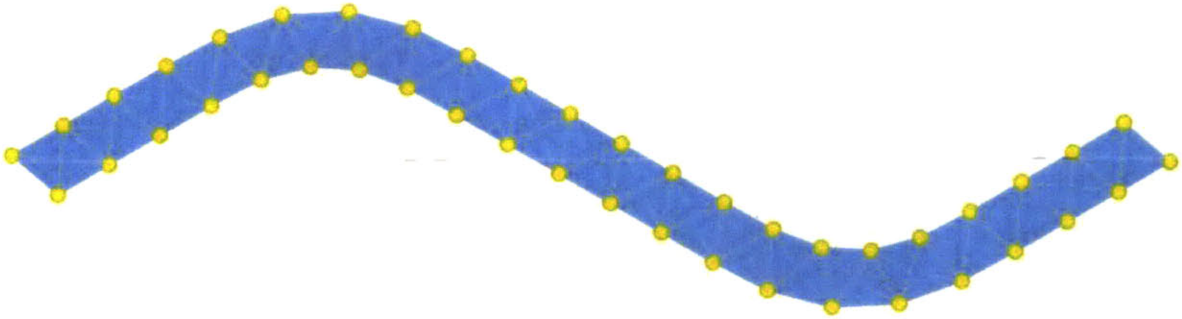

Figure 4.9: TiS_2 curved surface with a bending angle of 60° and a curved length of 10Å

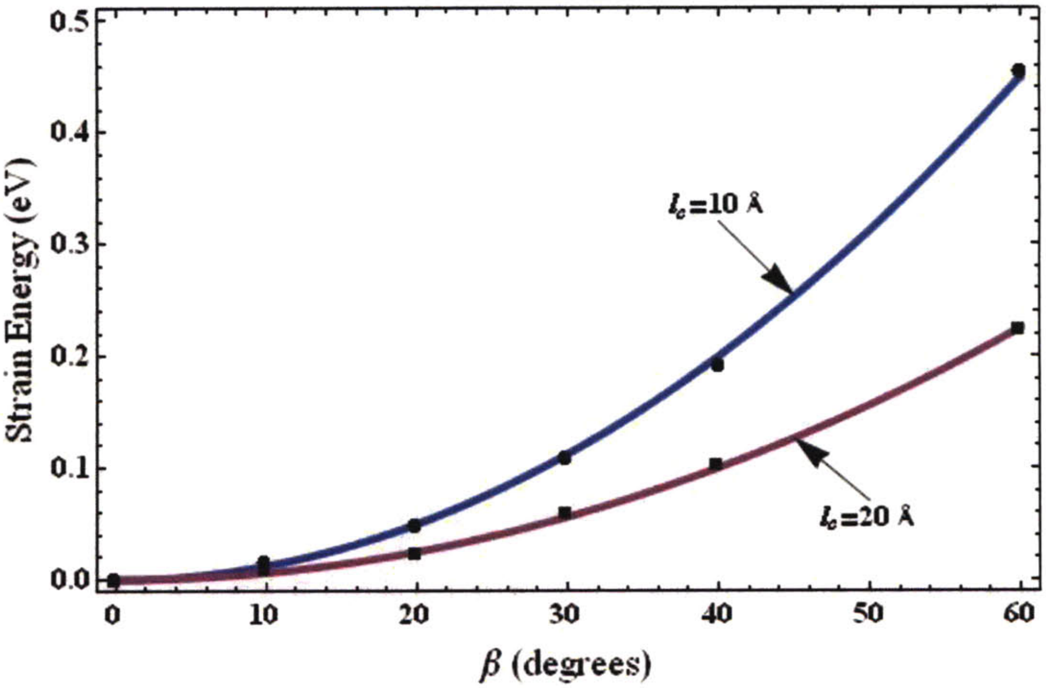

Figure 4.10: Strain energy versus bend angle for TiS_2 sheets with curved lengths of 10 and 20 Å

4.3.1.2 Interfacial Energy

In layered structures like TiS_2, the layers are held together by Van der Waals forces, which are not captured with DFT. However, when the stacking is disordered the distance between S atoms in consecutive layers is considerably less than the distance between S atoms in the same layer. The effect of this decrease in bond length, which is captured well with DFT, is a large contributor to the interfacial energy in this material due to the ionicity of the S-S interaction [12]. The interfacial energy will change with a change in interlayer spacing, but this was not investigated in this work, because it would be more strongly affected by Van der Waals forces and thus not accurately captured with DFT.

Double layer curved surface were used to determine the interfacial energy for incoherent interfaces. These structures consist of two TiS_2 triple layers separated by 5.7 Å, the experimentally measured interlayer spacing in both bulk TiS_2 and TiS_2 nanotubes [35]. The length of the curved portion of these surfaces was varied in order to vary the amount of incoherent interface. Figure 4.11 shows one of these double layers with a curved length of 5 Å. Calculations were also performed on two flat TiS_2 triple layers separated by 5.7 Å to determine the energy of a completely coherent interface. The difference between the energy of two single layers and that of a double layer is the interfacial energy. The interfacial energy for the structure with a completely coherent interface is subtracted from the interfacial energy for the structures with some incoherent interface to give the excess energy due to an incoherent interface. Figure 4.12 shows the excess energy plotted versus the amount of incoherent interface. The line fitted to the data corresponds to an interfacial energy constant of 19.16 meV per atom, resulting in an RMS deviation of 10.9 meV. This is the energy of an incoherent interface relative to a coherent interface. Structures with a different incoherence length also have a different radius of curvature and thus the structure on the interface is slightly different. The good agreement of the data points with the line indicate that the interfacial energy at the corners of the polygon can be well approximated by a single interfacial energy constant.

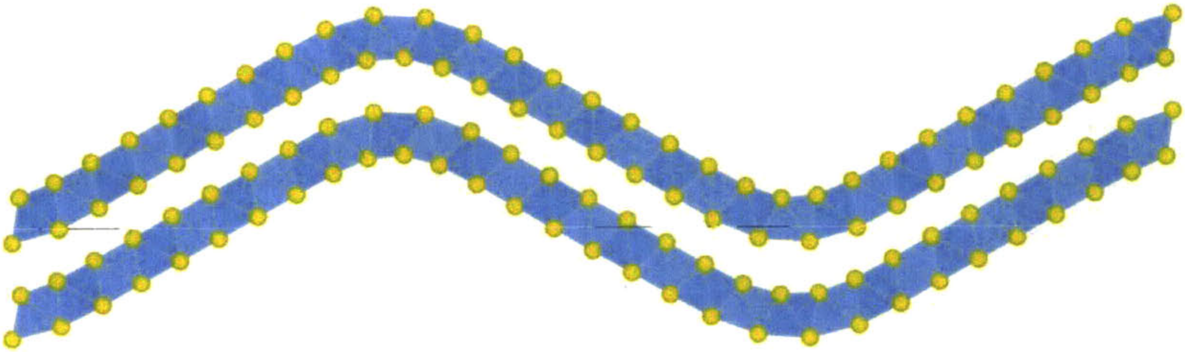

Figure 4.11: Double layer TiS_2 curved surface with a cuved length of 5 Å

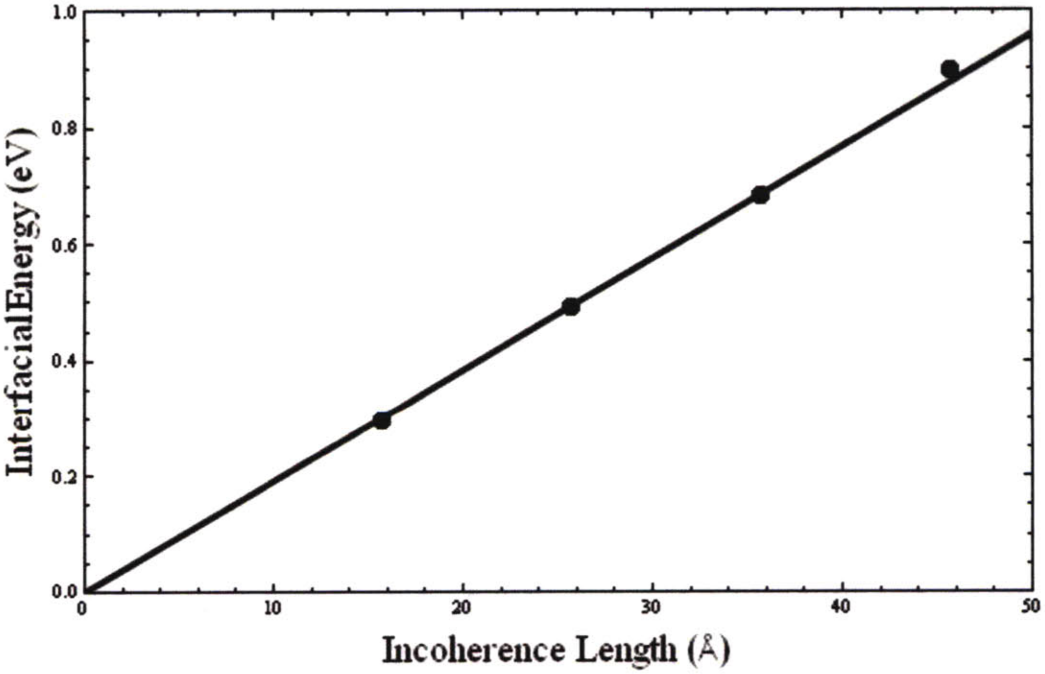

Figure 4.12: Calculated Interfacial energy versus incoherence length for TiS_2 sheets

4.3.1.3 Tensile Strain Energy

The energy required to compress or expand a nanotube layer was not included in the previous equations, but it is a relevant factor in the overall energy of the polygonal model. Due to Hooke's law this energy varies with the square of the strain fraction, ε. To determine the tensile strain energy constant, calculations on bulk TiS_2 with varying levels of compression and expansion of one of the in-plane lattice constants were performed. The expected form of the results of these calculations was shown in equation (4.3). The results of these calculations are shown in figure 4.13. The data is fitted to equation (4.3) with a Young's modulus of 36.2 GPa, corresponding to a tensile strain energy constant, $C_{tensile}$, of 8.9 eV per atom. The resulting RMS deviation is 8.3 meV.

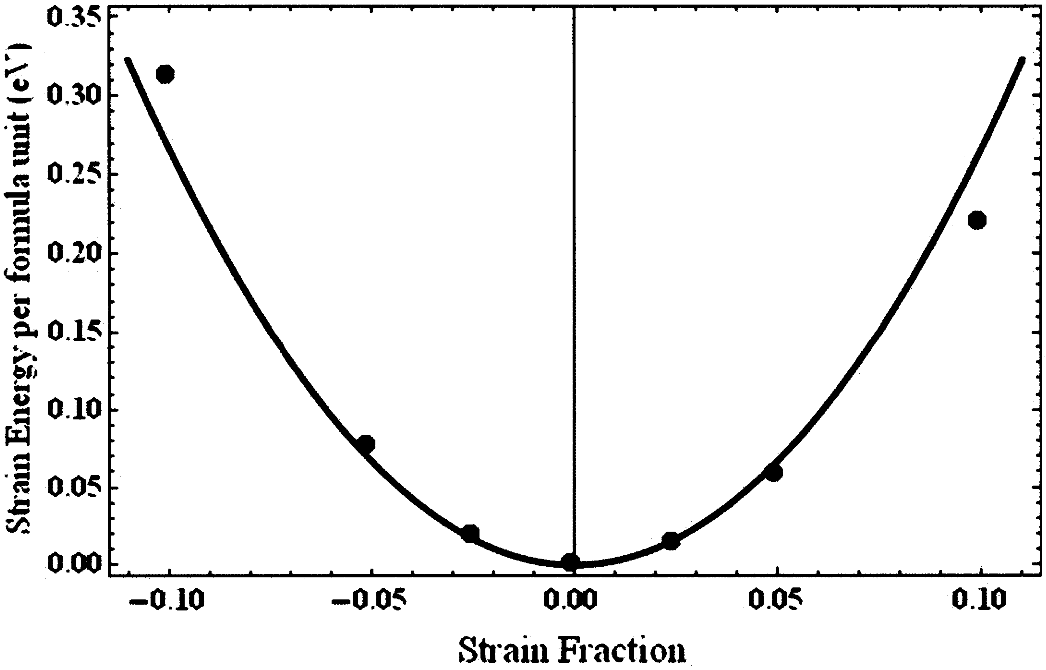

Figure 4.13: Tensile strain energy of TiS_2 plotted versus strain fraction

4.3.2 MoS2

4.3.2.1 Bending Strain Energy

As with TiS_2, we calculated the strain energy for MoS_2 structures with bending angles of 10, 20, 30, 40 and 60° and curved lengths of 10 and 20 Å. The results of these calculations are shown in figure 4.14. The points are the actual calculated strain energy, while equation (4.6) is plotted with a bending strain energy constant of 11.7 eV $Å^2$ per atom for the two different curved lengths. The data points agree with the fit line with an RMS deviation of 18 meV.

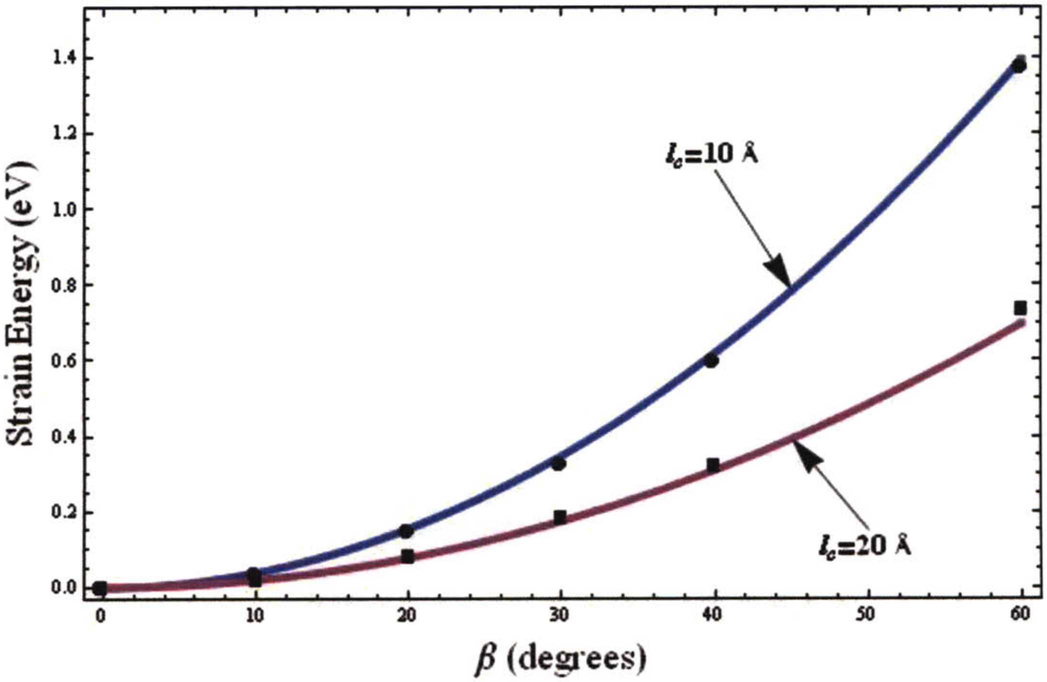

Figure 4.14: Strain energy versus bend angle for TiS_2 sheets with curved lengths of 10 and 20 Å

4.3.2.2 Interfacial Energy

Double layer curved surfaces with varying amounts of incoherent interface were also created for MoS_2 to analyze the interfacial energy. Figure 4.15 shows the excess energy plotted versus the amount of incoherent interface. A single line does not fit the data, because the incoherence energy is low for small radii of curvature as will be discussed in the next section. A single line does fit the last three points well, with an RMS of 17 meV. Table 4.2 shows the incoherence energy per atom for each of the four points in figure 4.15. While the incoherence energy per atom increases with the incoherence length, for 3 out of the 4 lengths the interfacial energy per atom is within 1.5 meV of 9.92 meV per atom.

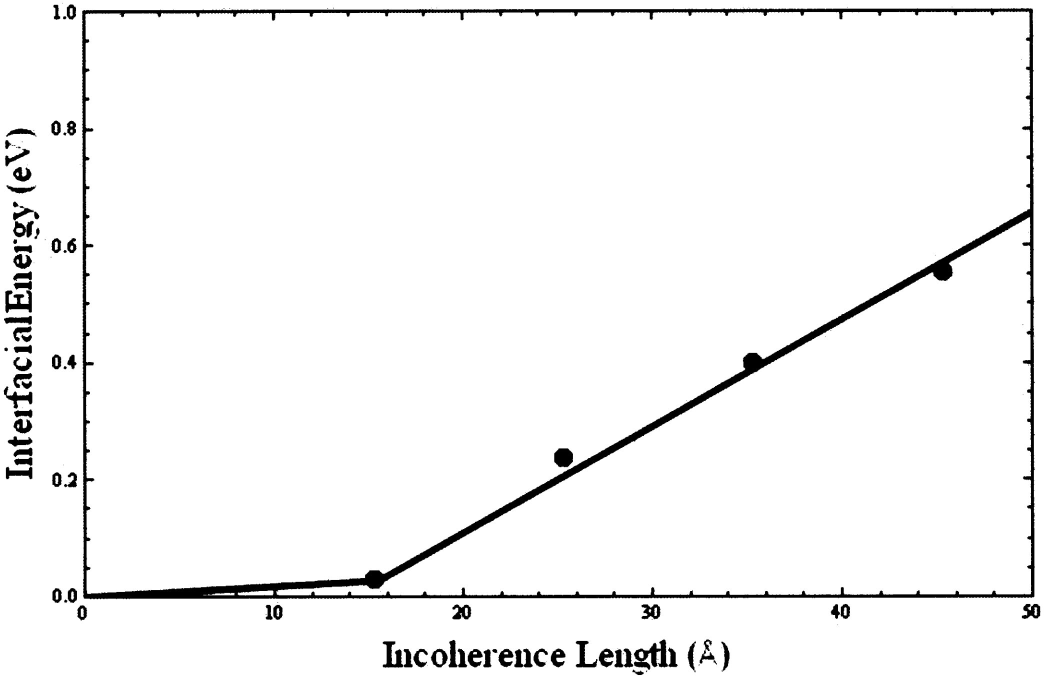

Figure 4.15: Calculated Interfacial energy versus incoherence length for MoS_2 sheets

Incoherence Length	Incoherence Energy per atom
15.529 Å	1.6 meV
25.529 Å	8.48 meV
35.529 Å	10.24 meV
45.529 Å	11.15 meV

Table 4.2: Incoherence energy per atom increases with incoherence length for MoS_2 sheets

4.4 Discussion

4.4.1 Incoherence Energy for MoS_2

The interfacial energy calculations for MoS_2 showed an increase in incoherence energy per atom with an increase in incoherence length, which was shown in table 4.2. This also occurred for TiS_2, but the increase was not nearly as dramatic. This is likely due to the larger strain energy for MoS_2 compared to TiS_2. The incoherence length is directly proportional to the radius of curvature of the layers. At small radii of curvature, a shift in the position of sulfur atoms in one layer results in a larger change in the coordination between sulfur atoms in consecutive layers when compared to a larger radius of curvature. Because the strain energy of MoS_2 is considerably larger than for TiS_2, this effect is much more pronounced in MoS_2. At the smallest incoherence length of 15.529 Å the radius of curvature is approximately 5 Å. This is much smaller than the radius of curvature that would occur in polygonal nanotubes, as will be shown in the next section. Figure 4.16 shows the interface for the MoS_2 curved surface with the smallest incoherence length. Because the incoherent interface is small, the 2 sulfur atoms from the inner layer that are part of the interface can essentially relax to a coherent interface. For the other three incoherence lengths, the incoherence energy is well approximated with a constant of 9.92 meV per atom.

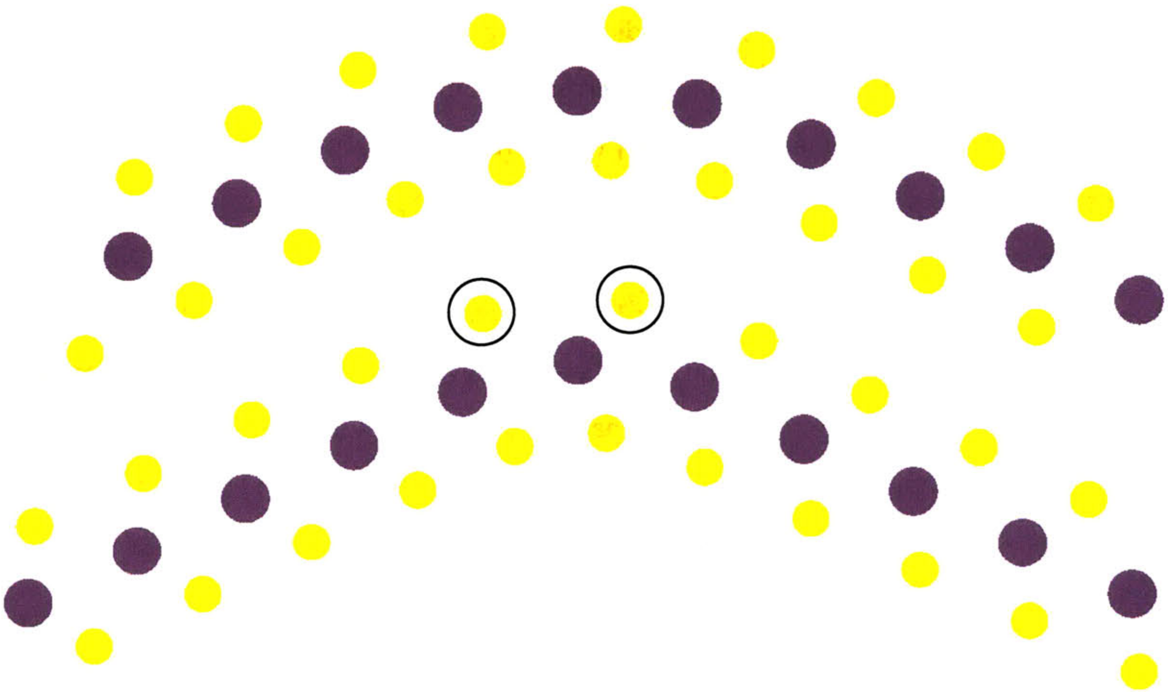

Figure 4.16: MoS_2 interface with smallest incoherence length. The radius of curvature of the inner layer is 5 Å. The two sulfur atoms from the inner layer that are part of the incoherent interface (circled in figure) are able to relax to a nearly coherent interface.

4.4.1 Radius of Curvature

In the previous section we showed results that can be used to estimate the interfacial energy constant and the bending strain energy constant of TiS_2 and MoS_2 and determine the nanotube shape with the lowest energy. Based on these results the low energy radius of curvature for a polygonal nanotube can be calculated. Equation (4.8), repeated here, gives the optimum radius of curvature for a given number of layers, *n*.

$$r_c = \sqrt{\frac{n}{n-1} \times \frac{C_{bend}\, C_{length}}{l_{unit}\, \gamma_{int}}} \qquad (4.11)$$

Table 4.3 lists the two energy constants and the optimum radius of curvature for several values of the number of layers, *n*.

Based upon our model, when the radius of curvature at the corners of a polygonal nanotube is equal to the nanotube radius the cross section will be circular, because the entire circumference of the nanotube is taken up by the curved corners. For example, table 4.3 shows that the optimum r_c is 20.79 Å when there are 2 layers in a TiS_2 nanotube, so when this nanotube exhibits a 2.079 nm radius both morphologies are identical in our model. More importantly, when the radius of the bi-layer TiS_2 is less than 2.079 nm the circular cross-section is more favorable while >2.079 nm radii should yield a polygonal cross-section. To generalize, multi-walled nanotubes exhibiting a radius smaller than the optimum radius of curvature (for a particular *n* value) should display circular cross-sections while nanotubes of radii greater than the optimum r_c should form a polygonal cross-section to yield a lower overall energy by creating straight segments.

	TiS_2	**MoS_2**
Bending strain energy constant, C_{bend}	4.033 eV*Å^2	11.7 eV*Å^2
Interfacial energy constant, γ_{int}	18.67 meV	9.92 meV
n= 2	r_c= 20.79Å	r_c= 48.58Å
n = 4	r_c = 16.97 Å	r_c= 39.67Å
n = 6	r_c = 16.10 Å	r_c= 37.63Å
n = 8	r_c = 15.71 Å	r_c= 36.72Å
n = 10	r_c = 15.49 Å	r_c= 36.21Å
$n = \infty$	r_c = 14.70 Å	r_c= 34.35Å

Table 4.3: Optimum radius of curvature, r_c, of the innermost nanotube layer decreases with the number of layers, n.

The results shown in table 4.3 represent the case where the radius of curvature remains constant from layer to layer, as discussed in section 4.3.4. In the alternate case the radius of curvature increases by the interlayer spacing for every layer. The energy of a polygonal nanotube under this condition was shown in equation (4.10) and is repeated here.

$$E_{polygon} = 2\pi C_{length} \sum_{i=0}^{n-1} \frac{C_{bend}}{r_c + i*d} + 2\pi\gamma_{int}\left[\left(r_c + {}^{d}\!/_{2}\right) * (n-1) + d * (n-2)\right] \quad (4.12)$$

In this equation r_c represents the radius of curvature of the innermost layer. For a given value of n, the value of r_c resulting in the minimum energy can be determined. Table 4.4 shows this optimum value of r_c for several values of n.

Equation (4.10) does not change the main conclusion of this paper, above a critical radius, polygonal nanotubes have lower energy than circular nanotubes. In fact, table 4.4 shows that the critical radius is lower in this case than for the original model. If the optimum radius of curvature is smaller than the radius of the innermost nanotube layer, and the chirality of the nanotube is symmetrically equivalent to one of those shown in Table 4.1, then the polygonal model will be the low energy solution. Most inorganic nanotubes have approximately 10 layers and an inner radius of 50 Å [35, 37, 172]. This is well above the optimum radius of curvature shown in either Table 4.3 or Table 4.4, except for a 2 layer MoS_2 nanotube, and hence it should be favorable for them to form polygons.

Number of layers	**Optimum radius of curvature**	
	TiS_2	**MoS_2**
2	18.4 Å	45.8 Å
4	11.5 Å	32.2 Å
6	8.8 Å	26.4 Å
8	7.2 Å	22.5 Å
10	6.2 Å	19.6 Å

Table 4.4: Optimum radius of curvature for several values of the number of layers, *n*, for the case where the radius of curvature changes from one layer to the next.

4.4.2 Tensile Strain in Polygonal Nanotubes

Because the length of the periodic unit cell, which accounts for the difference in length between two consecutive corners, will rarely be equal to $2\Delta l$ from equation (4.9) there will be some tensile or compressive strain. Table 4.1 shows all of the chiralities of TiS_2 nanotubes for which the polygonal model applies and the fractional strain for each chirality. The strain fractions shown in Table 4.1 are calculated by dividing the difference between the unit cell length, *a*, and $2\Delta l$ by the length of the arc at the corner:

$$\varepsilon = \frac{a-\beta\times d}{\beta\times r_c} \tag{4.13}$$

The value of r_c used is the value shown in Table 4.2 for an infinite number of layers, 14.7 Å. The value of ε will decrease for larger radii of curvature and increase for smaller radii of curvature. The value of ε will also increase with multiple layers. The values shown in Table 4.1 apply to the second layer. For the third layer the strain will be twice as large, three times as large for the fourth layer, etc. This is essentially because the third layer will have two more periodic units than the first layer, so the numerator of equation (4.13) will be twice as large, while the denominator will not change considerably. This strain must be considered. To quantify the magnitude of this strain we calculated the total tensile strain for a ten-layer nanotube with a chirality of (2,1), where the radius of curvature of consecutive layers increases by the interlayer spacing, as shown in figure 4.6(b). Equation (4.14) summarizes these calculations.

$$r_{ci} = r_{c0} + d \times (i-1) \qquad [i = 1,2,3 \ldots 10]$$

$$\varepsilon_i = \frac{(a-\beta\times d)\times(i-1)}{\beta\times r_{ci}} \tag{4.14}$$

$$\Delta E_i = 2\pi \times r_{ci} \times C_{length} \times C_{strain} \times \varepsilon_i^2$$

The calculated tensile strain for the entire ten-layer nanotube is 183 meV, corresponding to 0.1 meV per strained atom. This is a negligible amount of strain energy, but this calculation is for the chirality with the smallest strain fraction. For a similar ten-layer nanotube with a chirality of (4,1), which has the largest strain fraction of all chiralities shown in Table 4.1, the calculated tensile strain energy is 23.25 eV or 11.3 meV per strained atom. This is a considerable amount of strain energy and could prevent polygonal nanotube formation.

4.4.3 Polygon Cross Section

Thus far polygonal nanotubes have been depicted as having a cross section that is a regular polygon, but this is not a requirement. Because all strain and interfacial energy is located in the corners, the length and location of the flat segments have no effect on the energy. Figure 4.17 illustrates this point. This figure shows two possible nanotube cross sections. In each case the curved length and radius of curvature of each corner are identical. The total length of the flat sections in each case is also identical. As a result each nanotube would have the same energy. This point is reinforced by reference [125]. This paper shows two CdI_2 nanoparticles. Images of one of these nanoparticles is shown in figure 4.18. The cross section of each nanoparticle is a hexagon, but the two hexagons are vastly different and neither one is a regular polygon. Due to this equivalence of structures, polygonal nanotubes can be distorted with no change in energy. There would be some force required to shift the position of the corners, but the initial and final structures will have the same energy. This only applies to open-ended nanotubes. The ends of closed-ended nanotubes would likely provide resistance to deformation.

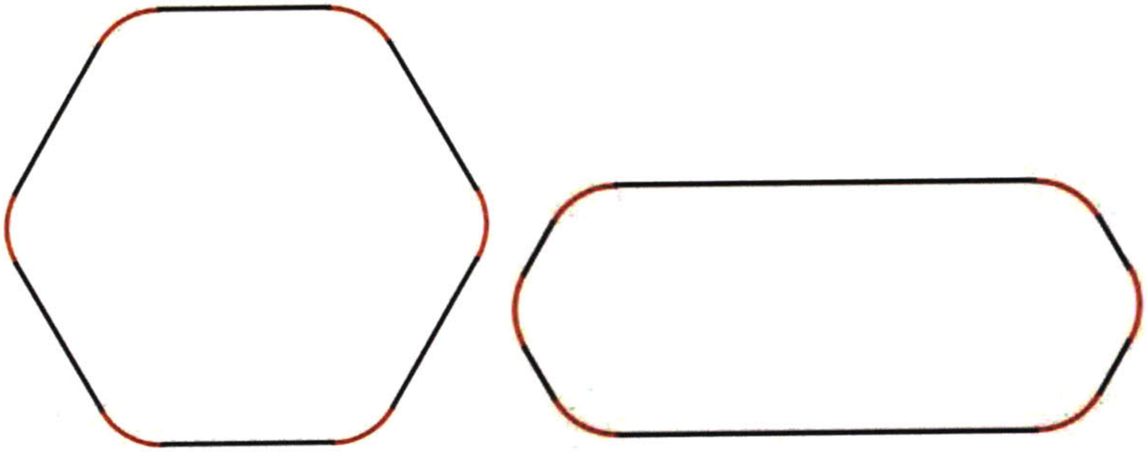

Figure 4.17: Cross section of two possible polygonal nanotubes that have the same energy in the polygonal model presented here

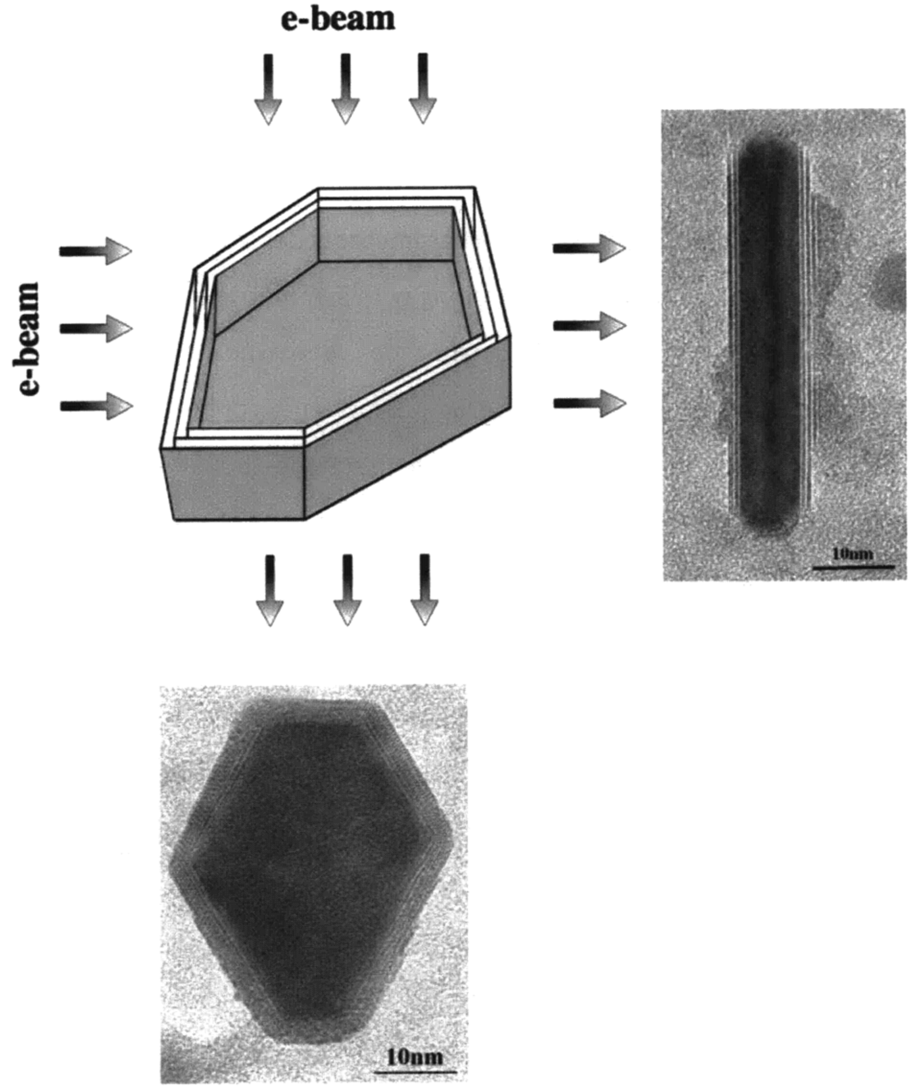

Figure 4.18: CdI_2 nanoparticle with polygonal sides [125]

4.5 Conclusions:

We have shown here that a multi-walled nanotube with a polygonal cross section can have a lower energy than a nanotube with a circular cross section. The polygonal cross section results in higher strain energy because the bending radius is smaller, but this can be more than compensated for by reduced interfacial energy. This energy reduction occurs because the flat sections of the nanotube can have a coherent interface with no tensile strain. A coherent interface has much lower energy than an incoherent interface. When the cross section is circular it is not possible to maintain a coherent interface without an excessive amount of tensile strain.

In order to maintain a coherent interface in the flat sections of a polygonal nanotube the difference in length between two layers must be equal to an integer number of lattice parameters in the rolling direction. This lattice parameter is determined by the chirality of the nanotube and only a few nanotube chiraities, along with symmetric equivalents, can therefore easily form polygons. The radius of inorganic nanotubes seen experimentally is considerably above the minimum radius required for the polygonal model to apply, so inorganic nanotubes with the required chiralities may form polygonal cross sections, though they do not need to be regular polygons. The energy is determined strictly by the radius of curvature of the corners of the polygon. This would result in extremely low resistance to deformation of polygonal nanotubes.

The optimum radius of curvature for polygonal TiS_2 nanotubes is considerably less than that for MoS_2 nanotubes due to a larger strain energy and smaller interfacial energy for MoS_2. This indicates that chemistry, and possibly structure, can have a large influence on the likelihood of polygonal nanotube formation. Investigations similar to the one presented here for other materials should provide useful information. The model predictions made here should also inspire further experimental investigations into the shape of multi-walled nanotubes.

Chapter 5

Lithium Storage in Inorganic Nanotubes

5.0 Introduction

The field of energy conversion and storage has received a tremendous amount of interest recently due to the search for replacements for fossil fuels. Li-ion batteries can be an important component of this search with some large improvements to Li-ion battery technology. Two important aspects for improvement are the charging time of the battery and the amount of power that the battery can supply. Both of these aspects require fast Li mobility. Nanomaterials, including inorganic nanotubes, are considered a likely candidate for battery materials in order to improve Li mobility [23-24, 173]. There are numerous examples of inorganic nanotubes storing Lithium and Hydrogen [24, 90, 101, 104]. This was discussed in detail in chapter 2.

Ab initio calculations can be used to predict the Li voltage and activation barrier [153, 174-177] for diffusion in inorganic nanotube of various radii and compare these values to the bulk material. In this chapter, calculations on Lithium storage in inorganic nanotubes are presented. The voltage and activation barrier for Li on the outside and inside of TiS_2 and MoS_2 nanotubes as a function of the radius of curvature were predicted using the curved surface method discussed in chapter 3. Whether a nanotube is polygonal, as discussed in chapter 4, or cylindrical there will be sections where the stacking differs from that seen in the bulk, resulting in a different Li environment. In this chapter results describing how this disordered stacking affects Li voltage and activation barrier between nanotube layers is also discussed.

5.1 Li-Ion Batteries

Lithium ion batteries consist of a positive and a negative electrode, the catode and anode respectively, and an electrolyte. During discharge Li-ions move from the anode to the cathode, through the electrolyte. Lithium ions are forced from the cathode back to the anode during charge. Figure 5.1 shows the parts of the battery and direction of lithium flow during discharge.

The voltage of the battery is determined by the chemical potentials of Li in the cathode and the anode. Specifically, for a lithium battery, the open circuit voltage at charge level x, is given by

$$V(x) = \frac{\mu_{Li}^{anode}(x) - \mu_{Li}^{cathode}(x)}{ze} \qquad (5.1)$$

where μ is the chemical potential of Li in the anode or cathode, z is the charge on the lithium ion (z=1) and e is the electron charge. Voltages discussed in this thesis are relative to a lithium metal anode, so μ_{Li}^{anode} is independent of the charge level. The voltage shown in equation 5.1 is for a specific charge level, or specific lithium concentration in the cathode. The quantity that is actually calculated in this thesis is the average voltage for a range of lithium concentration. The average voltage between $x=x_1$ and $x=x_2$ is determined by the change in Gibbs free energy as the charge state goes from x_1 to x_2.

$$V = \frac{-\Delta G}{(x_2 - x_1)ze} \qquad (5.2)$$

The change in Gibbs free energy, ΔG, can be approximated with first principles calculations [154, 170] as the difference in energy between the anode-cathode system at charge state x_2 and the system at charge state x_1. The Gibbs free energy also includes a $P\Delta V$ term and a $T\Delta S$ term, but the magnitude of these terms is negligible compared to the calculated energy difference. The capacity of the battery is determined by the amount of Li that can be cycled within a given voltage range.

Lithium ion mobility in a material varies exponentially with the energy barrier (activation barrier) the ion must overcome in order to diffuse through the material. Elastic band calculations [165, 178] are used to determine this activation barrier. The activation barrier for diffusion and elastic band calculations are discussed in chapter 3.

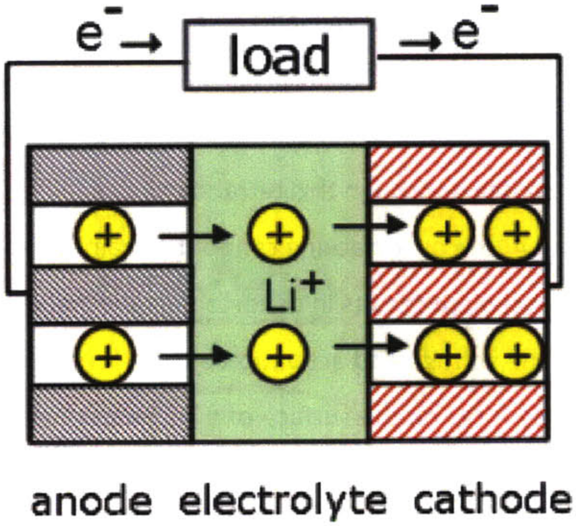

Figure 5.1 Diagram of battery components and Li motion during discharge

5.2 Calculation Details

In this chapter calculations on Li voltage and the activation barrier for Li motion in TiS_2 and MoS_2 structures are reported. All calculations were done using the Vienna Ab-initio Simulation Package (VASP) [166-167]. We have used the generalized gradient approximation (GGA) of Perdew-Burke-Ernzerhof (PBE) to treat the exchange and correlation interaction. The curved surface method, which reproduces the nanotube environment with considerably fewer atoms, was used to determine the variation with curvature of the voltage and activation barrier on the surface of TiS_2 and MoS_2. Distorted slabs were used to determine the effect of stacking on voltage and activation barrier in TiS_2. These methodologies as well as calculation parameters and unit cell optimization was discussed in chapter 3. In this section the TiS_2 and MoS_2 structures are presented and the locations for lithium in these structures are introduced.

5.2.1 TiS2 structure

Bulk TiS_2 forms the CdI_2-1T structure which consists of layers of Ti atoms octahedrally coordinated by S atoms. These triple layers (S-Ti-S) are separated by a Van der Waals gap and stacked such that the titanium atoms project on top of each other. Lithiation occurs by insertion of Li into the octahedral sites in the Van der Waals gap. The octahedral site is formed by three S atoms from each of the layer above and below the Li atom. There is also a tetrahedral Li site, in which Li is coordinated by three S atoms from one triple layer and one S atom from the other triple layer. Diffusion of Li in bulk Li_xTiS_2 occurs by migration from one octahedral site to another, passing through this tetrahedral site [179]. This is shown in figure 5.2. As discussed in chapter 4, the bulk stacking cannot be maintained in nanotubes. Deviation from this bulk stacking arrangement results in distorted octahedral and tetrahedral Li sites, which will obviously affect the voltage and activation barrier for diffusion.

The two possible sites for Li on the surface of a TiS_2 sheet or curved surface can be related to the bulk sites they are derived from. In both sites Li is coordinated by three S atoms at a distance of approximately 2.4 Å. In the A site, derived from the bulk tetrahedral site, the Li atom sits above a S atom from the bottom layer of the sheet, at a distance of approximately 3.4 Å from 3 Ti atoms. In the B site, corresponding to the bulk octahedral site, the LiS_3 tetrahedron shares its sulfur triangle with a Ti-S octahedron and is directly above a Ti atom at a distance of 2.8 Å. Both of these surface sites are shown in figure 5.3.

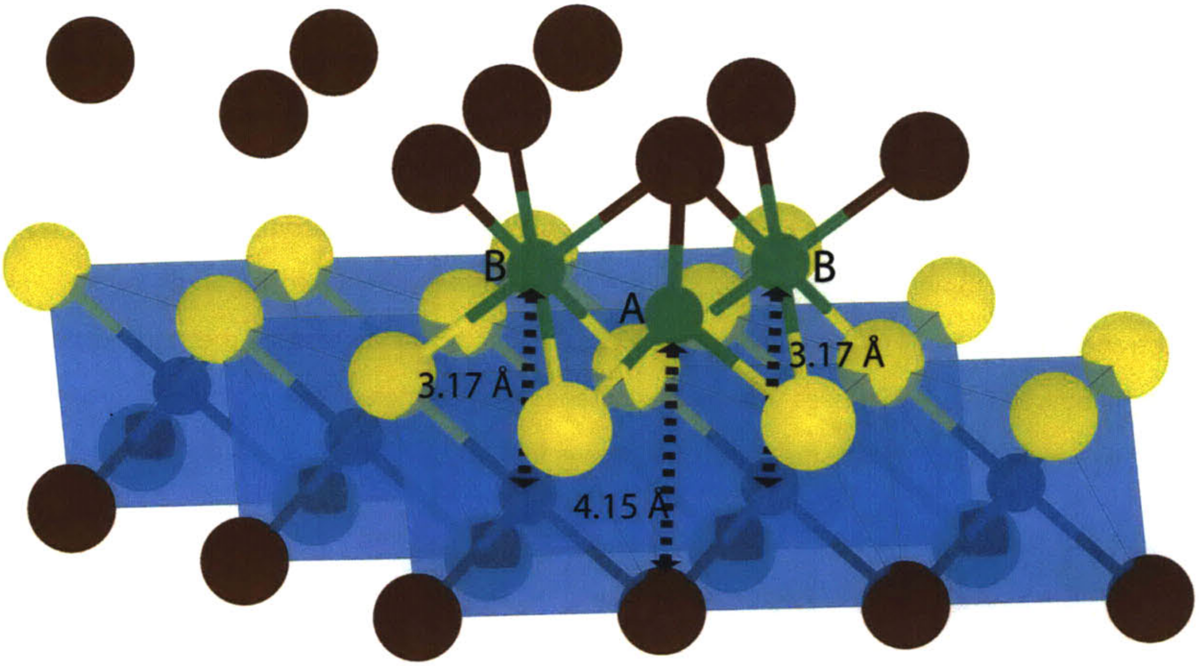

Figure 5.2: Li sites in bulk TiS_2

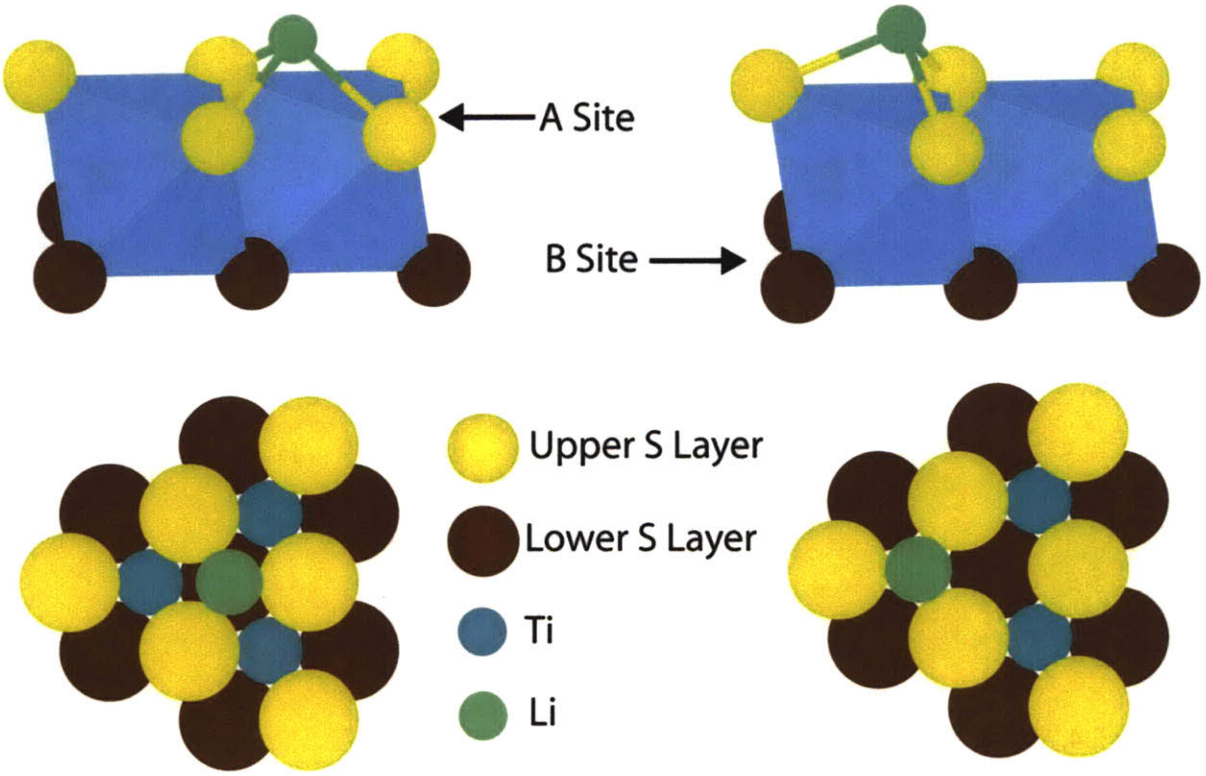

Figure 5.3: Li sites on the surface of TiS_2

5.2.2 MoS2 structure

Bulk MoS_2 has the CdI_2 – 2H structure [180-181]. This is similar to the 1T structure of TiS_2 with a layer of Mo atoms sandwiched between layers of S atoms. However, in the 2H prototype the coordination of the Mo atoms is trigonal prismatic. Mo atoms are stacked in an A-B-A-B sequence, so the unit cell consists of 2 triple layers and Mo atoms in every other layer are stacked on top of each other. As with the 1T prototype, there are octahedral and tetrahedral sites for Li in the Van der Waals gap, but the tetrahedral site is the stable lithium site in bulk MoS_2 and Li passes through the octahedral site when diffusing from one tetrahedral site to another tetrahedral site. Figure 5.4 shows the 2 Li sites on the surface of an MoS_2 sheet.

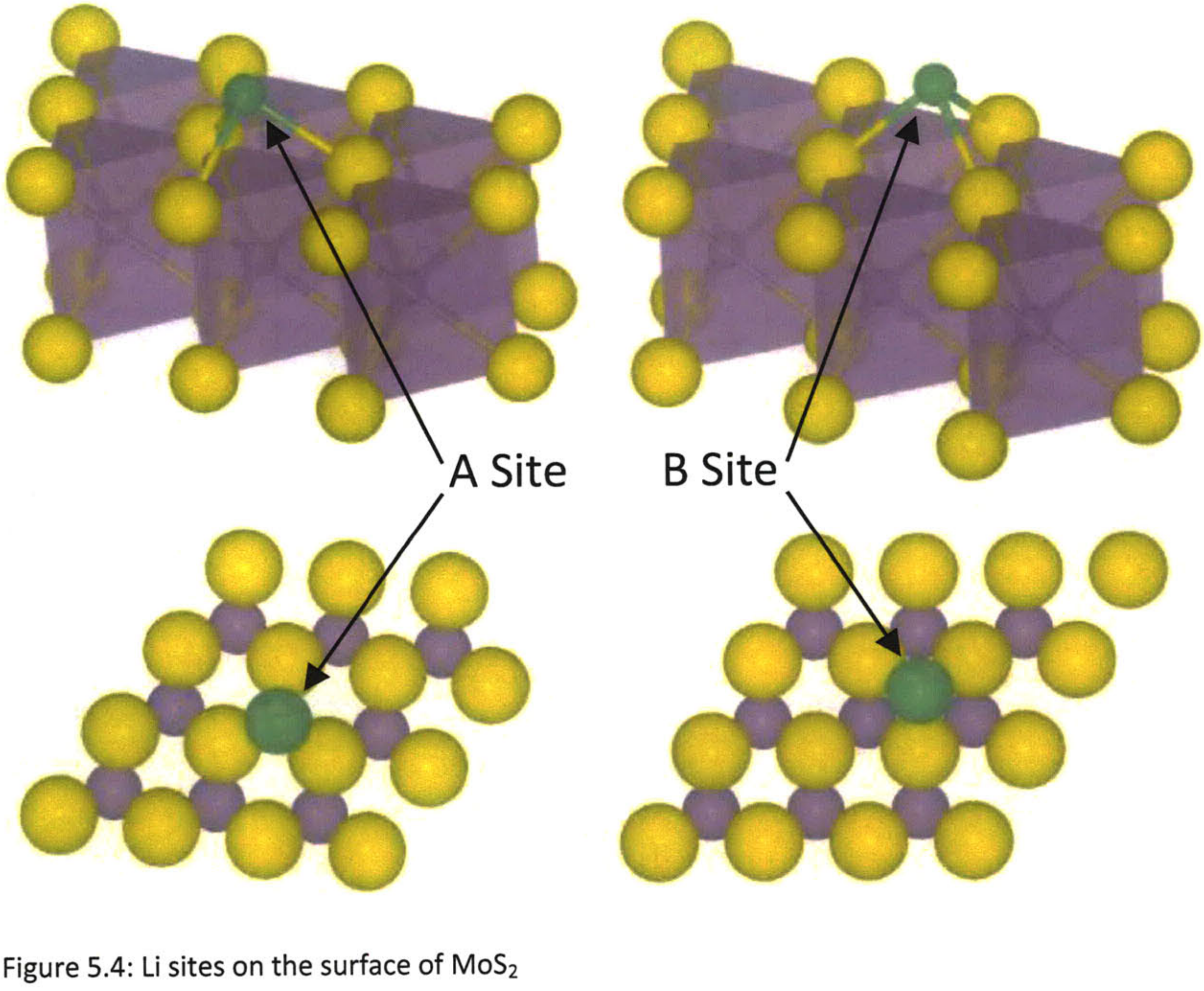

Figure 5.4: Li sites on the surface of MoS_2

5.3 Results

5.3.1 Verification of Curved Surface Method

To verify whether nanotubes can be approximated by curved surfaces we compare the calculated strain energy, Li voltage and Li migration barrier for a true TiS_2 nanotube with a radius of 9.5 Å to the values calculated for a TiS_2 curved surface with the same radius of curvature (Table 5.1). Strain energy is defined as the energy difference per formula unit between the curved surface (or nanotube) and the sheet. We find that the strain energy of the curved surface is 20 meV (14%) larger than for the nanotube. This is a property we do not expect to be accurately reproduced by the curved surface. Strain energy depends on the complete structure of the tube, while the curved surface approximation is intended to model local nanotube properties.

The Li insertion voltage and activation barrier depend mainly on the local environment of the Li atom and, as a result, are expected to be less affected by the curved surface approximation. For the tube with a 9.5 Å radius the lithium voltage is 13 mV (1%) higher than for the curved surface. The activation barrier is found to be accurate to within 9 meV (3%). The accuracy of the curved surface approximation should improve for larger radii of curvature as a larger radius of curvature results in less strain and thus less variation from a sheet. The accuracy of this approximation should also improve with the larger unit cells that were used for all other curved surface calculations, as a larger unit cell for the curved surface is affected less by the inflection points where the curvature inverts.

	Radius = 9.4 Å	**Radius = 9.5 Å**
	Curved Surface	**Full Nanotube**
Strain Energy	145 meV / Formula Unit	125 meV / Formula unit
Lithium Voltage Outside	1.292 V	1.305 V
Lithium Voltage Inside	1.353 V	1.356 V
Activation Barrier for Li Diffusion	261 meV	270 meV

Table 5.1: Calculated Li insertion voltage and activation barrier on a TiS_2 curved surface and TiS_2 nanotube with radius of 9.5 Å.

We also compared the electronic properties of the curved surface with those of the full nanotube. The electron localization function (ELF) is a measure of the electron localization based on the density of electrons of the same spin [182-184]. The ELFs for the TiS_2 nanotube and the curved surface with and without Li are shown in figure 5.5. These images show that in the vicinity of the Li atom the ELF for the curved surface is similar to that for a full nanotube. In addition, inside the nanotube, the ELF is elliptical in contrast with the outside electronic environment, where the ELF functions are spherical around the S atoms. The curvature method is able to reproduce the inner and outer ELF characteristics of the full nanotube lending further support for the approximation of a nanotube by a curved surface.

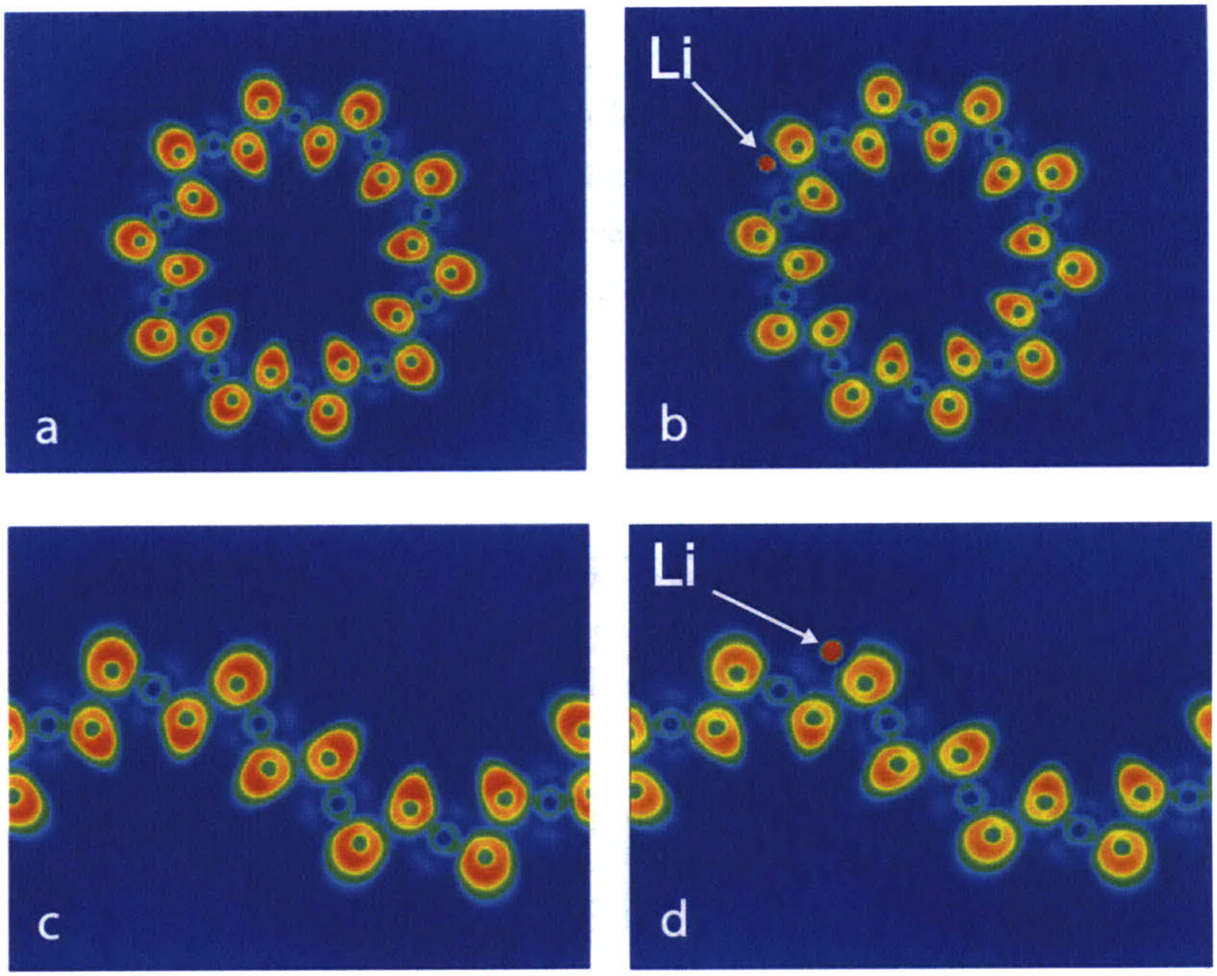

Figure 5.5: Electron Localization Function for full nanotube without Li (a) and with Li (b) and curved surface without Li (c) and with Li (d)

5.3.2 TiS_2 Results

5.3.2.1 Voltage variation with curvature

We compared the Li insertion voltage in the A and B sites of TiS_2 (Table 5.2). The calculated voltages are for the insertion of one Li atom in our curved surface, representing a concentration of approximately 25%. For most curved surfaces the A site is more stable than the B site. For the flat sheet and surfaces with large radius of curvature the difference is small,

~ 40 mV. For Li on the inside of the curved surface there is a transition at small radii where the B site becomes more stable. The Li voltage in the A site, both inside and outside of the curved surface, is displayed in Figure 5.6 as a function of the radius of curvature. This plot shows that the Li insertion voltage both inside and outside of the nanotube decreases as the radius decreases. The horizontal line displays the voltage for a sheet, 1.525 V. For most radii the voltage is slightly lower on the inside of the tube compared to the outside, though the opposite is true at the smallest radii.

	Li inside		**Li outside**	
Radius (Å)	**A Site**	**B Site**	**A Site**	**B Site**
Sheet	1.526 V	1.457 V	1.526 V	1.457 V
100	1.519 V	1.468 V	1.526 V	1.440 V
50	1.505 V	1.468 V	1.517 V	1.408 V
25	1.479 V	1.469 V	1.490 V	1.344 V
10	1.353 V	1.370 V	1.292 V	1.025 V

Table 5.2: Calculated Li voltages in the A and B site inside and outside of a TiS_2 curved surface as a function of radius of curvature

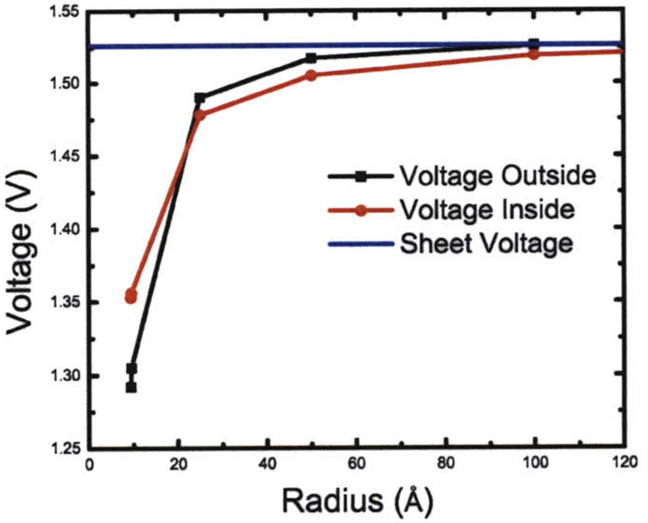

Figure 5.6: Calculated Li voltage on the inside and outside of a TiS_2 curved surface as a function of radius of curvature

Voltage calculations are performed by comparing the energy of TiS_2 + xLi to the energy of Li_xTiS_2. As the Li composition, x, increases, the nearest Li-Li distance decreases. The stronger Li-Li interaction results in a voltage that decreases with increasing composition. The voltages shown in figure 5.6 are for a single Li in our supercells. Due to the shape of the supercell, this results in a short Li-Li distance (3.5 Å) in the direction of the nanotube axis, but large Li-Li distance in the other direction. Typically one would expect a more homogeneous distribution of Li-Li distances to minimize the electrostatic repulsion between them [185-186]. As a result our cell shape may give a lower voltage then what would be observed from a homogeneous cell with the same Li concentration. By comparing the voltage for TiS_2 sheets with various homogeneous Li distributions to those with a short Li-Li distance, we determined that the voltage calculated using our supercells probably more reflects a nanotube with ~25% Li concentration. At a similar Li concentration in the bulk ($Li_{0.25}TiS_2$) the calculated voltage is approximately 2.2 V. The experimentally measured open circuit voltage for $Li_{0.25}TiS_2$ is approximately 2.4 V [84]. Calculations on a flat sheet showed an average voltage of 0.9 V for full lithiation,

$$Li + TiS_2 \rightarrow LiTiS_2$$

compared to an average voltage of 1.9 V for the same reaction in the bulk material.

5.3.2.2 Activation Barrier variation with curvature

Using the Nudged Elastic Band method [165, 178] we find that the path by which Li migrates between two A sites passes through a B site (shown in figure 5.7). This is opposite to bulk Li_xTiS_2, where Li diffuses through a tetrahedral (A) site when migrating between two octahedral (B) sites (figure 5.2).

The maximum energy along the Li^+ migration path (the activation barrier) was calculated for various radii of the tube and is shown in figure 5.8(a and b). The energy along the Li migration path in bulk TiS_2 and on the outside of large nanotubes is shown in figure 5.8a. The barrier on the sheet is approximately 180 meV, which is 200 meV lower than that in the bulk.

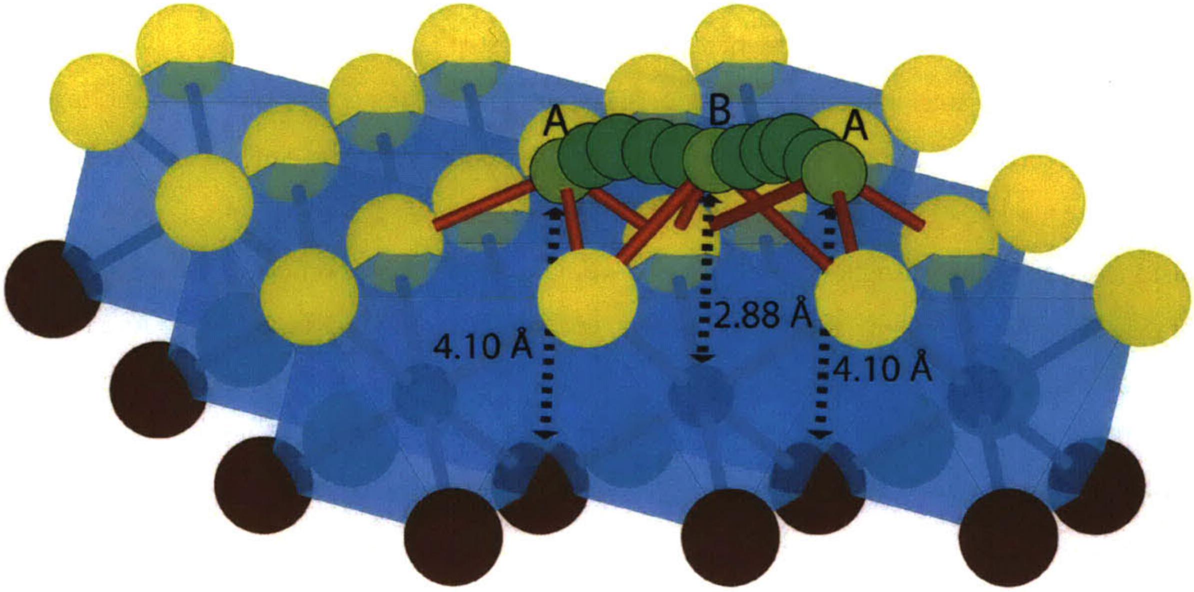

Figure 5.7: The Li diffusion path between two A-sites on the surface of a TiS_2 sheet goes through a B site.

The barriers on curved surfaces are notably higher than those on a sheet. While for a radius of curvature of 100 Å the barrier is only slightly larger than that for a sheet, on a tube with a radius of 25 Å the activation barrier increases to 220 meV. The difference of 200 meV between the activation barrier in the bulk and on the 100 Å nanotube will have a large effect on Li transport since the diffusion coefficient in general varies exponentially with the activation barrier through an Arrhenius-like formula:

$$D \propto e^{\frac{E_A}{kT}} \tag{5.3}$$

At room temperature a difference of 200 meV would result in a change in Li mobility by a factor of over 3000.

The energy along the diffusion path for the smallest nanotubes (figure 5.8b) is considerably different for the path inside and outside of the nanotube, especially at the midpoint of the diffusion path. The activation barrier is 270 meV for Li on the outside, 220 meV for Li on the inside of the 9.5 Å tube. In either case the activation barrier on nanotubes is considerably lower than that in the bulk, but larger than that on a sheet with no curvature. There is little difference between the activation barrier on the curved surface and on a real 9.5 Å radius nanotube.

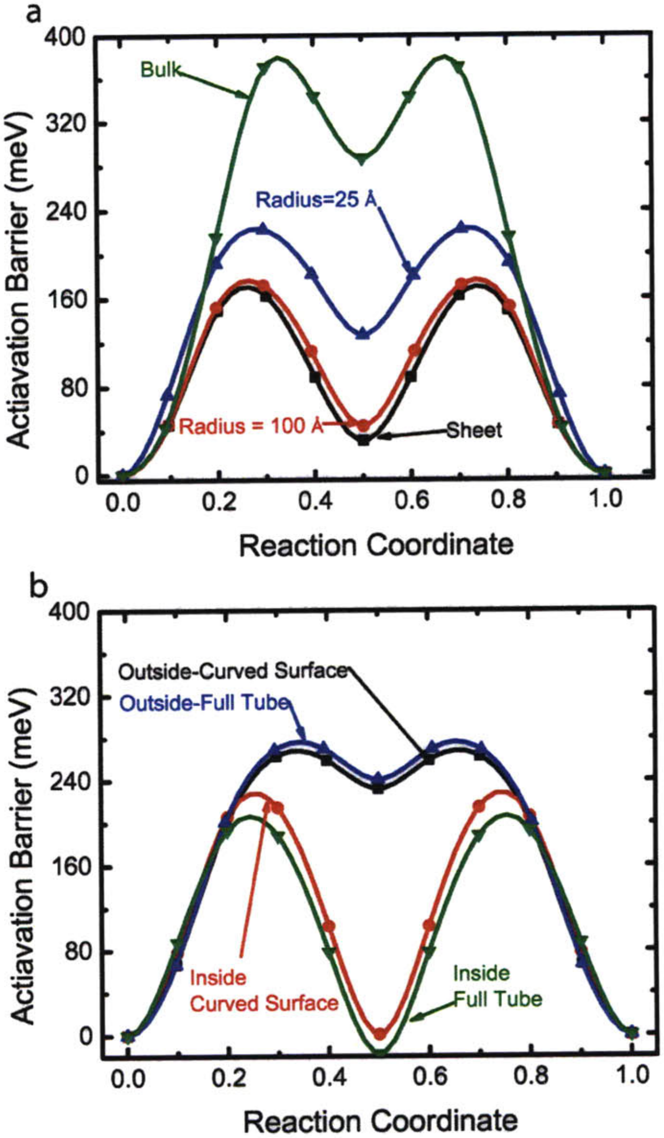

Figure 5.8: (a) Energy along the Li migration path in bulk TiS_2 and on the outside of surfaces with large radius of curvature. (b) Same as (a) but inside and outside of a full nanotube with a radius of 9.5 Å and a curved surface with a radius of 9.4 Å. For the curved surfaces and nanotube reaction coordinate 0 and 1 correspond to site A, and reaction coordinate 0.5 to site B. For the bulk this assignment is inverted.

5.3.2.3 Voltage Variation with Stacking

In inorganic nanotubes it is likely that there will be a variation in stacking alignment. It is useful to understand how the Li voltage and activation barrier for diffusion will be affected by the stacking. This was studied with bulk calculations where the stacking of layers is varied. This method was discussed in chapter 3. The variation in stacking can be parameterized with a variable that varies from 0 to 1. This variable defines the shift of one layer relative to the next layer, normalized by the lattice constant in the direction of the shift, and is referred to here as stacking mismatch. The direction of the shift corresponds to the rolling direction of the nanotube. The results reported in this chapter are for a shift corresponding to zigzag (n,0) nanotubes. Due to symmetry, structures with stacking mismatch of x are identical to those with a stacking mismatch of 1-x, so only values between 0 and 0.5 were examined.

Li voltages in the octahedral and tetrahedral site were examined for stacking mismatches of 0.1, 0.2, 0.3, 0.4 and 0.5. The results of these calculations are shown in figure 5.9. The stable Li site changes from the octahedral to the tetrahedral site at a stacking mismatch of 0.25. The octahedral voltage varies by slightly more than 0.5 volts over the stacking range and the tetrahedral voltage varies by 0.3 V. However, because the stable site changes, the voltage of the stable site varies by less than 0.2 V.

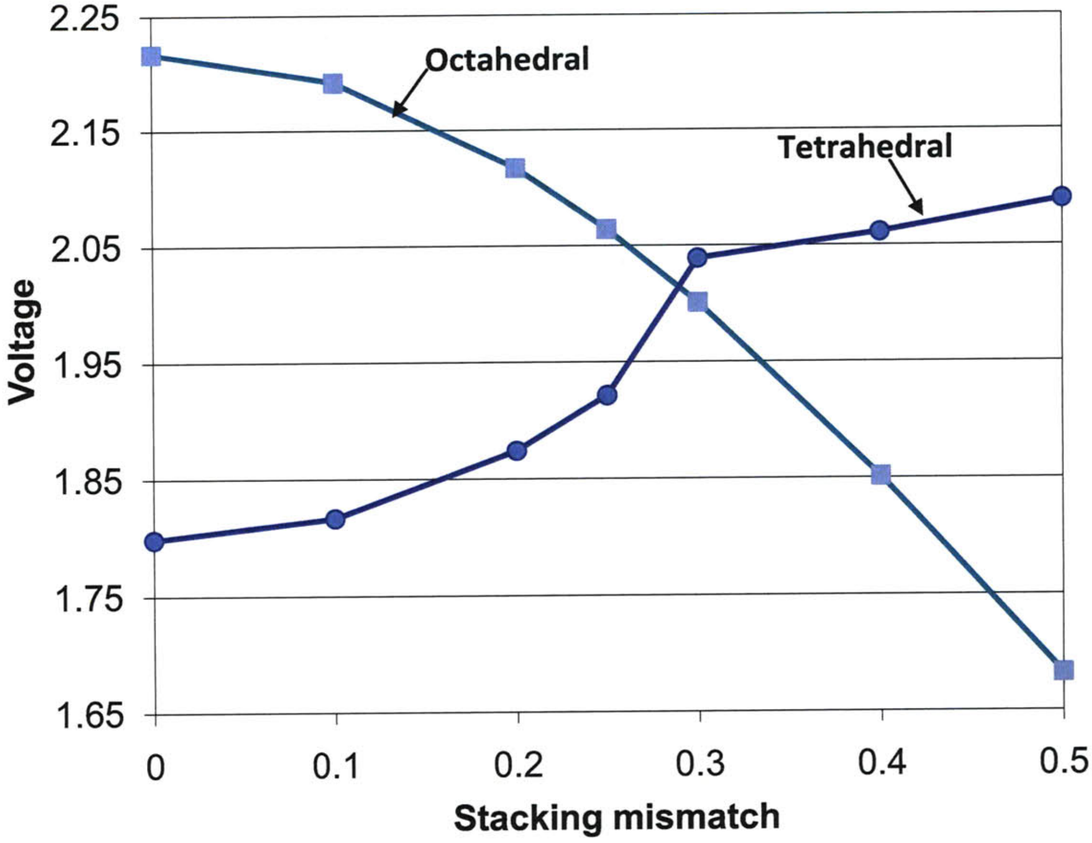

Figure 5.9 Li voltage in TiS_2 as a function of stacking mismatch

5.3.2.4 Activation Barrier Variation with Stacking

The activation barrier for Li diffusion was also studied for each of the 5 stacking mismatches (SM) at which the voltage was calculated. Figure 5.10 shows the energy as Li moves along the migration path for each of the 5 SM values and for ideal bulk stacking (SM=0). The activation barrier is the maximum energy along this path. The values of the activation barrier are given in table 5.3. The activation barrier varies from 585 meV with perfect stacking to 150 meV with a SM value of 0.3. This indicates that stacking disorder could result in a large variation in mobility.

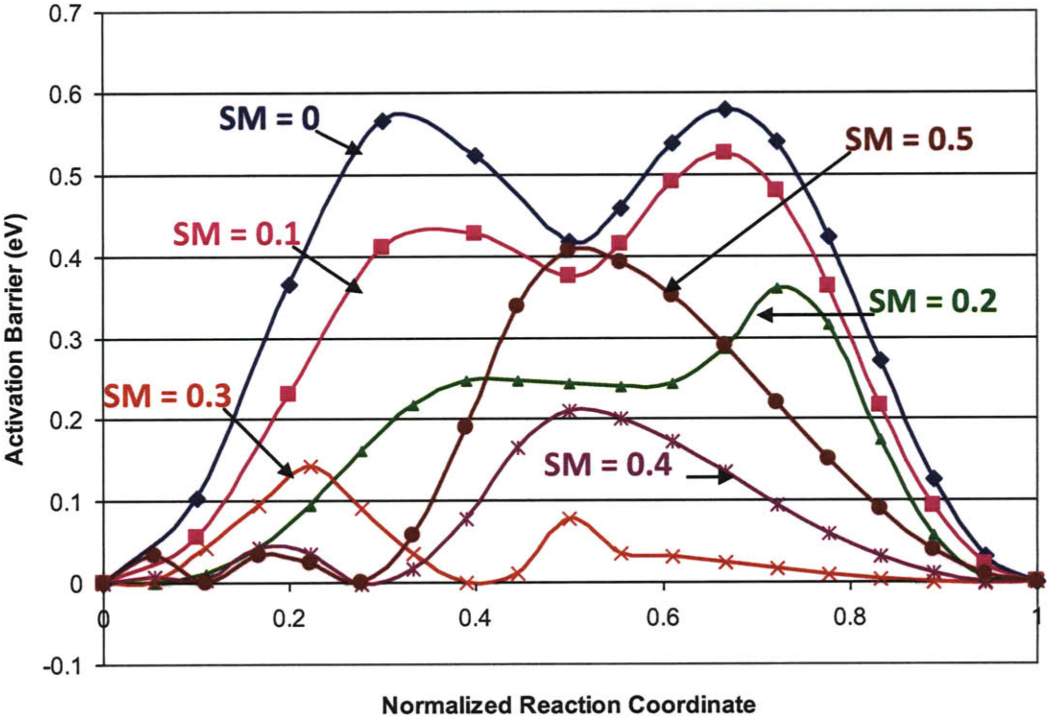

Figure 5.10: Migration energy during Li diffusion in TiS_2 at various levels of stacking mismatch (SM)

Stacking Mismatch	**Activation Barrier (eV)**
0	0.585
0.1	0.530
0.2	0.365
0.3	0.150
0.4	0.215
0.5	0.410

Table 5.3: Activation barrier for Li migration in TiS_2 as a function of stacking mismatch

5.3.3 MoS_2 Results

The curved surface calculations of variation with curvature of Li voltage and activation barrier were also performed for MoS_2 surfaces. These results are shown in this section.

5.3.3.1 Voltage variation with curvature

On the surface of an MoS_2 sheet, the A site, corresponding to the bulk octahedral site, is the stable site. The voltage for Li inside and outside of the curved surface as a function of radius of curvature for MoS_2 is shown in figure 5.11. Contrary to TiS_2, for MoS_2 the variation of voltage with radius of curvature is markedly different between the inside and outside of the curved surface. When Li is inside the curved surface, voltage decreases with a decrease in radius of curvature, as is the case with TiS_2. However, when Li is outside of the curved surface the voltage increases with a decrease in the radius of curvature. Most voltages shown in figure 5.11 are negative, meaning Li will not be stable on the surface. These voltages correspond to a Li composition of approximately 0.25. At more dilute Li concentrations the voltage will be higher, resulting in positive voltages at some radii of curvature.

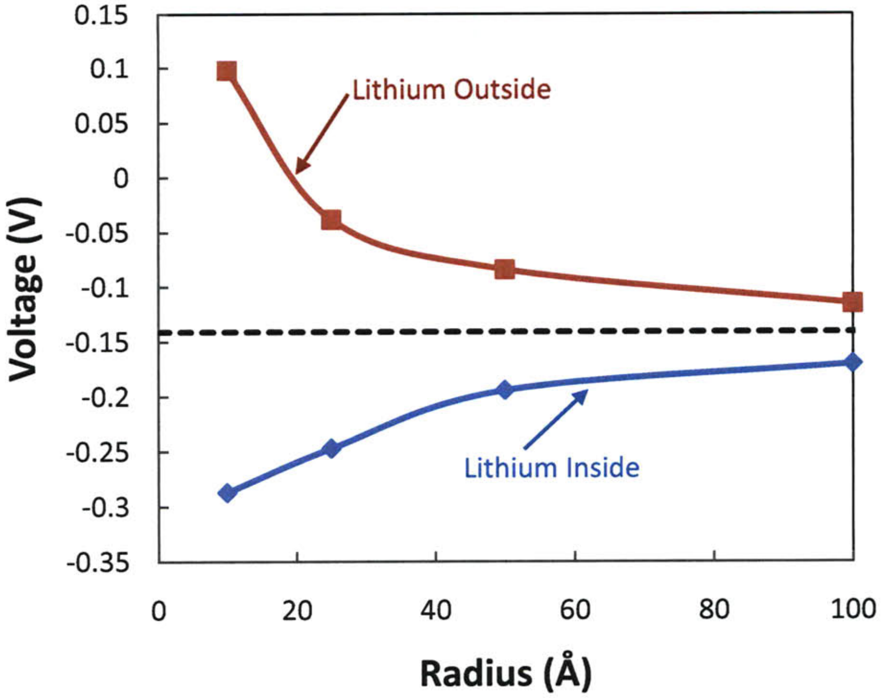

Figure 5.11: Li voltage on the inside and outside of a MoS_2 curved surface as a function of radius of curvature

5.3.3.2 Activation Barrier variation with curvature

The Li migration energy was calculated on the surface of MoS_2 at various radii of curvature. Figure 5.12 shows the migration energy for Li on an MoS_2 sheet as well as inside and outside of MoS_2 curved surfaces with radii of curvature of 100, 25 and 10 Å. The data for a sheet and radius of 100 Å with Li inside or outside are nearly identical, with an activation barrier of 225 meV. At a radius of 25 Å there is no difference between Li inside and outside of the curved surface, but the activation barrier is 205 meV, about 20 meV lower than on the surface of a flat sheet. For a radius of 10 Å, there is a noticeable difference between Li on the inside and outside. When Li is on the inside, the activation barrier is 208 meV. When Li is on the outside the barrier is 146 meV. Also, at a radius of 10 Å the A and B site are very close in energy. In fact, the stable site switches from the A site to the B site when Li is inside the curved surface.

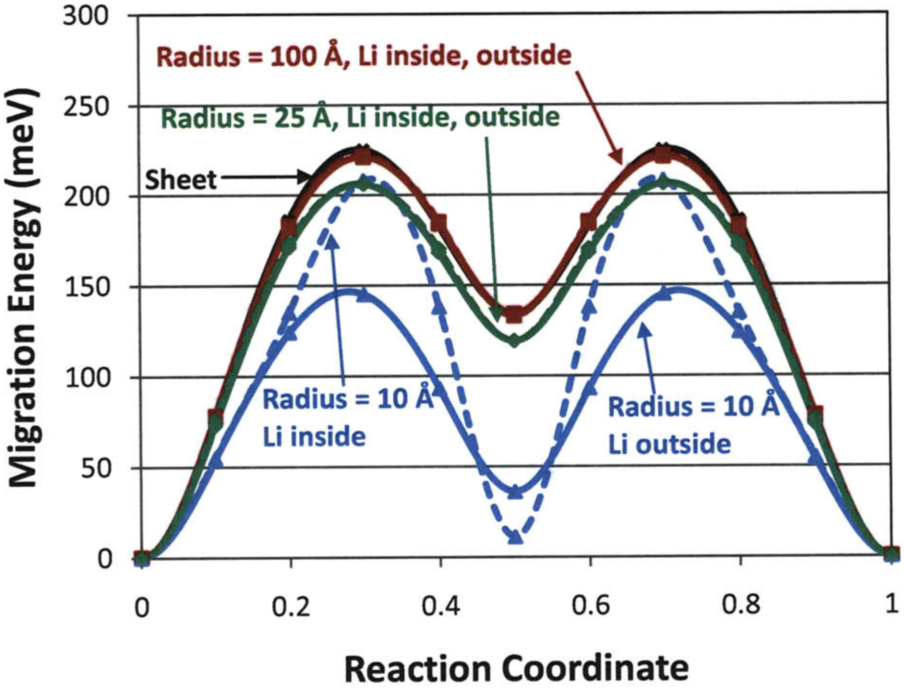

Figure 5.12: Energy along the Li migration path on the outside and inside of MoS_2 surfaces with radii of curvature of 10, 25 and 100 Å and for a flat sheet. For a radius of curvature of 10Å with Li on the inside, reaction coordinate 0 and 1 correspond to site B, and reaction coordinate 0.5 to site A. For all other surfaces this assignment is inverted.

5.4 Discussion

We find that variation with curvature of Li insertion voltage on the surface of a nanotube depends strongly on the material. For TiS_2 nanotubes, the voltage at small radii of curvature is smaller than that for a flat sheet, which in turn is considerably below the voltage for bulk Li insertion. The variation of the Li voltage with the radius of the tube can be understood by considering the electrostatic interaction between Li^+ and the other ions. Figure 5.13 shows the Li position on the surface of a TiS_2 sheet, on the outside of a curved surface, and on the inside of a curved surface. As the radius of curvature decreases the triangle of S atoms which defines the Li site on the outside of the curved surface expands. As a result, the Li atom must move closer to the curved surface to maintain the optimal distance from the S atoms (figure 5.13b). This moves the Li atom closer to the Ti layer, increasing the electrostatic repulsion between the positively charged Li and Ti ions. The balance between the S-Li interaction and the Ti-Li interaction determines the optimum position of the Li. The increased electrostatic interaction with the Ti atom results in an increased site energy for Li and thus a reduction in voltage.

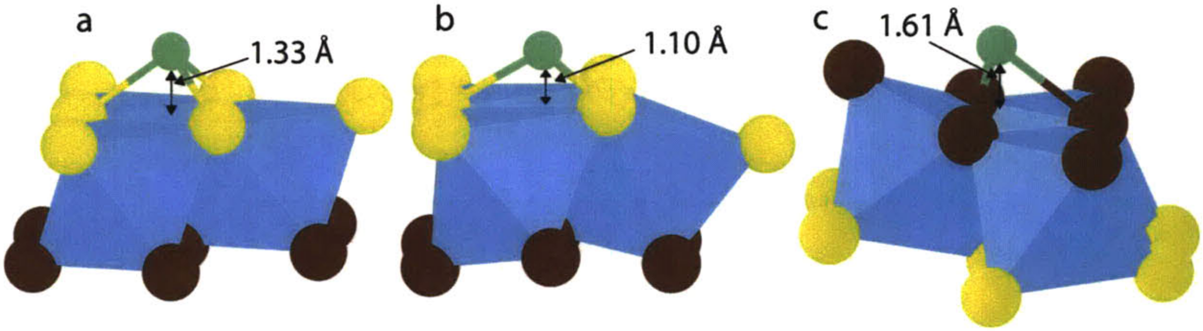

Figure 5.13: Li environment on the surface of a TiS_2 sheet (a), outside (b), and inside (c) a curved surface with a radius of 9.4Å. The distance between the Li atom and the plane of S atoms is shown for each case. Light (yellow online) circles represent S atoms on the outside of the tube. Dark (black online) circles are S on the inside.

This is not the case when Li is on the inside of the curved surface. The triangle of S atoms compresses, causing the Li atom to move away from the surface (figure 5.13c). As a result the lithiation voltage on the inside for the smallest tubes is higher than on the outside. For radii larger than about 25 Å, the main cause for the decrease in Li voltage at the inside position is the inability of the S atoms to relax when the Li atom is inserted. The S atoms are compressed on the inside of the surface and as a result are more constrained than on the flat sheet or outside the curved surface. We tested this hypothesis by calculating Li insertion voltages keeping S atoms fixed to the positions they have in an unlithiated tube. Under this constraint the calculated Li voltage of 1.4 V at the inside position of a 25Å curved surface is the same as on the flat sheet.

The contribution of Li-Ti electrostatics and sulfur relaxation can also be used to explain the increasing activation barrier with decreasing radius for TiS_2 nanotubes. The increase of the barrier due to electrostatic repulsion is apparent in the shape of the energy profile along the migration path in figures 5.8a and 5.8b. The largest energy difference between the path on the outside of a curved surface and the one on the flat sheet occurs at the B-site, which is the midway point of the hop (reaction coordinate ≈ 0.5 on Fig 5.8a). At this position the Li – Ti distance is smallest as the Li atom is directly above the Ti atom. This is confirmed by the data in Fig. 5.14 which shows the distance between the migrating Li atom and the nearest Ti atom. When Li is *outside* the nanotube this minimal Li-Ti distance decreases with decreasing radii, thereby increasing the energy for Li at this position. While the maximum energy along the migration path does not occur at the B site, we believe that the increase in B-site energy lifts up the energy surface and is the major factor in controlling the activation barrier.

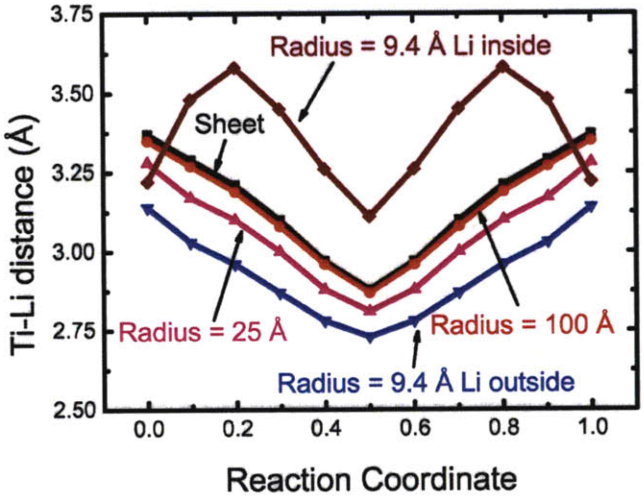

Figure 5.14: Smallest Ti-Li distance along the Li migration path on nanotubes with various radii of curvature

For MoS_2 nanotubes the Li insertion voltage on the surface decreases with decreasing radius of curvature when Li is inside the nanotube, but increases with decreasing radius of curvature when Li is outside the nanotube. This is likely driven by strain energy, which is considerably larger in MoS_2 compared to TiS_2. On the outside of the nanotube the S atoms are under tensile strain. In this case the insertion of Li reduces this tensile strain, lowering the Li site energy and increasing the voltage. Inside the nanotube the S atoms are under compressive strain and the insertion of Li increases the strain, raising the site energy and reducing the voltage.

The activation barrier on MoS_2 nanotubes decreases with decreasing radius of curvature whether Li is inside or outside of the nanotube, opposite to the situation on TiS_2 nanotubes. This can be understood by considering the activated state. In MoS_2 the stable Li site is one where Li sits directly above a Mo atom, while in the activated state Li is equidistant from 3 Mo atoms. As a result the change in site energy with curvature at the stable site is more affected by the Li-Mo interaction than the activated state. The activation barrier is largely determined by the difference between these two sites, so this results in a decreased activation barrier with decreasing curvature for MoS_2 nanotubes.

Activation barrier calculations were performed using a cell twice as long as the cell used for voltage calculations, representing a dilute Li concentration of approximately 5%. It is well known that the Li voltage will decrease with increasing concentration, but the effect of concentration on the activation barrier for Li diffusion is not as clear. This depends on the energy of the system with Li in the activated state relative to the energy with Li in the stable site. We have shown in this paper that for TiS_2 the electrostatic interaction between Li and Ti are crucial in determining the activation barrier for Li diffusion. As the Li concentration is increased the valence on the Ti atoms is reduced. This will reduce the strength of the Li-Ti interaction, which is most influential when Li is in the activated state, possibly resulting in a lower activation barrier.

Surface calculations discussed in this paper were performed on nanotubes and curved surfaces with armchair chirality. Nanotubes with other chiralities will have Li sites and diffusion paths slightly different than those discussed in this paper. Essentially the orientation of bonds relative to the nanotube axis will be different. This will likely result in small quantitative differences, but qualitatively the results should be the same.

It may be possible to draw some more general conclusions about the lithiation voltage and Li mobility on nanotubes of other chemistries. It is the *strain* in the inside and outside surface which indirectly seems to control the change in lithiation voltage from the flat sheet. Tensile strain increases the effective anion-anion distance on the surface drawing the Li atom closer in. Whether this has a strong effect on the potential depends on the nature and distance to the other cations. For a Li insertion site with a Ti^{4+} cation directly below (the B-site in our structure) the effect of curvature is the most pronounced. For structure types where the preferred Li site is not in close proximity to other cations the effect of curvature on the lithiation energy may be significantly less, although, as seen for MoS_2, strain energy may also have a direct effect on lithiation voltage. Overall, curvature effects on the voltage are small above a radius of 25 to 50 Å and can be well approximated by the lithiation voltage of the flat sheet, which should facilitate future investigations of inorganic nanomaterials for battery applications. Most inorganic tubes have radii well above 25 Å, making this finding particularly relevant.

As most of the Li sites in a nanotube are between layers as opposed to on the surface, the effect of stacking on Li voltage and activation barrier is important. The studies presented here show that for TiS_2 the voltage varies by approximately 200 meV with stacking while the activation barrier varies by over 400 meV. This can be understood by looking at the two Li sites. As mentioned previously the activation barrier is largely dependent on the difference in energy between these two sites. In the octahedral site Li is equidistant from 6 S atoms. As the stacking is varied this site becomes distorted and it is not possible for a Li atom to remain equidistant from 6 S atoms. In the tetrahedral site Li is equidistant for 4 S atoms. As this site becomes distorted it is still possible for the Li atom to remain equidistant from these 4 S atoms, so the site energy is less affected by the distortion of the site when stacking is varied compared to the octahedral site.

As is shown in figure 5.9, the tetrahedral voltage actually increases with a stacking mismatch. To help explain this, figure 5.15 shows the effect of interlayer distance on voltage in the two Li sites. The main effect on Li site energy of an increase in interlayer distance is an increase in the Li-S bond length, which also occurs when the stacking is varied. The figure shows that at the experimental lattice parameter, the octahedral voltage is near a maximum, while the tetrahedral voltage is far below the maximum. As the interlayer distance, and thus the Li-S distance, is increased the tetrahedral voltage increases, while the octahedral voltage does not change considerably. This increase in tetrahedral voltage is similar to what is seen in figure 5.9. Because the activation barrier is related to the difference in energy between these two sites while the voltage only depends on the stable site energy the activation barrier is reduced considerably more than the voltage when the stacking is varied. While the curvature of the nanotube can also affect Li voltage and activation barrier between layers, the effect of curvature on the lithium environment is considerably less than the effect of stacking so it is likely that stacking has a larger effect than curvature on voltage and activation barrier between layers.

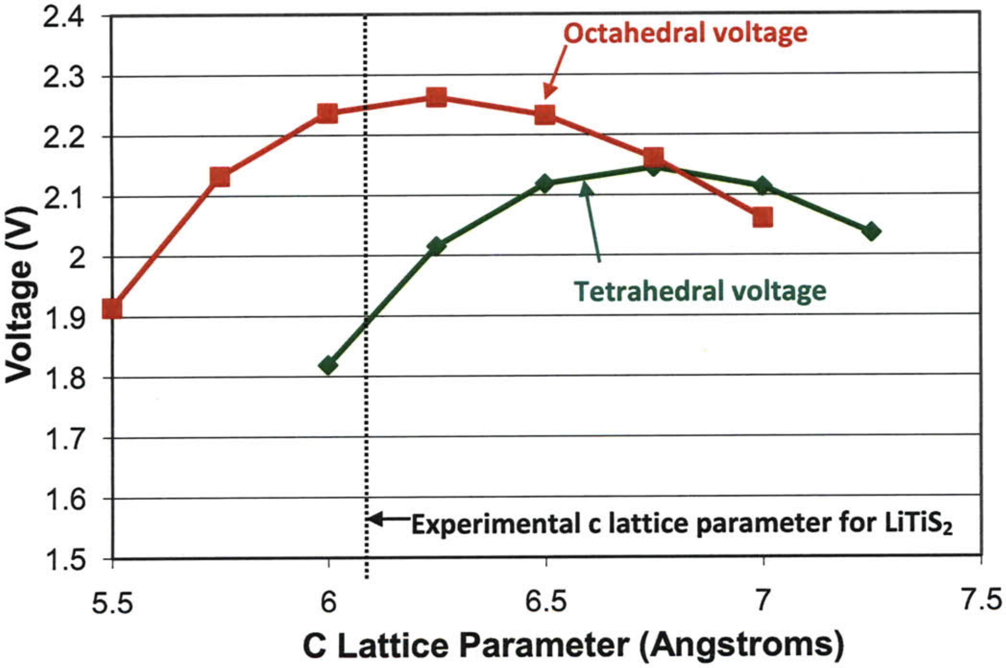

Figure 5.15: Variation in Li voltage with c lattice parameter for the octahedral and tetrahedral sites in TiS_2

The effect of curvature on voltage and activation barrier is minimal at nanotube radii seen experimentally. However, with the polygonal nanotubes discussed in chapter 4 the radius of curvature is considerably lower than the nanotube radius. At the radii of curvature that could occur in polygonal nanotubes, the effect of curvature on surface voltage and activation barrier could be large, although this will only apply to the polygon corners as the flat segments have no curvature. This will be discussed further in chapter 6.

Our results confirm the speculation that nanotubes may function as fast diffusion paths for ions such as Li. Even though the activation barrier increases with decreasing radius for TiS_2 nanotubes it remains well below the value in bulk even for the smallest tubes we tested. The voltage on the nanotube must match the voltage of the primary electrode material in order for the Li sites on the nanotube to be active during Li diffusion. Thus, the surface sites on TiS_2 nanotubes would only improve Li diffusion of electrode materials with a maximum operating voltage near ~ 1.5 V and the interlayer sites would be active when the operating voltage is near 2.0 V.

5.5 Conclusions

In summary, we find that Li diffusion on a flat surface of MoS_2 and TiS_2 is considerably faster than in the bulk. Curved surfaces maintain this mobility advantage and are similar to a flat sheet in their thermodynamic and kinetic properties until the radius of curvature approaches 25 – 50 Å, at which point the activation barrier increases with decreasing radius in TiS_2 and decreases with decreasing radius in MoS_2. But even for the smallest TiS_2 tubes the Li migration barrier is well below the value in the bulk. Li reacts with TiS_2 tubes on the surface in the voltage range 1.3 – 1.5 V which is considerably below the bulk TiS_2 voltage of 2.2 V, making single-walled TiS_2 nanotubes not interesting for cathode applications. However, it is possible that oxide tubes, or sulfide tubes with later transition metals have a higher voltage making them a better match for common cathode materials. As the voltage inside multi-walled tubes is likely to approach that of the bulk, they may be better suited as electrode materials. The activation barrier decreases considerably with stacking mismatch between nanotubes layers, which could provide fast rate capabilities.

The variation of Li voltage and migration barrier in TiS_2 can be well rationalized by considering the electrostatic repulsion with the cations and the strain on the S atoms that form the outside and inside surface. When Li is on the outside of the tube the tensile strain in the outer sulfur layer pulls the Li closer to the cation in the center of the tube, thereby decreasing the voltage. On the inside of the tube it is the compressive strain in the S layer preventing their relaxation which decreases the voltage with decreasing radius. Except for the smallest tubes the Li voltage is higher on the outside of the tube than on the inside, though the difference is small and less than the magnitude of the Li-Li interactions which control the variation of voltage with Li composition. Hence, it is likely that at the limit of lithiation both the inside and outside of a tube will be partially occupied. The activation barrier for Li migration is similarly controlled by electrostatics. The closer Li approaches Ti cations along the migration path the higher the activation barrier.

For MoS_2 nanotubes, strain plays a large role in the variation in voltage with curvature. Li on the outside of the nanotube decreases strain, increasing the voltage, while Li on the inside increases strain, reducing the voltage. The activation barrier for Li on the surface of MoS_2 decreases with decreasing radius because Li in the activated state is farther from the Mo ions than in the stable site.

Stacking also has a large effect on Li voltage and activation barrier. When the stacking is varied in TiS_2, the voltage in the octahedral site is reduced while the voltage in the tetrahedral site increases so the tetrahedral site becomes stable for some stacking orientations. This results in a dramatically reduced activation barrier for Li motion at some stacking orientation.

Our results indicating very high mobility for Li across the surface of TiS_2 and MoS_2 nanotubes are likely to hold for other nanotube chemistries and support the exciting prospect of these materials as additives for high rate Li battery electrodes.

Chapter 6

Summary and Future Work

6.0 Summary and Conclusions

In this thesis I have discussed a polygonal structure of inorganic nanotubes and how curvature and stacking will affect lithium properties of these nanotubes. A lot of information was presented, but there is an important conclusion that can be summarized in one statement for each of these topics.

1. Inorganic layered nanotubes of some chiralities can lower their energy by forming a polygonal cross section if the nanotube radius is above a critical radius, which can be considerably smaller than observed nanotube radii.
2. The curvature and stacking disorder present in layered nanotubes will have an effect on Li voltage and activation barrier for diffusion, but this effect will vary quantitatively and qualitatively from one material to the next.

In this chapter I will summarize the work leading to these statements. I will also discuss how the lithium properties of a nanotube are affected by a polygonal or circular cross section. Then I will wrap up the thesis by discussing the potential experimental and computational future work related to the topics in this thesis.

6.0.1 Polygonal Nanotubes:

In chapter 4 I presented an energy component model that separates the energy of a nanotube into several energy components, each of which can be examined separately. This model was used to compare circular nanotubes and polygonal nanotubes. The strain energy and interfacial energy components were parameterized using atomistic calculations.

The results showed that there is a critical nanotube radius at which polygonal nanotubes will begin to form. This radius is also the radius of curvature at the polygonal corners. The critical radius varies for different materials and depends on the number of nanotube layers. For TiS_2, the critical radius for any number of layers is well below the radius of most inorganic nanotubes seen experimentally. For MoS_2 nanotubes, the critical radius is considerably larger than for TiS_2, but is still below the radius of most inorganic layered nanotubes.

Chirality plays an important role in determining whether or not a polygonal nanotube can form and determines the number of sides to the polygon. The lattice parameter in the rolling direction depends on the chirality. This lattice parameter must be close to the excess length between layers at each corner for a polygonal tube to form without defects. This excess length is determined by the number of sides to the polygon and the interlayer distance. For TiS_2 there are only four chiralities, along with symmetric equivalents, for which polygonal nanotubes can form without defects. The symmetric equivalents of these four chiralities constitute 38% of all nanotube chiralities. The difference between the lattice parameter and the excess length must be accounted for by tensile strain. For most of the allowed chiralities in TiS_2, the tensile strain is small and will not dramatically affect polygonal nanotube formation. Defects could lower the energy of a polygonal nanotube. If the defect energy of a sharp corner is less than the sum of the strain and interfacial energy for a rounded corner then that defect would form and lower the total nanotube energy.

6.0.2 Lithiation Properties of Nanotubes

Many layered materials have potential as energy storage materials because the space between layers is ideal for intercalates such as Li and H. As discussed in chapter 2, there are several layered inorganic nanotubes that have shown the ability to store lithium, hydrogen and magnesium. In chapter 5, we examined the effect of curvature on Li voltage and activation barrier for diffusion on the surface of TiS_2 and MoS_2. In addition we examined the effect of stacking disorder on Li voltage and activation barrier between layers of TiS_2.

When Li is on the surface of a layered material, the voltage is considerably lower than in the bulk of the material, because the coordination of the Li atom is reduced. The activation barrier for diffusion is also lower, because Li is less constrained on the surface compared to between layers. The curvature of the surface can affect the Li voltage and activation barrier relative to a flat sheet. For both TiS_2 and MoS_2 the effect of curvature is small when the radius of curvature is above 50 Å.

When the radius of curvature is below 50 Å the Li voltage inside or outside of a TiS_2 surface decreases with decreasing radius, but for different reasons. When Li is outside of the surface, strain causes the Li ion to move closer to the Ti ion increasing the electrostatic energy. When Li is on the inside, the inability of S atoms to relax causes the decrease in voltage. On MoS_2, the Li voltage increases with decreasing radius when Li is outside the surface, but decreases with decreasing radius when Li is inside the surface. This can be attributed to strain, which is much larger for MoS_2 compared to TiS_2. When Li is placed inside the surface, compressive strain is increased, increasing the Li site energy and reducing the voltage. When Li is outside, tensile strain is decreased, decreasing site energy and increasing the voltage.

The effect of curvature on activation barrier for diffusion is also different between the two materials. In TiS_2, the activation barrier increases with decreasing curvature, whether Li is inside or outside of the material. In MoS_2, the activation barrier decreases in both cases. The qualitative difference between these materials is due to the difference in the activated state. In TiS_2, Li in the activated state during diffusion is closer to a Ti cation than when Li is in the stable site. In MoS_2, Li is closer to a Mo cation in the stable site compared to the activated state.

Stacking disorder results in a decrease in voltage and activation barrier for Li diffusion in TiS_2. As the stacking is varied from the bulk stacking, the octahedral site voltage decreases, while the tetrahedral site voltage increases. The stable site for Li switches from octahedral to tetrahedral at some stacking orientations. The activation barrier is well approximated by the difference between these two voltages. As a result the activation barrier decreases dramatically when the octahedral voltage decreases and the tetrahedral voltage increases.

6.1 Lithiation Properties of Polygonal Nanotubes

The next step is to compare how the lithium properties of polygonal nanotubes will differ from those of circular nanotubes based on the results discussed in this thesis. Due to the large difference between the voltage on the surface and the voltage between layers it is unlikely that these two regions will both be active at the same time. In order for the nanotube surface to be active, the gaps between nanotube layers will be fully lithiated.

When a nanotube has a circular cross section, the radius of curvature is the same as the radius of the nanotube. For most nanotubes this radius is larger than 50 Å. Li voltage and activation barrier do not change considerably above this radius so curvature will have little effect on these properties on the surface of a circular nanotube. For TiS_2 nanotubes with a polygonal cross section the radius of curvature at the corners will be considerably smaller than 50 Å so curvature can effect voltage and activation barrier. The voltage will be lower and the activation barrier will be higher at the corners compared to the flat segments of the nanotube. For MoS_2 polygonal nanotubes, the radius of curvature is only slightly below 50 Å so variation in voltage and activation barrier compared to a circular nanotube will be small. Surfaces constitute a small portion of multi-walled nanotubes. They can provide dramatically improved mobility, but when the surface is active most of the nanotube is inactive. This is not the case for single-walled nanotubes, but instances of single-walled inorganic nanotubes are rare [28, 187].

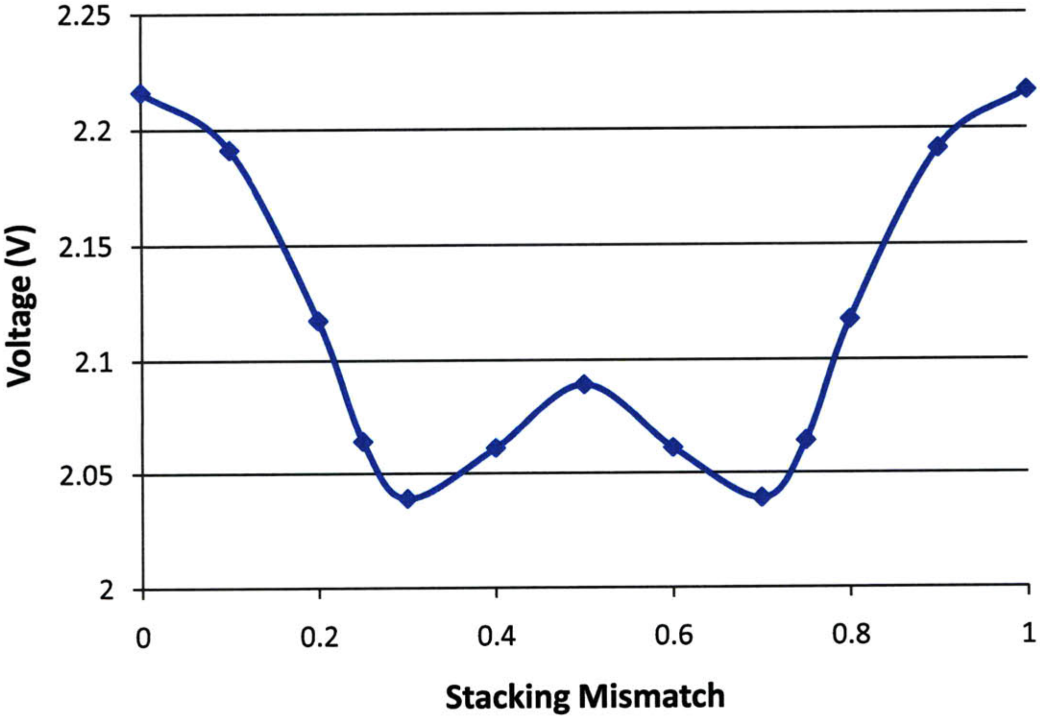

Figure 6.1: Li voltage between layers of TiS_2 as a function of stacking mismatch. The voltage is highest when there is no stacking disorder (SM=0 or 1) and varies by 0.2 V over the full range of stacking mismatch.

When Li is between layers of a TiS_2 nanotube stacking will affect Li properties. Figure 5.9 showed the voltage in each of the two sites as a function of stacking mismatch. Figure 6.1 shows the voltage of the stable site as a function of stacking mismatch. The voltage is highest when there is no stacking disorder and only varies by 0.2 V throughout the range of stacking mismatch. For a circular nanotube, stacking disorder will gradually vary throughout the circumference of the nanotube. The effect of Li concentration on voltage must be known in order to determine precisely how the concentration will vary, but we know that the areas with a lower voltage will have a lower Li concentration than the areas with a higher voltage. Figure 5.10 showed that the activation barrier is lowest at a stacking mismatch of 0.3, which is also the stacking mismatch with the lowest voltage. This results in channels for Li diffusion where the activation barrier and the Li concentration are lower than in the rest of the nanotube. The main difference between polygonal nanotubes and circular nanotubes in regards to stacking disorder is that in polygonal nanotubes the stacking varies over a small portion of the nanotube, specifically at the polygonal corners. There is no stacking mismatch in the flat segments of the nanotube. The channels for Li diffusion will still exist, but the size of these channels will be smaller. On the other hand, the average Li voltage in a polygonal nanotube will be higher than for a circular nanotube because a larger fraction of the nanotube has ideal stacking, where the voltage is highest.

6.2 Suggestions for Future Work

The work discussed in this thesis would be well supported with experimental work to verify the existence of polygonal inorganic nanotubes and the properties of lithium on these nanotubes. In addition, further computational work could expand the applicability of the results to other materials and intercalates. Suggestions for experimental and computational future work are presented in this section.

6.2.1 Experimental Work

The results of this thesis show that inorganic nanotubes can lower their energy by forming a polygonal cross section. Hopefully this will inspire future experimental examinations of the structure of inorganic nanotubes. It is not easy to determine the cross section of a nanotube. Polygonal carbon nanotubes have been identified primarily due to a change in interlayer spacing [116]. This is possible with carbon nanotubes because graphite has a known disordered stacking (turbostratic) phase with an interlayer spacing that is slightly larger than that for the ordered phase [116]. There is not a known disordered stacking phase for most layered inorganic materials, although some inorganic layered nanotubes show a larger interlayer spacing than the bulk material [47-49]. Studies looking for a disordered stacking phase in layered inorganic materials would be beneficial in understanding the increased layer spacing in some inorganic nanotubes. Evidence that the spacing corresponds to a turbostratic phase of the material would increase the likelihood that the nanotubes with an increased layer spacing have circular cross sections, while those without this increased spacing may have a polygonal cross section.

Most images of nanotubes show the cross section along the length of the tube as opposed to the ends of the tube [3, 8]. This lengthwise cross section will often look the same for circular and polygonal tubes. A large number of images must be examined in order to see evidence of polygonal tubes [123, 125]. Currently there is limited knowledge of the chirality of inorganic nanotubes [188]. Because the chirality of nanotubes is important to the polygonal cross section it would be useful to have more knowledge of the chirality of inorganic nanotubes.

Many nanotubes have shown the ability to store lithium, but voltage profiles and rate capabilities are not typically reported. The work in this thesis has shown that nanotubes could dramatically increase rate capabilities due to the lower activation barrier with stacking disorder. Extensive studies of rate capabilities of TiS_2 or other nanotubes could support this result.

6.2.2 Computational Work:

This study has shown that first principles methods can effectively be used to study various properties of nanotubes. The structure and Li properties of two types of nanotubes were investigated using the curved surface method. These studies showed that the effect of curvature on Li voltage and activation barrier can vary tremendously from one material to the next. Further studies of other materials would be useful in order to determine some general guidelines about how curvature and stacking will affect Li voltage and activation barrier for diffusion. By replacing lithium with magnesium, hydrogen or other intercalates, the effect of curvature and stacking on storage of these materials can also be examined.

In addition, the basic idea of simulating a nanotube environment through methods such as curved surfaces and distorted slabs can be an effective way of studying nanotube properties. Many of the important interactions in the MX_2 nanotubes investigated in this work can possibly be represented using a simple potential model as opposed to the density functional theory methods used here. The use of a potential model could provide similar results with a great reduction in computation time, allowing the investigation of larger structures. Also, classical methods, such as the finite element method, could be used in conjunction with atomistic calculations to model the entire nanotube. This would be especially useful with polygonal nanotubes, which consist of two distinct regions, the flat and curved segments of the polygon. This type of analysis was used by Pantano et al. to study defects and chirality of carbon nanotubes [189]. Hopefully the work discussed here will assist further computational studies of nanotubes.

Bibliography

1. Birkett, P. R. *Annu. Rep. Prog. Chem.* **2004**, *100*, 461

2 Tenne, R. *Chem. Eur. J.* **2002**, *8*, 5296

3. Tenne, R. *J. Mater. Res.* **2006**, *21*, 2726

4. Tenne, R. *Nature Nanotechnology* **2006**, *1,* 103

5. Bar-Sadan, M.; Kaplan-Ashiri, I.; Tenne, R., *Eur. Phys. J. Special Topics* **2007,** *149*, 71

6. Patzke, G. R.; Krumeich, F.; Nesper, R. *Angew. Chem. Int. Ed.* **2002**, *41*, 2446

7. Remskar, M. *Adv. Mater.* **2004,** *16,* 1497

8. Rao, C. N.; Nath, M. *Dalton Trans.* **2003,** 1

9. Tenne, R.; Rao, C. N. *Phil. Trans. R. Soc. Lond. A.* **2004,** *362,* 2099

10. Enyashin, A. N.; Seifert, G. *Phys. Stat. Sol.* **2005,** *242*, 1361

11. Ivanovskaya, V. V.; Enyashin, A. N.; Ivanovskii, A. L. *Mendeleev Commun.* **2003**, *13*, 5

12. Ivanovskaya, V. V.; Seifert, G. *Solid State Communications* **2004**, *130*, 175

13. Ivanovskaya, V. V.; Seifert, G.; Ivanovskii, A. L. *Semiconductors*, **2005**, *39*, 1058

14. Enyashin, A.; Ivanovskii, A. *Inorganic Materials* **2005**, *41*, 1118

15. Srivastava, D.; Menion, M.; Cho, K. *Computing in Science and Engineering* **2001**, *3*, 42.

16. Meunier, V.; Kephart, J.; Roland, C.; Bernholc, J. *Physical Review Letters* **2002**, *88*, 075506.

17. Lee, Y.; Nardelli, M.; Marzari, N. *Physical Review Letters* **2005**, *95*, 076804.

18. Charlier, J. C.; Lamin, P.; Ebbessen, T. W. *Phys. Rev. B* **1996,** 54, R8377

19. Bishop, C. L.; Wilson, M. *Molecular Phys.* **2008**, *106*, 1665

20. Tibbetts, K.; Miranda, C. R.; Meng, Y. S.; Ceder, G. *Chem Mater.* **2007**, 19, 5302

21. Sides, C. R.; Li, N.; Patrissi, C. J.; Scrosati, B.; Martin, C. R. *MRS Buletin*, **2002**, 604

22. Chen, J.; Wu, F. *Appl. Phys. A.* **2004,** *78,* 989

23. Arico, A. S.; Bruce, P.; Scrosati, B.; Tarascon, J. M.; Van Schalkwijk, W. *Nature Materials* **2005,** *4,* 366

24. Cheng, F.; Chen, J. *J. Mater. Res.* **2006,** *21,* 2744

25. Terrones, M.; Terrones, H.; Banhart, F.; Charlier, J.-C.; Ajayan, P. M. *Science* **2000,** *288*, 1226

26. Journet, C.; Maser, W. K.; Bernier, P.; Loiseau, A.; Lamy de la Chepelle, M.; Lefrant, S.; Deniard, P.; Lee, R.; Fischer, J. E. *Nature* **1997**, *388*, 756

27. Malliakas, C. D.; Kanatzidis, M. G. *J. Am. Chem. Soc.* **2006**, *128*, 6538

28. Remskar, M.; Mrzel, A.; Skraba, Z.; Jesih, A.; Ceh, M.; Demsar, J.; Stadelmann, P.; Levy, F.; Mihailovic, D. *Science* **2001**, *292*, 479

29. Loiseau, A.; Willaime, F.; Demoncy, N.; Hug, G.; Pascard, H. *Phys. Rev. Lett.* **1996**, *76*, 4737

30. Afanasiev, P. ; Geantet, C. ; Thomazeau, C. ; Jouget, B. *Chem Comm* **2000**, 1001

31. Peng, Y.; Meng, Z.; Zhong, C.; Lu, J.; Yang, Z.; Qian, Y. *Mater. Chem. Phys.* **2002**, *73*, 327

32. Wang, S.; Li, G.; He, Y.; Yin, H.; Xu, Z.; Zou, B. *Mater. Lett.* **2006**, *60*, 815

33. Lavayen, V.; Mirabal, N.; O'Dwyer, C.; Santa Ana, M. A.; Benavente, E.; Sotomayor Torres, C. M.; Gonzalez, G. *App. Surf. Sci.* **2007**, *253*, 5185

34. Rosentsveig, R.; Margolin, A.; Feldman, Y.; Popovitz-Biro, R.; Tenne, R. *Chem. Mater.* **2002,** *14*, 471

35. Feldman, Y.; Wasserman, E.; Srolovitz, D. J.; Tenne, R. *Science* **1995**, *267*, 222

36. Tenne, R.; Margulis, L.; Genut, M.; Hodes, G. *Nature* **1992**, *360*, 444

37. Rothschild, A.; Frey, G. L.; Homyonfer, M.; Tenne, R.; Rappaport, M. *Mat. Res. Innovat.* **1999**, *3*, 145

38. Chopra, N. G.; Luyken, R. J.; Cherrey, K.; Crespi, V. H.; Cohen, M. L.; Louie, S. G.; Zettl, A. *Science* **1995**, *269*, 966

39. Iijima, S. *Nature* **1991**, 354, 56

40. Tourillon, G.; Pontonnier, L.; Levy, J. P.; Langlais, V. *Electrochem. Solid State Lett.* **2000**, *3*, 20

41. Li, N.; Li, X.; Yin, X.; Wang, W.; Qiu, S. *Solid State Comm.* **2004**, *132*, 841

42. Zhao, J.; Wang, X.; Sun, T.; Li, L. *Nanotechnology* **2005**, *16*, 2450

43. Endo, M.; Katoh, A.; Sugiura, T.; Shiraishi, M. *Extended Abrstracts 18th Biennial Conf. on Carbon* **1987**, 151

44. Speck, J. S.; Endo, M.; Dresselhaus, M. S. *J. Cryst. Growth* **1989**, *94*, 834

45. Chianelli, R. R.; Prestridge, E. B.; Pecoraro, T. A.; DeNeufville, J. P. *Science* **1979**, *203*, 1105

46. Sanders, J. V. *Ultramicroscopy* **1986**, *20*, 33

47. Nath, M.; Rao, C. N. R. *Angew Chem. Int. Ed.* **2002**, *41*, 3451

48. Nath, M.; Rao, C. N. R. *J. Am. Chem. Soc.* **2001**, *123*, 4841

49. Tenne, R.; Homyonfer, M.; Feldman, Y. *Chem. Mater.* **1998**, *10*, 3225

50. Ma, R.; Bando, Y.; Sasaki, T. *J. Phys. Chem. B* **2004**, *108*, 2115

51. Schmidt, O. G.; Eberl, K. *Nature* **2001**, *410*, 168

52. Wang, W.; Varghese, O. K.; Paulose, M.; Grimes, C. A. *J. Mater. Res.* **2004**, *19*, 417

53. Maniwa, Y.; Fujiwara, R.; Kira, H.; Tou, H.; Nishibori, E.; Takata, M.; Sakata, M.; Fujiwara, A.; Zhao, X.; Iijima, S.; Ando, Y. *Phys. Rev. B* **2001**, *64*, 073105

54. Ebbessen, T. W.; Ajayan, P. M. *Nature* **1992**, *358*, 220

55. Maser, W. K.; Munoz, E.; Benito, A. M.; Martinez, M. T.; de la Fuente, G. F.; Maniette, Y.; Anglaret, E.; Sauvajol, J. L. *Chem. Phys. Lett.* **1998**, *292*, 587

56. Min, Y. S.; Bae, E. J.; Kang, D.; Ko, J. H.; Park, W. *J. Am. Chem. Soc.* **2005**, *127*, 12498

57. Bae, E. J.; Min, Y. S.; Kang, D.; Ko, J. H.; Park, W. *Chem. Mater.* **2005**, *17*, 5141

58. Govindaraj, A.; Rao, C. N. R. in *The Chemistry of Nanomaterials*, ed. C. N. R. Rao, A. Muller and A. K . Cheetham, Wiley-VCH Verlag GmbH & Co, Weinheim, **2004**, Vol. 1;

59. Hulteen, J. C.; Martin, C. R. *J. Mater. Chem.* **1997**, *7*, 1075

60. Tang, C.; Bando, Y.; Sato, T.; Kurashima, K. *Chem. Commun.* **2002**, 1290

61. Chhowalla, M.; Amaratunga, G. A. J. *Nature* **2000**, *407*, 164.

62. Parilla, P. A.; Dillon, A. C.; Jones, J. M.; Riker, G.; Schulz, D. L.; Ginley, D. S.; Heben, M. J. *Nature* **1999**, *397*, 114

63. Parilla, P. A.; Dillon, A. C.; Parkinson, B. A.; Jones, J. M.; Alleman, J.; Riker, G.; Schulz, D. L.; Ginley, D. S.; Heben, M. J. *J. Phys. Chem. B* **2004**, *108*, 6197

64. Hershfinkel, M.; Gheber, L. A.; Volterra, V.; Hutchison, J. L.; Margulis, L.; Tenne, R. *J. Am. Chem. Soc.* **1994**, *116*, 1914

65. Tsirlina, T.; Feldman, Y.; Homyonfer, M.; Sloan, J.; Hutchison, J. L.; Tenne, R. *Fullerene Sci. Tech.* **1998**, *6*, 157

66. Nath, N.; Kar, S.; Raychaudhuri, A.; Rao C. *Chem. Phys. Lett.* **2003**, *368*, 690.

67. Spahr, M. E.; Stoschitzki-Bitterli, P.; Nesper, R.; Haas, O.; Novak, P. *J. Elect. Chem. Soc.* **1999**, *146*, 2780

68. Du, G.; Chen, Q.; Yu, Y.; Zhang, S.; Zhou, W.; Peng, L. M. *J. Mater. Chem.* **2004**, *14*, 1437

69. Kasuga, T.; Hiramatsu, M.; Hoson, A.; Sekino, T.; Niihara, K. *Langmuir* **1998**, *14*, 3160

70. Kasuga, T.; Hiramatsu, M.; Hoson, A.; Sekino, T.; Niihara, K. *Adv. Mater.* **1999**, *11*, 1307

71. Seo, D. S.; Lee, J. K.; Kim, H. *J. Crystal Growth* **2001**, *229*, 428

72. Mu, C.; Yu, Y.; Wang, R.; Wu, K.; Xu, D.; Guo, G. *Adv. Mater.* **2004**, *16*, 1550

73. Zhang, X. H.; Xie, Z. X.; Jiang, Z. Y.; Xu, X.; Xiang, J.; Huang, R. B.; Zheng, L. S. *Chem. Commun.* **2004**, *1106*

74. Rao, C. N. R.; Govindaraj, A. *Nanotubes and Nanowires*, Royal Society of Chemistry: London, UK, **2005**

75. Gong, D.; Grimes, C. A.; Varghese, O. K.; Hu, W.; Singh, R. S.; Chen, Z.; Dickey, E. C. *J. Mater. Res.* **2001**, *16*, 3331

76. Birkett, P. R. *Annu. Rep. Prog. Chem.* **2006**, *102*, 420

77. Rapoport, L.; Fleischer, N.; Tenne, R. *J. Mater. Chem.* **2005**, *15*, 1782

78. Rochschild, A.; Cohen, S.; Tenne, R. *App. Phys. Lett.* **1999**, *75*, 4025

79. Zhu, Y.; Sekine, T.; Brigatti, K.; Firth, S.; Tenne, R.; Rosentsveig, R.; Kroto, H.; Walton, D. *J. Am. Chem. Soc.* **2003**, *125*, 1329.

80. Mor, G.; Carvalho, M.; Varghese, O.; Pishko, M.; Grimes, C. *J. Mater. Res.* **2004**, *19*, 628.

81. Adachi, M.; Marata, Y.; Okada, I.; Yoshikawa, S. *J. Electrochem. Soc.* **2003**, *150*, G488.

82. Lei, Y.; Zhang, L.; Meng, G.; Li, G.; Zhang, X.; Liang, C.; Chen, W.; Wang, S. *App. Phys. Lett.* **2001**, *78*, 1125.

83. Winter, M.; Besenhard, J. O.; Spahr, M. E.; Novak, P. *Adv. Mater.* **1998**, *10*, 725

84. Whittingham, M. S. *Science* **1976**, *192*, 1126

85. McCanny, J. V. *J. Phys. C:Solid State Phys.* **1979**, *12*, 3263

86. A. M. Seayad, A. M.; D. M. Antonelli, D. M. *Adv. Mater.* **2004**, *16,* 765

87. Ma, R.; Bando, Y.; Zhu, H.; Sato, T.; Xu, C.; Wu, D. *J. Am. Chem. Soc.* **2002**, *124*, 7672

88. Bavykin, V.; Lapkin, A. A.; Plucinski, P. K.; Friedrich, J. M.; Walsh, F. C. *J. Phys. Chem. B.* **2005**, *109*, 19422

89. Chen, J.; Li, S. L.; Tao, Z. L.; Shen, Y. T.; Cui, C. X. *J. Am Chem. Soc.* **2003**, *125*, 5284

90. Chen, J.; Kuriyama, N.; Yuan, H.; Takeshita, H. T.; Sakai, T. *J. Am. Chem. Soc.* **2001**, *123*, 11813

91. Chen, J.; Li, S. L.; Tao, Z. L. *J. Alloys and Compounds* **2003**, *356-357*, 413

92. Zhou, Y.; Cao, L.; Zhang, F.; He, B.; Li, H. *J. Electr. Chem. Soc.* **2003**, *150*, A1246

93. Gao, X. P.; Lan, Y.; Zhu, H. Y.; Liu, J. W.; Ge, Y. P.; Wu, F.; Song, D. Y. *Electrochem. Sol. State. Lett.* **2005**, *8*, A26

94. Li, J.; Tang, Z.; Zhang, Z. *Electrochem. Solid-State Lett.* **2005,** *8*, A316

95. Kim, J.; Cho, J. *J. Electrochem. Soc.* **2007**, *154*, A542

96. Armstrong, G.; Armstrong, A. R.; Canales, J.; Bruce, P. G. *Electrochem. Solid-State Lett* **2006**, *9*, A139

97. Li, J.; Tang, Z.; Zhang, Z. *Electrochem. Comm.* **2005**, *7*, 62

98. Augustsson, A.; Schmitt, T.; Duda, L.-C.; Nordgren, J.; Nordlinder, S.; Edstrom, K.; Gustafsson, T.; Guo, J.-H. *J. Appl. Phys.* **2003**, *94*, 5083

99. Nordlinder, S.; Nyholm, L.; Gustafsson, T.; Edstrom, K. *Chem. Mater.* **2006**, *18*, 495

100. Dobley, A.; Ngala, K.; Yang, S.; Zavalij, P. Y.; Whittingham, M. S. *Chem. Mater.* **2001**, *13*, 4382

101. Dominko, R.; Arcon, D.; Mrzel, A.; Zorko, A.; Cevc, P.; Venturini, P.; Gaberscek, M.; Remskar, M.; Mihailovic, D. *Adv. Mat* **2002**, *14*, 1531

102. Arcon, D.; Dominko, R.; Mrzel, A.; Remskar, M.; Zorko, A.; Cevc, P.; Gaberscek, M.; Mihailovic, D. *Struct. and Elect. Prop. of Molecular Nanostructures* **2002**, 218

103. Wang, G. X.; Bewlay, S.; Yao, J.; Liu, H. K.; Dou, S. X. *Electrochem. and Solid Stat Lett.* **2004**, *7*, A321

104. Chen, J.; Tao, Z. L.; Li, S. L. *Angew. Chem Int Ed*, **2003**, *42*, 2147

105. Chan, C. K.; Peng, H.; Liu, G.; McIlwrath, K.; Zhang, X. F.; Huggins, R. A.; Cui, Y. *Nature Nanotechnology* **2008**, *3*, 31.

106. Nam, K. T.; Kim, D. W.; Yoo, P. J.; Chiang, C. Y.; Meethong, N.; Hammond, P. T.; Chiang, Y. M.; Belcher, A. M. *Science* **2006**, *312*, 885.

107. Park, M. S.; Wang, G. X.; Kang, Y. M.; Wexler, D.; Dou, S. X.; Liu, H. K. *Angew. Chem. Int. Ed.* **2007**, *46*, 750.

108. Armstrong, G.; Armstrong, A. R.; Bruce, P. G.; Reale, P.; Scrosati, B. *Adv. Mater.* **2006**, *18*, 2597.

109. Chan, C. K.; Peng, H.; Twesten, R. D.; Jarausch, K.; Zhang, X. F.; Cui, Y. *Nano Letters* **2007**, *7*, 490.

110. Tao, Z. L.; Xu, L. N.; Gou, X. L.; Chen, J.; Yuan, H. T. *ChemComm* **2004**, 2080

111. Jiao, L.; Yuan, H.; Wang, Y.; Cao, J.; Wang, Y. *Electrochem. Comm.* **2005**, *7*, 431

112. Reinoso, J. M.; Muhr, H. J.; Krumeich, F.; Bieri, F.; Nesper, R. *Helv. Chim. Acta* **2000**, *83*, 1724

113. Therese, H. A.; Rocker, F.; Reiber, A.; Li, J.; Stepputat, M.; Glasser, H.; Kolb, U.; Tremel; W. *Angew. Chem. Int. Ed.* **2005**, *44*, 262

114. Liu, M.; Cowley, J. M. *Carbon* **1994**, 32, 393

115. Reznik, D.; Olk, C. H.; Neumann, D. A.; Copley, J. R. D. *Phys. Rev. B.* **1995**, 52, 116

116. Wu, F. Y.; Cheng, H. M. *J. Phys. D: Appl. Phys.* **2005**, 38, 4302

117. Venkateswaran, U. D.; Rao, A. M.; Richter, E.; Menon, M.; Rinzler, A.; Smalley, R. E.; Eklund, P. C. *Phys. Rev. B* **1999**, 59, 10928

118. Tang, J.; Qin, L. C.; Sasaki, T.; Yudasaka, M.; Matsushita, A.; Iijima, S. *Phys. Rev. Lett.* **2000**, 85, 1887

119. "Graphite Whiskers, Cones, and Polyhedral Crystals" by S. Dimovski and Y. Gogotsi in "Nanomaterials Handbook" ed. By Y.Gogotsi, Tailor and Francis (2007).

120. Gogotsi, Y.; Libera, J. A.; Kalashnikov, N.; Yoshimura, M, *Science* **2000**, *290*, 317

121. Okuno, H.; Palnichenko, A.; Despres, J.-F.; et al. *Carbon* **2005**, *43*, 692

122. Kim, Y-S.; Mizuno, M.; Tanaka, I.; Adachi, H. *Jap. J. Appl. Phys.* **1998**, *37*, 4878

123. Golberg, D.; Mitome, M.; Bando, Y.; Tang, C. C.; Zhi, C. Y. *Appl. Phys. A* **2007**, 88, 347

124. Celik-Aktas, A.; Zuo, J. M.; Stubbins, J. F.; Tang, C.; Bando, Y. *Acta. Cryst. A* **2005,** 61, 533

125. Zhu, Y. Q.; Hsu, W. K.; Grobert, N.; Chang, B. H.; Terrones, M.; Terrones, H.; Kroto, H. W.; Walton, D. R. M. *Chem. Mater.* **2000**, 12, 1190

126. Mori, H.; Ogata, S.; Li, J.; Akita, S.; Nakayama, Y. *Physical Review B* **2006**, *74*, 165418.

127. Dubay, O.; Kresse, G. *Physical Review B* **2003**, *67*, 035401.

128. Cheng, H.; Cooper, A.; Pez, G.; Kostov, M.; Piotrowski, P.; Stuart, S. *J. Phys. Chem. B* **2005**, *109*, 3780.

129. Liu, Y.; Nishimura, N.; Otani, Y. *Computational Materials Science* **2005**, *34*, 173.

130. Charlier, J-C.; Gonze, X.; Michenaud, J.-P. *Europhys. Lett.* **1995**, *29*, 43

131. Tersoff, J.; Ruoff, R. S. *Phys. Rev. Lett* **1994,** *73,* 676

132. Peters, M.; McNeil, L. E.; Lu, J. P.; Kahn, D. *Phys. Rev. B.* **2000**, *61*, 5939

133. Chesnokov, S. A.; Nalimova, V. A.; Rinzler, A. G.; Smalley, R. E.; Fischer, J. E. *Phys. Rev. Lett.* **1999,** *82*, 343

134. Lee, Y.-S.; Marzari, N. *Phys. Rev. Lett.* **2006**, *97*, 116801

135. Srolovitz D. J, Safran S. A., Tenne R. *Phys Rev E* **1994**, *49*, 5260

136. Enyashin, A. N.; Makaruin, Y. N.; Ivanovskii, A. L. *Doklady Phys. Chem.* **2004,** *399,* 293

137. Miyamoto, Y.; Rubio, A.; Louie, S. G.; Cohen, M. L. *Phys. Rev. B* **1994**, *50*, 4976

138. Cohen, M. L. *Solid State Commun.* **1994**, *92*, 45

139. Miyamoto, Y.; Rubio, A.; Louie, S. G.; Cohen, M. L. *Phys. Rev. B* **1994**, *50*, 18360

140. Rubio, A.; Corkill,m J. L.; Cohen, M. L. *Phys. Rev. B* **1994**, 5081

141. Jhi, S.-H.; Kwon, Y.-K. *Phys. Rev. B* **2004**, *69*, 245407

142. Wu, X.; Yang, J.; Hou, J. G.; Zhu, Q. *J. Chem. Phys.* **2004**, *121*, 8481

143. Wu, X.; Yang, J.; Hou, J. G.; Zhu, Q. *J. Chem. Phys.* **2006**, *124*, 054706

144. Han, S. S.; Kang, J. K.; Lee, H. M.; Van Duin, A. C. T.; Goddard, W. A. *J. Chem. Phys.* **2005**, *123*, 114704

145. Hafner, J.; Wolverton, C.; Ceder, G. *MRS Bulletin* **2006**, *31*, 659

146. Ceder, G. *Science* **1998**, *280*, 1099

147. de Fontaine, D.; Ceder, G.; Asta, M. *Nature* **1990**, *343,* 544

148. Oganov, A. R.; Glass, C. W.; Ono, S. *Earth Planet. Sci. Lett.* **2006**, *241*, 95

149. Ong, S. P.; Wang, L.; Kang, B.; Ceder, G. *Chem. Mater.* **2008,** *20*, 1798

150. Zhou, F.; Maxisch, T.; Ceder, G. *Phys. Rev. Lett.* **2006**, *97*, 155704

151. Maxisch, T.;Ceder, G. *Phys. Rev. B* **2006**, *73*, 174112

152. LePage, Y.; Saxe, P. *Phys. Rev. B* **2001**, *63,* 174103

153. Kang, K.; Morgan, D.; Ceder, G. *Phys. Rev. B* **2009**, *79*, 014305

154. Zhou, F.; Cococcioni, M.; Marianetti, C. A.; Morgan, D.; Ceder, G. *Phys. Rev. B* **2004**, *70,* 235121

155. Curtarolo, S.; Morgan, D.; Persson, K.; Rodgers, J.; Ceder, G. *Phys. Rev. Lett.* **2003**, *91,* 135503

156. Morgan, D.; Ceder, G.; Curtarolo, S. *Meas. Sci. Technol.* **2005**, *16*, 296

157. Fischer, C. C.; Tibbetts, K.; Morgan, D.; Ceder, G. *Nature Materials* **2006**, *5*, 641

158. Hohenberg, P.; Kohn, W. *Physical Review* **1964**, *136*, 864

159. Jones, R. O.; Gunnarsson, O. *Rev. Mod. Phys.* **1989**, *61*, 689

160. Kohn, W.; Sham, L. J. *Physical Review* **1965**, *140*, 1133

161. Perdew, J.; Yue, W. *Phys. Rev. B* **1986**, *33*, 8800

162. Perdew, J.; Burke, K.; Ernzerhof, M. *Phys. Rev. Lett.* **1996**, *77,* 3865

163. Dreizler, R. M.; Gross, E. K. U. *Density Functional Theory* **1990**, Springer, Berlin

164. Martin, R. M. *Electronic Structure Theory: Basic Theory and Practical Methods* **2004**, Cambridge University Press, Cambridge, UK

165. Mills, G.; Jonsson, H.; Schenter, G. K. *Surf. Sci.* **1995**, *324*, 305

166. Kresse, G.; Furthmuller, J. *Comp. Mat. Sci.* **1996**, *6*, 15

167. Perdew, J. P. *Physical Review B* **1996**, *54*, 16533.

168. Blochl, P. E. *Physical Review B* **1994**, *50*, 17953.

169. Kresse, G.; Joubert, D. *Physical Review B* **1999**, *59*, 1758.

170. Aydinol, M.; Kohan, A.; Ceder, G. *Journal of Power Sources* **1997**, *68*, 664.

171. Popovitz-Biro, R.; Sallacan, N.; Tenne, R. *J. Mater. Chem.* **2003**, *13*, 1631

172. Chen, J.; Li, S. L.; Tao, Z. L.; Gao, F. *Chem. Comm.* **2003**, 980

173. Chan, C. K.; Peng, H.; Twesten, R. D.; Jarausch, K.; Zhang, X. F.; Cui, Y. *Nano Letters* **2007**, *7*, 490.

174. Kang, K.; Meng, Y. S.; Breger, J.; Grey, C. P.; Ceder, G. *Science* **2006**, *311*, 977.

175. Van der Ven, A.; Ceder, G. *Electrochem. Solid-State Lett.* **2000**, *3,* 301.

176. Morgan, D.; Ceder, G.; Saidi, M. Y.; Barker, J.; Swoyer, J.; Huang, H.; Adamson, G. *Chem. Mater.* **2002**, *14*, 4684.

177. Aydinol, M. K.; Kohan, A. F.; Ceder, G.; Cho, K.; Joannopoulos, J. *Phys. Rev. B* **1997**, *56,* 1354.

178. Jonsson, H.; Mills, G.; Jacobsen, K. *Classical and Quantum Dynamics in Condensed Phase Simulations*; World Scientific Publishing Company: Hackensack, NJ, **1998.**

179. Mendizabal, F.; Contreras, R.; Aizman, A. *J. Phys. Condens. Matter* **1997**, *9*, 3011.

180. Hsu, W. K.; Chang, B. H.; Zhu, Y. Q.; Han, W. Q.; Terrones, H.; Terrones, M.; Grobert, N.; Cheetham, A. K.; Kroto, H. W.; Walton. D. R. M. *J. Am. Chem. Soc.* **2000**, *122*, 10155.

181. Seifert, G.; Terrones, H.; Terrones, M.; Jungnickel, G.; Frauenheim, T. *Phys. Rev. Lett.* **2000**, *85*, 146.

182. Becke, A. D.; Edgecombe, K. E. *J. Chem. Phys.* **1990**, *92*, 5397.

183. Silvi, B.; Savin, A. *Nature (London)* **1994**, *371*, 683.

184. Savin, A.; Nesper, R.; Wengert, S.; Fässler, T. F. *Angew. Chem., Int. Ed. Engl.* **1997**, *36*, 1808.

185. Ceder, G.; Van der Ven, A. *Electrochimica Acta* **1999**, *45*, 131.

186. Arroyo y de Dompablo, M. E.; Van der Ven, A.; Ceder, G. *Physical Review B* **2002,** *66*, 064112.

187. Seifert, G.; Kohler, T.; Tenne, R. *J. Phys. Chem. B* **2002**, *106*, 2497.

188. Zhu, Y. Q.; Hsu, W. K.; Terrones, H.; Grobert, N.; Chang, B. H.; Terrones, M.; Wei, B. Q.; Kroto, H. W.; Walton, D. R. M.; Boothroyd, C. B.; Kinloch, I.; Chen, G. Z.; Windle, A. H.; Fray, D. J. *J. Mater. Chem*. **2000**, *10*, 2570.

189. Pantano, A.; Parks, D. M.; Boyce, M. C.; Nardelli, M. B. *J. Appl. Phys*. **2004**, *96*, 6756.